# Phase Transitions in Transition Metal Dichalcogenides studied by Femtosecond Electron Diffraction

by

Kerstin Haupt

*Thesis presented in partial fulfilment of the requirements for the degree of*

***Doctor of Philosophy***

*at the University of Stellenbosch*

Department of Physics,
University of Stellenbosch,
Private Bag X1, 7602 Matieland, South Africa.

Promoters:

Prof. Heinrich Schwoerer
Prof. Erich G. Rohwer

December 2013

# Declaration

By submitting this dissertation electronically, I declare that the entirety of the work contained therein is my own, original work, that I am the sole author thereof (save to the extent explicitly otherwise stated), that reproduction and publication thereof by Stellenbosch University will not infringe any third party rights and that I have not previously in its entirety or in part submitted it for obtaining any qualification.

October 19, 2013

# Abstract

Low-dimensional materials are known to undergo phase transitions to differently ordered states, when cooled to lower temperatures. These phases often show a periodic modulation of the charge density (called a charge density wave – CDW) coupled with a periodic perturbation of the crystal lattice (called a periodic lattice distortion – PLD). Although many experiments have been performed and much has been learnt about CDW phases in low-dimensional materials, the reasons for their existence are still not fully understood yet. Many processes, involving either strong electron–electron or electron–lattice coupling, have been observed which all might play a role in explaining the formation of different phases under different conditions.

With the availability of femtosecond lasers it has become possible to study materials under highly nonequilibrium conditions. By suddenly introducing a known amount of energy into the system, the equilibrium state is disturbed and the subsequent relaxation processes are then observed on timescales of structural and electronic responses. These experiments can deliver valuable information about the complex interactions between the different constituents of condensed matter, which would be inaccessible under equilibrium conditions.

We use time resolved electron diffraction to investigate the behaviour of a CDW system perturbed by a short laser pulse. From the observed changes in the diffraction patterns we can directly deduce changes in the lattice structure of our sample.

A femtosecond electron diffraction setup was developed at the Laser Research Institute in Stellenbosch, South Africa. Short laser pulses produce photo electrons which are accelerated to an energy of 30 keV. Despite space charge broadening effects, electron pulses shorter than 500 fs at sample position can be achieved. Technical details of this system and its characterisation as well as sample preparation techniques and analysis methods are described in detail in this work.

Measurements on two members of the quasi-two-dimensional transition metal dichalcogenides, namely $4H_b$-$TaSe_2$ and $1T$-$TaS_2$, are shown and discussed. Both show fast (subpicosecond) changes due to the suppression of the PLD and a rapid heating of the lattice. When the induced temperature rise heats the sample above a phase transition temperature, a complete transformation into the new phase was observed. For $4H_b$-$TaSe_2$ we found that the recovery to the original state is significantly slower if the PLD was completely suppressed compared to only disturbing it. On $1T$-$TaS_2$ we could not only study the suppression of the original phase but also the formation of the higher energetic CDW phase. Long (100 ps) time constants were found for the transition between the two phases. These suggest the presence of an energy barrier which has to be overcome in order to change the CDW phase. Pinning of the CDW by defects in the crystal structure result in such an energy barrier and consequently lead to a phase of domain growth which is considerably slower than pure electron or lattice dynamics.

# Opsomming

Dit is bekend dat lae-dimensionele materie fase oorgange ondergaan na anders georiënteerde toestande wanneer afgekoel word tot laer temperature. Hierdie fases toon dikwels 'n periodiese modulasie van die elektron digtheid (genoem 'n "charge density wave" – CDW), tesame met 'n periodiese effek op die kristalrooster (genoem 'n "periodic lattice distortion" – PLD). Alhoewel baie eksperimente al uitgevoer is en al baie geleer is oor hierdie CDW fase, is die redes vir hul bestaan nog steeds nie ten volle verstaan nie. Baie prosesse, wat of sterk elektron–elektron of elektron–fonon interaksie toon, is al waargeneem en kan 'n rol speel in die verduideliking van die vorming van die verskillende fases onder verskillende omstandighede.

Met die beskikbaarheid van femtosekonde lasers is dit nou moontlik om materie onder hoogs nie-ewewig voorwaardes te bestudeer. Deur skielik 'n bekende hoeveelheid energie in die stelsel in te voer, word die ewewigstaat versteur en word die daaropvolgende ontspanning prosesse waargeneem op die tydskaal van atomies strukturele en elektroniese bewiging. Hierdie eksperimente kan waardevolle inligting lewer oor die komplekse interaksies tussen die verskillende atomiese komponente van gekondenseerde materie, wat ontoeganklik sou wees onder ewewig voorwaardes.

Ons gebruik elektrondiffraksie met tyd resolusie van onder 'n pikosekonde om die gedrag van 'n CDW stelsel te ondersoek nadat dit versteur is deur 'n kort laser puls. Van die waargenome veranderinge in die diffraksie patrone kan ons direk aflei watse veranderinge die kristalstruktuur van ons monster ondergaan.

'n Femtosekonde elektronendiffraksie opstelling is ontwikkel by die Lasernavorsingsinstituut in Stellenbosch, Suid-Afrika. Kort laser pulse produseer foto-elektrone wat dan na 'n energie van 30 keV versnel word. Ten spyte van Coulomb afstoting effekte, kan elektron pulse korter as 500 fs by die monster posisie bereik word. Tegniese besonderhede van hierdie opstelling, tegnieke van die voorbereiding van monsters asook analise metodes word volledig in hierdie tesis beskryf.

Metings op twee voorbeelde van kwasi-tweedimensionele semi-metale, naamlik $4H_b$-$TaSe_2$ en $1T$-$TaS_2$, word gewys en bespreek. Beide wys 'n vinnige (subpikosekonde) verandering as gevolg van die versteuring van die PLD en 'n vinnige verhitting van die kristalrooster. Wanneer die geïnduseerde temperatuur bo die fase oorgang temperatuur styg, is 'n volledige transformasie na die nuwe fase waargeneem. Vir $4H_b$-$TaSe_2$ het ons gevind dat die herstelling na die oorspronklike toestand aansienlik stadiger is as die PLD heeltemal viernietig is in vergelyking met as die PLD net versteur is. Met $1T$-$TaS_2$ kon ons nie net alleenlik die vernietiging van die oorspronklike fase sien nie, maar ook die vorming van 'n hoër energie CDW fase. Lang (100 ps) tydkonstante is gevind vir die oorgang tussen die twee fases. Hierdie dui op die teenwoordigheid van 'n energie-versperring wat eers oorkom moet word om die CDW fase voledig te verander. Vaspenning van die CDW deur defekte in die kristalstruktuur veroorsaak so'n energie versperring en gevolglik lei dit tot 'n fase van groeiende CDW gebiede wat heelwat stadiger as pure elektron of kritalrooster dinamika is.

# Acknowledgements

All in all, many people have been involved in the FED project and I would like to thank each and every one of them for their valuable contributions towards a successfully operating machine, producing good quality data. The LRI has always been a great place to work, thanks to a friendly atmosphere created by staff and students.

I am most thankful to my supervisor Heinrich Schwoerer. I have worked with him for many years and always appreciated his openness and willingness to help in all situations. His enthusiasm for our research has been a great motivation.

I want to thank the other student members of the FED team for being great workmates. Especially Günther Kassier, who seems to never run out of ideas and Nicolas Erasmus, who is always full of hope and eager to bring the project forward. Both contributed with many ideas and valuable skills to the success of the project. Ilana Boshoff and Andrea von Flotow joined the project later and helped a lot with developing sample preparation techniques and performing experiments. I really enjoyed working with all of you!

A big thanks also to the technical staff and the workshop, who could always realise and often even improve our ideas. Especially Ulli Deutschländer was always willing to help, no matter what the problem was. He was quick, reliable and always in a good mood.

Help with the interpretation of the measurement results came from our german collaborators Maximilian Eichberger and Jure Demsar (University of Konstanz) and Kai Rossnagel (University of Kiel), who also provided the $TaS_2$ crystals. Thanks for helping me understand the complex processes happening inside my sample.

# Contents

**Declaration** ii

**Contents** vi

**1 Introduction** 1

**2 Charge Density Waves** 3
2.1 Introduction . . . 3
2.2 Transition Metal Dichalcogenides . . . 7
2.3 Methods . . . 12

**3 The Setup** 15
3.1 The Probe . . . 16
3.2 The Pump . . . 24
3.3 Vacuum System . . . 27
3.4 Improvements . . . 28

**4 Sample Preparation** 29

**5 Measurement and Analysis** 34
5.1 Measurement Strategies . . . 34
5.2 Stability . . . 36
5.3 Preparing and Running the Measurement . . . 37
5.4 Analysis . . . 38

**6 Results** 42
6.1 $4H_b$-$TaSe_2$ . . . 43
6.2 $1T$-$TaS_2$ . . . 44

**7 Summary** 54

**A Preparing and Running the Measurement** 56
A.1 Preparing for the Measurement . . . 56
A.2 The Measurement Program . . . 58

**Bibliography** 61

# 1. Introduction

Some solid materials change their states – often abruptly – as a function of environmental parameters like pressure or temperature. These transitions are generally easy to detect since they can involve large jumps in basic macroscopic parameters like reflectivity, conductivity or spatial dimensions. The origin of these phase changes however is often difficult to find since one has to look at the system on microscopic scales. Here, many different particles, quasiparticles and their interactions between each other can make the matter rather complicated. Sophisticated experimental methods are therefore needed in order to find an explanation for a certain behaviour of a sample.

One example for such abruptly changing phases are the so called charge density wave (CDW) phases which occur in low-dimensional materials: a periodic modulation of the electron density with an accompanying periodic perturbation of the crystal lattice is often found below a sample specific transition temperature. This new periodicity is coupled with an opening of a gap in the electronic band structure of the material which often leads to large jumps in the electric resistivity. Many such phases have been characterised in detail amongst others using microscopic and diffraction techniques. It is known that the occurrence of these CDW states is a consequence of either strong electron–electron or strong electron–lattice coupling. However, for many systems it is not clear which processes actually lead to the development of the observed CDWs and thus, many questions are still to be answered.

With the availability of short laser pulses it has become possible to study a sample under highly nonequilibrium conditions using the pump–probe method: The sample gets abruptly disturbed by a strong laser pulse and its reaction to this sudden blow is then studied.

The principle is the same than the one used in 1964 by Harold Edgerton at MIT when he recorded the famous snapshot of an apple hit by a bullet. The 'sample' (apple) is abruptly disturbed by a fast 'pump pulse' (bullet) and a sharp snapshot is taken shortly afterwards by firing a short 'probe pulse' (camera flash) and detecting it with a suitable slow detector (camera). 'Slow' meaning here, that the exposure time of the camera does not need to be extremely short; the temporal resolution is given by the duration of the flash (i. e. no light is detected except for the flash light). Thus, it is important that the flash is short compared to the process to be observed in order to record a sharp image. Such an experiment can be repeated with different time delays between pump and probe in order to gather information about the whole process (images with the bullet before, inside and behind an apple can be taken and one gets an idea of how an apple 'explodes' when being shot).

Since lasers which are producing pulses in the order of tens to hundreds of femtoseconds are nowadays commercially available, processes happening on subpicosecond time scales are accessible with this method. Movements of electrons and atoms happen on these time scales and thus, microscopic dynamics following laser excitation

can now be studied.

In this work, a femtosecond electron diffraction system is described which was developed and built at Stellenbosch University: short laser pulses act as 'pump' and disturb a crystalline sample while short electron pulses are used as 'probe' signal. The electron beam forms a diffraction pattern on a phosphor screen which is recorded by a CCD camera. The diffraction pattern contains information about the crystalline structure and thus, changes in the diffraction pattern can be interpreted as structural changes in the sample. In particular, a CDW produces diffraction peaks additional to the ones produced by the crystal lattice and therefore, this method is suitable for studying CDWs under nonequilibrium conditions.

Using femtosecond electron diffraction, experiments on two different samples have been performed: $4H_b$-$TaSe_2$ and $1T$-$TaS_2$. Both materials are members of the quasi-two-dimensional transition metal dichalcogenides which are known to develop CDW phases. Both measurements were performed at room temperature. Consequently, in $4H_b$-$TaSe_2$ we disturb the commensurate CDW and (if sufficiently pumped) heat it into the incommensurate phase. Unfortunately, we do not observe a diffraction pattern of the incommensurate CDW since its intensity is too weak. $1T$-$TaS_2$ is in its nearly commensurate phase at room temperature and is pumped into the incommensurate phase, which produces a visible diffraction pattern in our setup. We therefore can observe the complete transition from the one into the other phase in this sample.

The FED project involves typically three to four postgraduate students working as a team, whereby everybody is encouraged to contribute to all the different aspects necessary for a successful operation of the system. I have been part of the team from the very beginning of the project and therefore took part in designing the many parts of the system, assembling, characterising and always improving the setup as well as preparing, running and analysing experiments. This includes performing simulations, developing experimental methods and writing many programs to control devices and analyse the collected data.

I will first provide some background about charge density waves and transition metal dichalcogenides (chapter 2). I will especially introduce the two materials $4H_b$-$TaSe_2$ and $1T$-$TaS_2$ which we used in our experiments. I will also give a short overview of experimental methods which are nowadays used to study materials under highly nonequilibrium conditions.

Since I was involved in the project from the beginning, I contributed a lot to the design and development of the femtosecond electron system. Chapter 3 therefore describes the entire setup as well as the methods we use in order to characterise it in detail. Sample preparation, which can be quite challenging in the field of femtosecond electron diffraction, is discussed in chapter 4. Everything we need to do in order to run a successful measurement and obtain meaningful data is described in chapter 5. This includes measurement strategies, necessary steps to take before performing the actual experiment and the methods we use to analyse the collected data.

Finally, the results of the measurements performed on $4H_b$-$TaSe_2$ and $1T$-$TaS_2$ are described and discussed (chapter 6). A possible scenario taking place within the sample is described. I will conclude this work with a short summary and some final remarks (chapter 7).

# 2. Charge Density Waves

## 2.1 Introduction

A solid consists of many atoms or molecules interacting with each other, forming a continuous structure by developing various types of bonds. An accurate theoretical description of a solid can be obtained by solving a many body problem, which is very difficult to do due to the extremely high number of degrees of freedom. In the case of a crystal however, the atoms (or molecules) are arranged periodically and simple models can be applied in order to describe most of the materials properties. The nearly free electron model as a first approach divides the crystal into a periodic lattice formed by ionic cores and valence electrons which can move almost freely through the crystal, only seeing a weak periodic potential produced by the lattice. Collective phenomena like lattice or electron density oscillations can be described as quasiparticles (phonons, plasmons).

The solution of the Schrödinger equation for a free electron is a plane wave and the dispersion relation is a parabola (energy $E \propto$ square of wave vector $k^2$). For an electron in a periodic potential with a period $a$ the solution of the Schrödinger equation is the product of a plane wave times a function of periodicity $a$ (Bloch's theorem). It follows that the dispersion has to be periodic in $k$-space, with the period $2\pi/a$ [1]. This means that the parabola of the free electron in $k$-space is repeated along $k$ like shown in figure 2.1a.

At certain points in $k$-space ($\pm n\pi/a$, with $n$ being an integer), a crossing of two parabolas indicates the coexistence of two degenerate electronic states. Taking the crossing at $\pi/a$ in figure 2.1a as an example, the two coexisting states can be described by two plane waves, one with wave vector $\pi/a$ and the other with wave vector $-\pi/a$. A linear combination of the two leads to two possible standing waves with different energies, therefore lifting the degeneracy. The energy difference between them depends on the amplitude of the modulation of the background potential. Therefore, gaps open in the vicinity of band crossings and the dispersion separates into several discrete bands.

The bands are filled up to the Fermi energy with electrons and since in most scenarios only the electrons close to the Fermi level can change their states, the band structure in this region is of great interest. Above all, one can now distinguish between insulators, conductors, semimetals and semiconductors just by looking at the band structure around the Fermi energy. In particular the shape of the Fermi level in $k$-space (Fermi surface) can be a useful picture to describe some of the materials properties.

**CDW Formation** The formation of a band gap is coupled to a periodic potential in the crystal. In general this is produced by the atomic cores and therefore its period is given by the lattice constant. Under certain conditions, some materials can develop

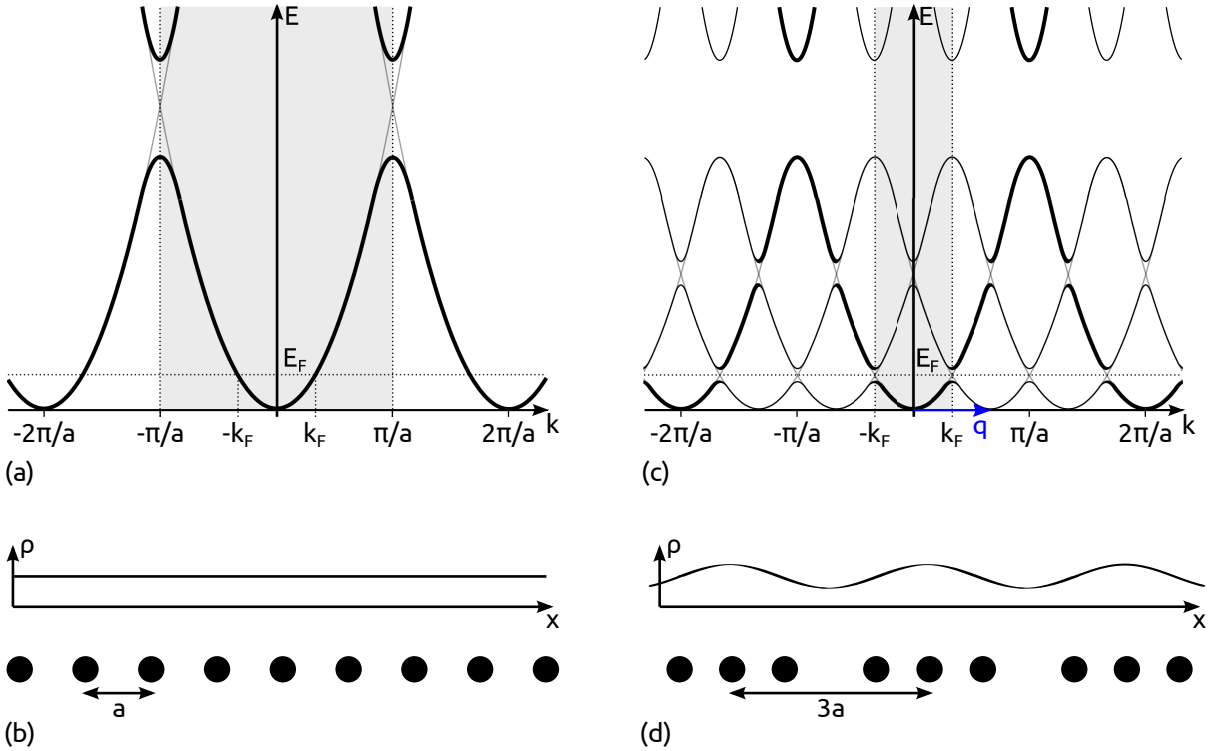


Figure 2.1: One-dimensional example of a crystal with and without a CDW: (a) Band structure of a simple crystal. (b) Electron density $\rho$ and atomic positions in real space. (c) Band diagram after introducing a CDW with wave vector $q$. (d) Modulation in electron density and atomic positions due to the CDW.

an additional, usually much weaker periodic potential called a charge density wave (CDW). This new periodicity which can be viewed as a perturbation of the original lattice potential leads to the formation of additional gaps in the band structure.

We assume a strongly correlated material which is metallic at sufficiently high temperatures and therefore its electron density is constant over the whole lattice (figure 2.1a and b). This means, we have a partially filled band and thus no band gap at the Fermi level. It is always favourable for a system to change into a new state if in this way its total energy can be lowered. Since the system might need to spend energy in order to change its state, the energy gain of the new state must exceed the amount of energy used for the transition in order for the new state to occur. If, for example, a new band gap would open around the Fermi level (and hence the Fermi surface would disappear at this point), this would lower the energy states below the Fermi level and rise the ones above the Fermi level. However, such a state is only profitable below a certain temperature when enough electrons are in the lower states. In this case many electron energies would be lowered and only a few would be increased and therefore the total energy of the system is reduced.

Such a band gap opening is strongly correlated with a periodic perturbation of both the electron density (CDW – charge density wave) and the lattice (PLD – periodic lattice distortion). The development of such a charge density wave phase can be triggered by different mechanisms, involving either strong electron–electron coupling or strong electron–phonon coupling.

The next three paragraphs explain the mechanisms needed to understand the development of CDW phases in the later introduced samples.

**Peierls Transition** By introducing a superstructure with a wave vector $\vec{q}$, the band structure will be 'copied and pasted' along $\vec{q}$. Depending on the shape of the Fermi surface, it might be possible to reduce it's size by choosing one or several suitable wave vectors such that as many Fermi surface sections as possible will fall on top of each other. Due to the band gap openings at these positions many energy states will be lowered and the CDW phase becomes favourable for the system. The process of shifting Fermi surface sections on top of each other is called 'nesting' and $\vec{q}$ is then called the 'nesting vector'.

In the one-dimensional example shown in figure 2.1 the atomic lattice is described by the lattice constant $a$ and the reciprocal lattice constant $2\pi/a$. A new periodicity with a wave vector $q < 2\pi/a$ is introduced to the system. This results in a change of the band structure of the system: The Brillouin zone will be copied and pasted along $q$, the size of the first Brillouin zone reduces to $q$ and band gaps form at the crossings of two bands which occur at the new Brillouin zone edges at $\pm q$ as well as in the Brillouin zone centre. If $q$ is chosen to be $2k_F$ (Fermi wave vector), the new band gap will open exactly at the Fermi surface. In the example (figure 2.1c and d) the band is filled to a third, thus $k_F = \frac{1}{3} \cdot \pi/a$ and $q = \frac{1}{3} \cdot 2\pi/a$ and the one band splits into three. In real space we get a periodic perturbation of the lattice as well as of the electron density. Since the gaps form around the Fermi energy, the transition is accompanied by a large jump in resistivity: the initially metallic material becomes an insulator.

Nesting is easily achieved for a one-dimensional system (like in the example), but more difficult for two or even three-dimensional systems since their Fermi surfaces can have much more complex shapes. Here, an opening or partial opening of the Fermi surface is often only efficiently reached by superimposing several CDWs. Therefore, CDWs are most likely to occur in quasi-one-dimensional materials and are also common in quasi-two-dimensional materials like the transition metal dichalcogenides which will be introduced in section 2.2.

Every single CDW can be described by a simple plane wave and every plane wave can (in theory) have an arbitrary direction, wavelength and amplitude, independent of the underlying lattice structure. Nevertheless, many CDWs observed in real materials show some kind of correlation with the lattice structure. Therefore one distinguishes between two types of CDWs: if the wave vector describing the CDW is a sum of rational multiples of the lattice vectors, the CDW is commensurate with the lattice, otherwise it is incommensurate. Strictly speaking, a material showing an incommensurate CDW is not truly periodic anymore and therefore cannot be presented by a reciprocal lattice. However, a CDW is only a small perturbation of the underlying lattice and thus the main structure stays the same. This can be seen in diffraction experiments where the CDW induced peaks are clearly weaker than the Bragg peaks created by the lattice (see for example figure 3.3).

In summary, a Peierls instability is a consequence of strong electron–phonon coupling [2]: the electrons strongly notice the fluctuations of the lattice and therefore a perturbation of the lattice effects the electronic band structure significantly. A certain phonon is able to create a gap in the band structure which decreases the total energy of the system. Peierls transitions are for example found in the organic salt TTF-DCNQ, in the quasi-one-dimensional CDW material $K_{0.3}MoO_3$ (blue bronze) and also in the quasi-two-dimensional $1T$-$TaS_2$ which is introduced later in this work.

**Other Models** The above described theory of CDW development is very simplified and does not in general fully explain how and why a CDW occurs. Many materials develop CDWs but do not fulfil the requirements for an effective nesting of the Fermi surface. It is however a graphical, easy to understand description and depicts the most important features, namely the opening of a band gap and the deformation of the lattice. In fact, the development of a CDW depends on a delicate balance of several factors [2] and is not fully understood yet. Several models are used to explain CDWs in different samples, which are typically based on two different pictures [2]:

- The energy of the system is lowered by introducing a modulation which extends over the whole crystal. This corresponds to the weak coupling limit described above, where the conduction electrons are seen as freely moving in the crystal and not belonging to a specific lattice site. Since the period of the most beneficial modulation depends on the band structure around the Fermi surface and not on the lattice geometry, the resulting CDW is in general incommensurate. The introduced energy gap as well as the amplitude of the modulation are small.

- In the strong coupling limit, the electrons are localised at lattice sites. The energy balance might be improved locally by shifting electrons between neighbouring lattice sites and shortening the bonds between them. This might lead to the formation of clusters consisting of several atoms or molecules. However, if some bonds in a crystal shorten, others (the ones between the clusters) lengthen and consequently the energy balance worsens at these positions. The overall change is only favourable if the sum leads to a reduction of the total energy. Since the formation of a CDW in this picture is coupled to the lattice geometry, the CDW tends to be commensurate. The resulting energy gap and the modulation amplitude are large.

In both cases a strong electron–lattice interaction is an important requirement for the occurrence of the CDW. However, also a strong electron–electron interaction can, under certain circumstances, explain a modulation of the charge density (exciton insulator model, see for example [2]). The lattice deformation can then be seen as a byproduct which occurs because some electron–lattice interaction is present in all materials. In true materials, it is likely to have a mixture of different effects and therefore the matter can turn out to be very complicated.

**Mott Insulator** If atoms in a crystal are far apart in a certain direction, the overlap of the wave functions of neighbouring atoms is small and therefore the bands are narrow in this direction. A narrow band indicates a large effective mass and this again means that it is hard to remove the electrons from their lattice sites [3]. In other words, the potential barrier between two atoms, which the electrons have to overcome in order to move in this direction, gets smaller the closer the atoms move together. Therefore it is possible to have a material whose band structure looks like that of a metal, i. e. the Fermi level lies within a band, but which behaves like an insulator, since the potential barrier is very large. Such a material is called a Mott insulator.

A transition from a metal to a Mott insulator can be reached by decreasing the overlap of the atomic wave functions, which usually requires an increased distance between the atoms. In practice this might be done for example by varying the strain or pressure.

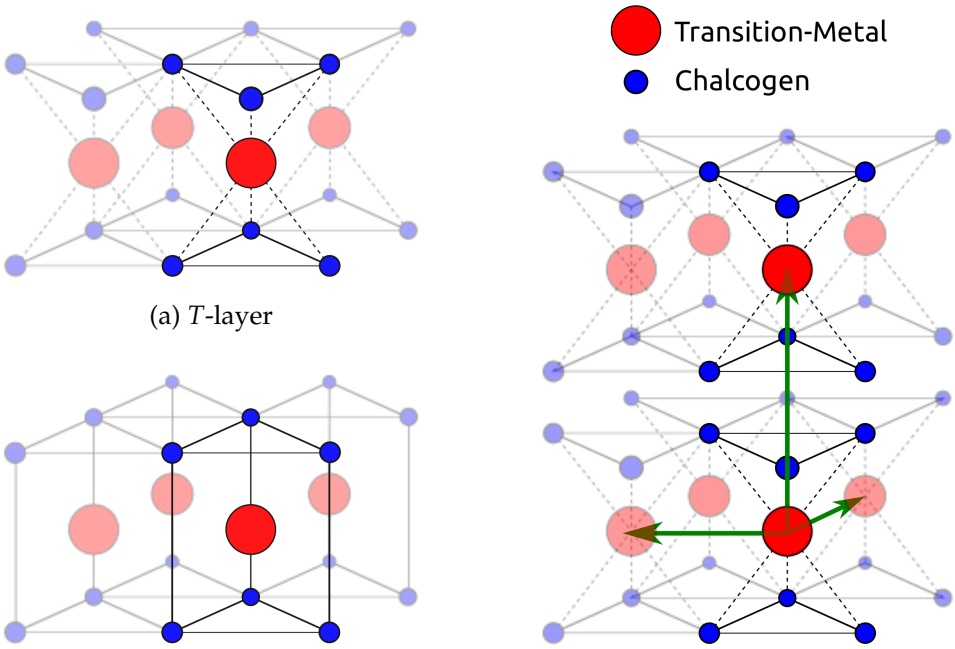


(a) $T$-layer

(b) $H$-layer

(c) $1T$ structure

Figure 2.2: The configuration in octahedrally arranged $T$-layers (a) and trigonal prismatic $H$-layers (b) in transition metal dichalcogenides. The big red dots represent transition metal atoms and the small blue dots represent chalcogen atoms. (c) The $1T$ structure. The green arrows span a unit cell.

A Mott transition does not introduce a CDW in the system. But since a CDW involves a change in the atomic distances, the occurrence of a CDW can trigger a Mott state. This is the case for $1T$-$TaS_2$, which will be introduced within the next section.

## 2.2 Transition Metal Dichalcogenides

Transition metal dichalcogenides have the stoichiometry $TX_2$ where T stands for a transition metal (e. g. Ti, Ta, ...) and X for a chalcogen (e. g. Se, S, ...). A layer of hexagonally packed transition metal atoms is sandwiched between two layers of hexagonally packed chalcogen atoms. Those sandwich slabs are stacked to form a crystal while separated by van der Waals gaps [4]. Consequently, transition metal dichalcogenides generally have a quasi-two-dimensional structure and thus an important condition for the formation of CDW phases is fulfilled in these materials.

The three atom thick sandwiches (from now on called layers) can either have trigonal prismatic ($H$-layer) or octahedral ($T$-layer) configuration (see figure 2.2) and different stackings form different polytypes. A notation $nP_x$ is used to distinguish between the different polytypes, where $n$ is the number of sandwich slabs needed to describe one unit cell, $P$ indicates the bonding structure inside the slabs and $x$ is a letter which is used if the polymorph is not sufficiently described by $nP$ alone [5]. As an example, the $1T$ structure is shown in figure 2.2c.

Many polytypes of the quasi-two-dimensional layered transition metal dichalcogenides show one or more CDW phases. We investigated photo excited phase transitions in two different materials, $4H_b$-$TaSe_2$ and $1T$-$TaS_2$, which are introduced in the following two paragraphs.

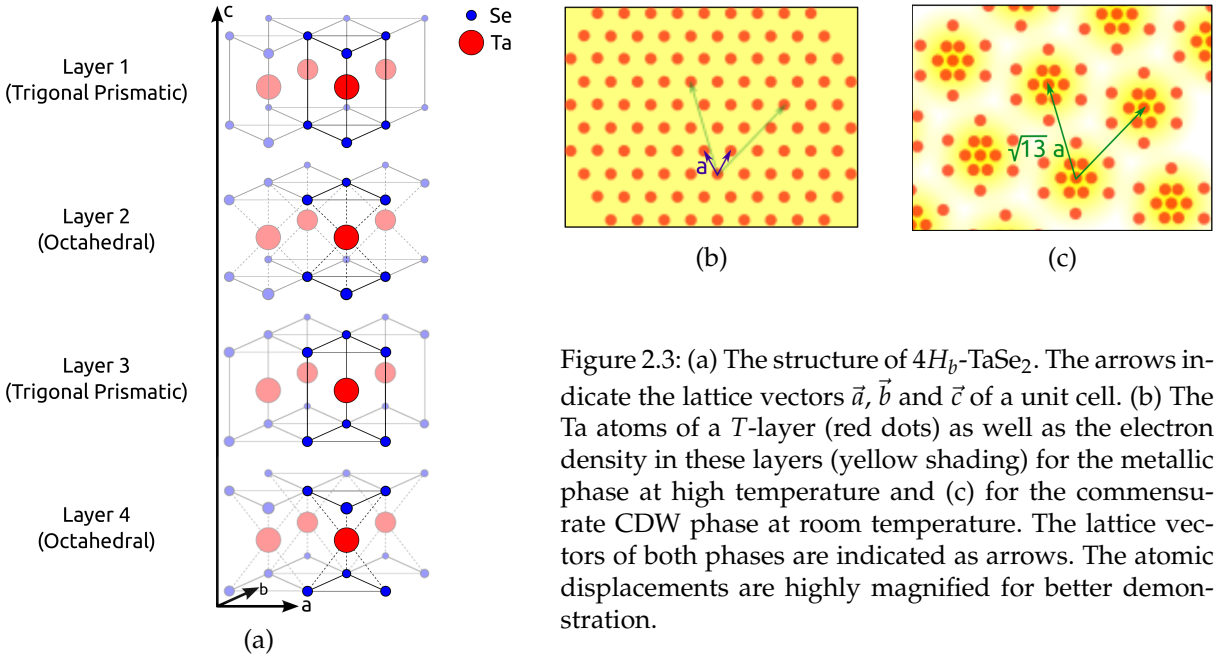


Figure 2.3: (a) The structure of $4H_b$-$TaSe_2$. The arrows indicate the lattice vectors $\vec{a}$, $\vec{b}$ and $\vec{c}$ of a unit cell. (b) The Ta atoms of a $T$-layer (red dots) as well as the electron density in these layers (yellow shading) for the metallic phase at high temperature and (c) for the commensurate CDW phase at room temperature. The lattice vectors of both phases are indicated as arrows. The atomic displacements are highly magnified for better demonstration.

**4$H_b$-$TaSe_2$** The polytype $4H_b$-$TaSe_2$ consists of alternating $H$- and $T$-layers. A unit cell, consisting of four layers, is shown in figure 2.3a. In the metallic phase at high temperatures the hexagonal lattice parameters are $a = b = 3.455$ Å and $c = 25.15$ Å [6] (note that in this case $c$ is including four layers). All other phases are distortions of this basic structure.

Electron and neutron diffraction [7] as well as x-ray diffraction [6, 8] were used to characterise the different CDW phases. Below 600 K an incommensurate CDW forms only in the $T$-layers, which locks into a commensurate phase at 410 K. At around 75 K an incommensurate CDW forms in the $H$-layers while the commensurate CDW in the $T$-layers is still present. Figure 2.4 shows resistivity measurements on $4H_b$-$TaSe_2$ compared to the purely octahedral ($1T$) and purely trigonal prismatic ($2H$) polytypes [7]. The transition between the incommensurate and the commensurate phase is clearly visible in the mixed and the purely octahedral polytypes but does not occur in the $2H$ type.

The in-plane views of the hot metallic phase as well as the commensurate CDW phase are shown schematically in figure 2.3b and c. The Tantalum atoms of one layer are shown as red dots and the yellow shading represents the electron density. In the commensurate state, the six nearest neighbours as well as the six next nearest neighbours of a central Tantalum atom move closer together. Like this, star shaped clusters of 13 atoms each are formed with a centre to centre distance of $\sqrt{13}\,a$. The displacements of the atoms are highly magnified in the picture for better demonstration. The electron density is slightly higher at the centre of the clusters. The lattice vectors of the disturbed structure (green arrows in figure 2.3c) are rotated by 13.9° in respect to the ones of the undisturbed phase (blue arrows in figure 2.3b). There is no modulation in $c$ direction present in the commensurate phase.

The incommensurate phase is not rotated in respect to the lattice and has a wave vector of $q = 0.265a^*$ with $a^*$ being the reciprocal lattice constant. This corresponds to a CDW period in real space of $3.77a$. The amplitude of the CDW decreases with increasing temperature and vanishes at 600 K [7].

The displacement magnitudes of the Ta atoms in the $T$-layers at room temperature is about 0.2 Å [8]. Even though the CDW forms in the $T$-layers, also the atoms in the $H$-layers get slightly modulated with about one tenth of the amplitude of the atoms in the $T$-layers [6]. This is not a CDW on its own, but results from the elastic coupling between the two types of layers. The high temperatures at which the CDW phases exist make this sample a very convenient one since experiments on the commensurate CDW phase can be performed at room temperature. However, so far not many studies have been done on $4H_b$-$TaSe_2$ and therefore there is still a lot to learn about this polytype.

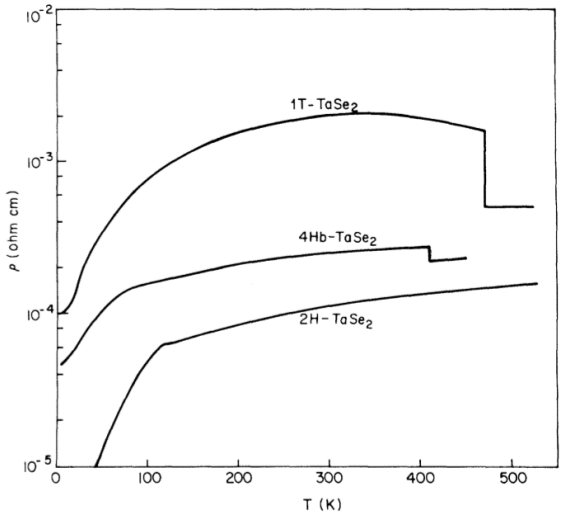


Figure 2.4: Resistivity measurements on three different $TaSe_2$ polytypes, by Di Salvo *et al.* [7].

**1$T$-$TaS_2$** The structure of 1$T$-$TaS_2$ consists of layers of only the $T$-type, separated by van der Waals gaps. The 1$T$ structure is shown in figure 2.2c; lattice vectors spanning a unit cell are indicated by the green arrows. The lattice parameters in the unperturbed high temperature phase are $a = b = 3.36$ Å and $c = 5.90$ Å [9].

Several CDW phases are present in 1$T$-$TaS_2$ at different temperatures which all can be described as a distortion of the basic structure. The phases are as shown in figure 2.5:

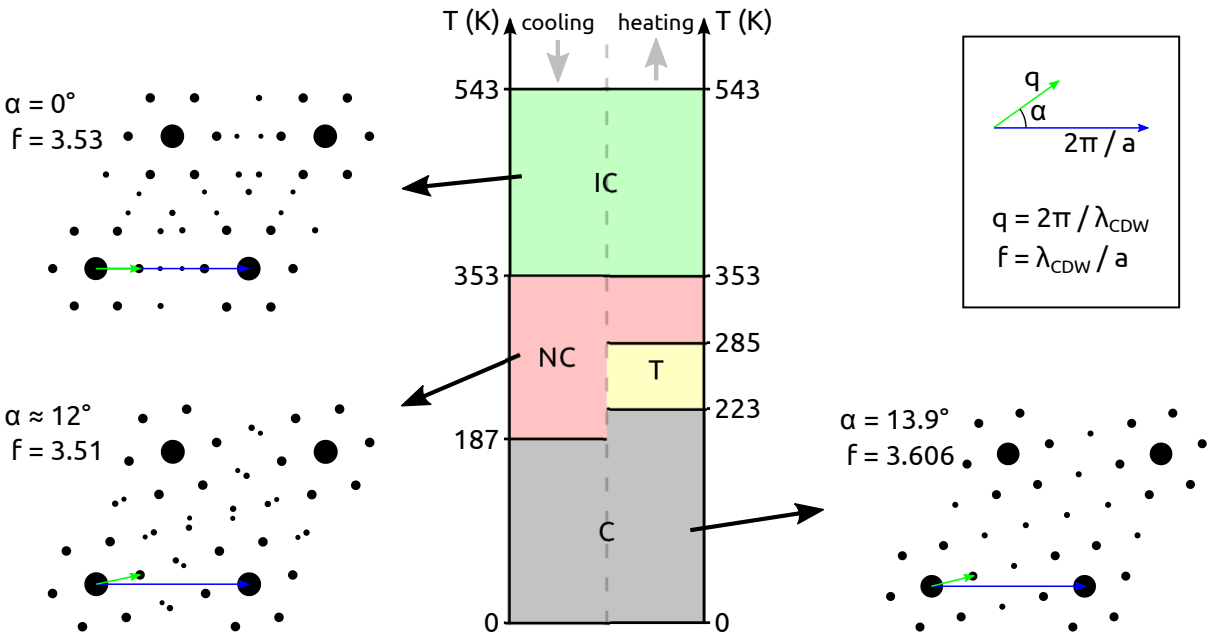


Figure 2.5: The CDW phases of 1$T$-$TaS_2$: The phase diagram shows the temperature ranges in which the different phases occur (C = commensurate, NC = nearly commensurate, IC = incommensurate, T = triclinic). The reciprocal lattices of three of the phases including their wave vectors are illustrated as well (a = lattice constant, $\lambda_{CDW}$ = wave length of the CDW). The higher diffraction orders of the CDW are drawn as smaller dots.

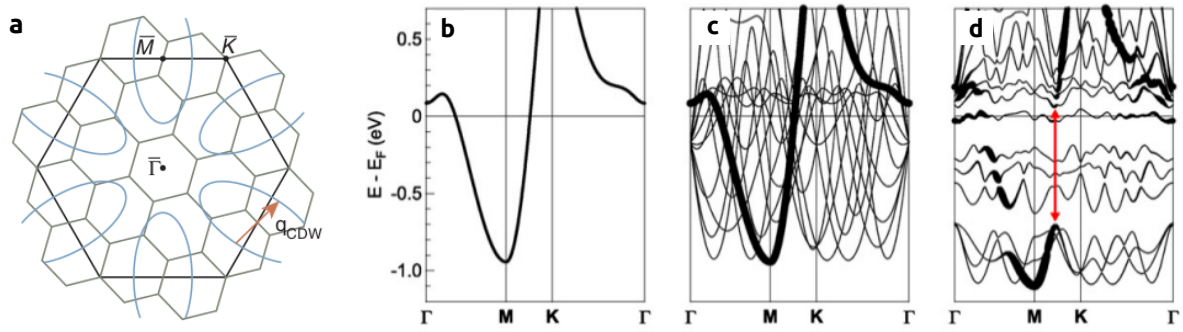


Figure 2.6: (a) The Brillouin zones of $1T$-$TaS_2$ in the metallic state (black) and the commensurate CDW phase (grey). The Fermi surface of the metallic state (blue ellipses) and one of the three nesting vectors (red arrow) are also shown. Image taken from [11]. (b) Calculated band structure of the metallic state of $1T$-$TaS_2$. (c) Additional bands obtained by translating the original band by the three nesting vectors. (d) Taking interactions between the bands into account leads to the reconstructed band structure of the commensurate CDW phase. The spectral weight is still concentrated along the original band. Images taken from [2].

an incommensurate one between 543 K and 353 K, a nearly commensurate one between 353 K and 187 K and a commensurate one below 187 K. There is also a triclinic phase between 223 K and 283 K which exists only when warming the material from the commensurate state (in this case the commensurate phase persists up to a temperature of 223 K) [10].

The in-plane part of the commensurate phase at low temperatures has exactly the same structure as was described above for $4H_b$-$TaSe_2$. Clusters consisting of 13 Tantalum atoms form star patterns like shown in figure 2.3c. This results in a $(\sqrt{13} \times \sqrt{13})$ superstructure which is rotated with respect to the atomic lattice by an angle of 13.9°. The in-plane displacement of the Tantalum atoms is up to 0.24 Å [2] and the electrons shift towards the centre of the clusters.

The commensurate CDW of $1T$-$TaS_2$ has been studied intensely in the past [4, 13, 14] and is well understood: A Peierls transition including three nesting vectors opens a gap just below the Fermi level (see the band structure calculations by Rossnagel [2] shown in figure 2.6). There is still a narrow band intersecting with the Fermi level, as can be seen in the band diagram in figure 2.6d. Since the conduction band is half filled, one would expect the material to be a conductor. However, resistivity measurements clearly show the insulating behaviour at low temperatures (figure 2.7). As already mentioned above, a narrow band indicates a possible Mott transition, which in this case is induced by the formation of the CDW. Between the star clusters formed by the CDW, the atomic distances increase and therefore the overlap of the orbitals is reduced. The material is a Mott insulator.

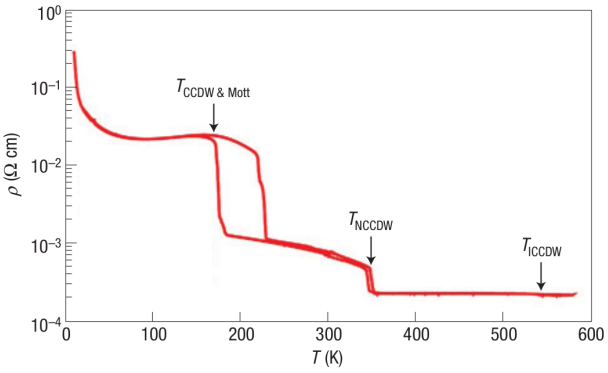


Figure 2.7: Temperature dependent resistivity for $1T$-$TaS_2$, by Sipos *et al.* [12].

At room temperature, $1T$-$TaS_2$ is in a nearly commensurate state which means that the CDW is indeed incommensurate with the lattice, but still very close to the commensurate one observed at lower temperatures (see figure 2.5). The CDW wavelength

is now a little bit smaller ($3.51\,a$ instead of $\sqrt{13}\,a = 3.606\,a$) and the rotation angle in respect to the lattice orientation varies with temperature between 11° (350 K) and 13° (180 K) [9, 10]. The maximum displacement of the Tantalum atoms is again 0.24 Å [15].

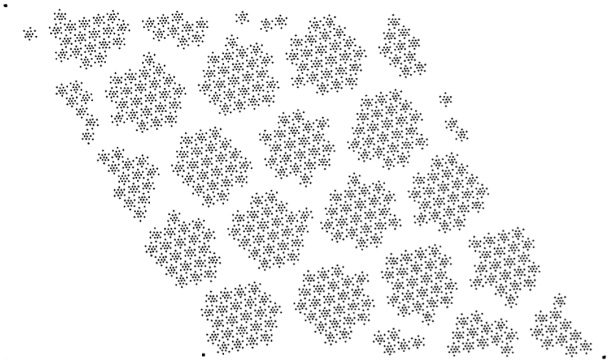

Figure 2.8: The nearly commensurate phase of $1T$-$TaS_2$: Tantalum atoms in a region of $100 \times 100$ unit cells are shown. Only atoms belonging to complete star clusters are plotted as dots, other regions are left blank. The displacements of the atoms is exaggerated five times. Image taken from [9].

The nearly commensurate phase consists of domains showing the commensurate structure, separated by regions of not commensurately modulated domain walls (see figure 2.8). This structure is described in detail in [9]. The domains have an average diameter between 60 Å (350 K) and 90 Å (180 K) [10] and their shape can be approximately described as hexagonal. At room temperature the domain size is 70 Å and each domain contains several tens of star clusters. Since the phase is actually incommensurate, there are small variations in form and size of the domains. The domain wall region, forming the background on which the hexagonal domains occur, consists of a net of connected triangles. In this region the amplitude of the CDW is smaller and no (complete) star clusters are formed. This network of incommensurate domain walls separates the insulating domains and makes the nearly commensurate phase a metallic one (see figure 2.7).

In neighbouring layers, the CDW domain structure is shifted such that the domains in one layer are centred on top of triangular regions of the domain walls in the next layer. This resembles a hexagonal close-packed (hcp) stacking which can be explained by the displacement of the sulfur atoms which is primarily in $c$-direction perpendicular to the layers (up to about 0.1 Å either in or out of the plane) [9]. The atoms get pushed out of the layer where the tantalum atoms move closer together in order to form clusters of 13 atoms each. In between those clusters on the other hand, the sulphur atoms move further into the layer. This also means that the sulfur atoms above the domains mainly move outwards and the ones within the domain walls mainly move inwards, therefore modulating the layer thickness and promoting the hpc domain stacking.

The incommensurate phase is metallic and shows a CDW with a wavelength of $3.53\,a$ which is not rotated in respect to the atomic lattice (see figure 2.5). The maximum displacement of the Tantalum atoms is 0.166 Å parallel to the crystal layers, as was determined by x-ray diffraction [16].

The above information about $4H_b$-$TaSe_2$ and $1T$-$TaS_2$ were obtained using various measurement techniques, amongst others diffraction experiments (x-ray [15], electron and neutron [7]), scanning tunnelling microscopy (STM) [10], electron microscopy [4], photo electron spectroscopy (PES) [14] and resistivity measurements [7, 17]. These techniques are very common for identifying the properties of a sample in thermal equilibrium.

Presently, more advanced methods are used to study materials under nonequilibrium conditions to gather additional information which is inaccessible under thermal equilibrium. In the following section an introduction into these methods is given while later our femtosecond electron diffraction setup is described in detail.

## 2.3 Methods

A material in a CDW phase in equilibrium always shows a periodic perturbation of both the electron density (CDW) as well as the atomic lattice (PLD). This is due to the coupling between electrons and lattice which is present in all materials. Phase and shape of a CDW and its corresponding PLD are the same.

In contrast, if studying the nonequilibrium case we have to distinguish them. The electronic part (CDW) can react within a few femtoseconds to a sudden change in experimental parameters, while the structural part (PLD) changes on a timescale of hundreds of femtoseconds or more [11]. Other conditions, like the presence of domain structures or defects, can lead to even longer time scales.

Therefore, it is advantageous to investigate CDW materials under nonequilibrium conditions when attempting to answer questions about how or why specific CDW phases form. Such experiments are generally based on the pump–probe method: A short laser pulse (pump) is used to abruptly deposit energy into the sample material and another short pulse (probe) measures the momentary state of the sample at certain times after excitation. Since laser pulses with a duration of tens to hundreds of femtoseconds are nowadays very common, timescales in the order of electronic and structural responses can be reached.

So far, three different methods proved to deliver valuable results: Time resolved reflectivity measurements are used to observe changes of the dielectric function, time and angle resolved photo electron spectroscopy (trARPES) is used to measure changes in the band structure and time resolved diffraction experiments are used to study changes in the lattice structure. These three methods are introduced in the following paragraphs.

**Reflectivity Measurements** Time resolved reflectivity measurements can be performed with relatively little effort. Short laser pulses are used as pump and probe pulses. The reflectivity of the probe beam from the sample is measured as a function of delay time between the two pulses. Reflectivity changes can be translated into changes of the dielectric function of the sample. This method therefore is mainly sensitive to electronic properties of the sample. Note that this method only delivers information about the surface layers of the sample and bulk properties might differ.

Photo induced reflectivity changes were measured on several transition metal dichalcogenides in their CDW phases [18–21]. Shapes and time constants of the observed decays give hints on the nature of processes happening inside the sample. Oscillations of the CDW phonon were measured in the vicinity of phase transitions:

Suppose we are in the unperturbed phase but force the atoms onto the positions of the CDW phase. Now we suddenly release the atoms. The atoms will perform a (damped) oscillation around their respective lattice positions. This collective oscillation equals a certain phonon mode of the crystal. A similar scenario takes place if a crystal in a CDW state experiences a sudden photo excitation.

This oscillation can be seen as a modulation of the reflectivity. Its frequency and damping factor can be studied as a function of equilibrium temperature and pump fluence. A weakening of the CDW phonon as well as a decrease in its frequency is often observed when approaching the transition temperature (see [20] for measurements on $1T$-$TaS_2$ and $2H$-$TaSe_2$).

**Photo Electron Spectroscopy** In photo electron spectroscopy (PES) experiments, electrons are extracted from the sample via the photoelectric effect using light with a known wavelength $\lambda$. The energy distribution of the extracted electrons is then measured which contains information about the band structure of the sample material.

The kinetic energy of the freed electron is the difference between the energy of the excitation photon and the energy actually needed to get the electron out of the material (binding energy plus work function). Therefore, by measuring the kinetic energy of the photo electrons one can calculate the energy levels they occupied in the sample material. Consequently, PES is a method to determine the energy diagram of the material.

More information can be obtained when in addition to the kinetic energy of the extracted electrons also its extraction angle is measured. This is called angle resolved photo electron spectroscopy (ARPES). Each electron has a certain momentum inside the material which is linked to its energy. The momentum component parallel to the sample surface is conserved during the extraction process and therefore, the kinetic energy of the extracted electrons is angle dependent. Thus, by measuring the energy angle distribution of the electrons one is directly mapping the band structure of the material [3]. The opening of a band gap due to the development of a CDW can be seen in (time averaged) ARPES measurements [2, 22]. As an example, the band diagram of the commensurate phase of $1T$-$TaS_2$, measured by Hellmann *et al.* [11] is shown in figure 2.9.

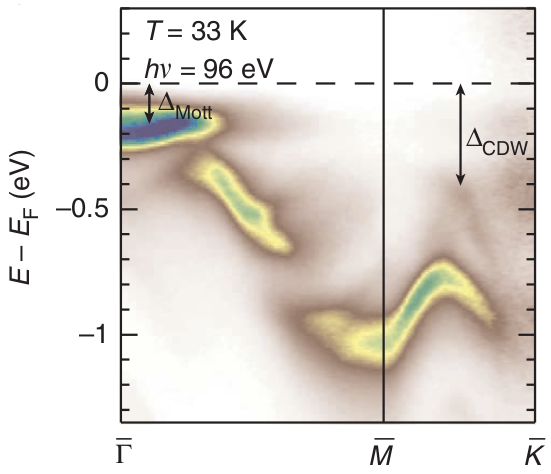


Figure 2.9: ARPES measurements on the commensurate CDW phase of $1T$-$TaS_2$ show two band gaps, by Hellmann *et al.* [11]. $\bar{\Gamma}$, $\bar{M}$ and $\bar{K}$ denote symmetry points in the first Brillouin zone.

PES and ARPES are also suitable for time resolved pump–probe experiments by using short optical pulses. Changes in the band structure in the nonequilibrium case can be directly measured. The high photon energies needed in order to extract electrons from deeper lying energy bands can be obtained by producing high harmonics of short laser pulses. Like this, XUV pulses with a duration of less than 10 fs can be achieved which makes is possible to distinguish purely electronic processes, which happen on a sub-100 fs time scale, from the slower structural processes [11]. Space charge effects have to be taken into account since they modify the electron pulses on their way to the detector. Especially the influence of the short pump pulse on the extracted electrons has to be considered [23].

Time resolved PES experiments have been performed on several CDW materials, amongst others also on $TaS_2$ and $TaSe_2$ polytypes [23–26]:

The $4f$ levels of $1T$-$TaS_2$ in the commensurate CDW phase show a splitting due to the deformation of the lattice. The change of the splitting following photo excitation was studied with time resolved x-ray photo emission spectroscopy [23, 24]. The development of the CDW and PLD could be linked to the observed dynamics: The splitting reduces on a subpicosecond time scale as the CDW melts. After a few picoseconds, the PLD melts as well and a quasi equilibrium is reached. The recovery to the initial state

happens within a few nanoseconds.

The behaviour of band gaps following a sudden excitation was observed on different samples using time resolved ARPES [11]. Comparing the temporal development of the gap regions allows to distinguish between several mechanisms involving either electron–electron or electron–lattice interactions.

**Diffraction Experiments** To observe fast structural changes in crystalline materials, either x-ray or electron diffraction with ultrashort pulses is used. The electrons or photons get diffracted by the crystal lattice and create an image of the reciprocal space on a two-dimensional detector.

The diffraction is effective when the (de Broglie) wavelength of the probe beam is comparable with or smaller than the lattice period. In a typical crystal, like the ones introduced above, the lattice constant is in the order of one Ångström which means that either hard x-rays or electrons with a kinetic energy of more than 0.1 keV are necessary to obtain a diffraction pattern. Both techniques can be used for time resolved measurements.

Short electron pulses are relatively easy to produce and do not require a big laboratory. A major problem in femtosecond electron diffraction (FED) experiments is the pulse broadening due to space charge effects. Setups are therefore kept very compact in order to minimise the travel length of the pulses and maintain a good temporal resolution. An alternative is the use of a pulse compressing device. Electron pulses are easy to manipulate with simple electric or magnetic fields. The cross section for electron diffraction is in general relatively large, so that a low electron current is sufficient in order to produce a reasonable diffraction image on a detector. However, the penetration depth into a typical sample is very small and thus very thin samples ($\approx$ 100 nm) are required when performing electron diffraction in transmission geometry. This is the second major challenge in FED. Experiments have been done on various samples [27, 28] amongst others also on $TaS_2$ [18].

Short x-ray pulses are available at several large FEL (free electron laser) facilities, but can also be generated with a laser driven plasma source [29]. X-ray pulses allow for a high temporal resolution since no pulse broadening effects do occur. However, it is not trivial to manipulate x-ray pulses since the required optics are single crystalline materials which cannot be produced in arbitrary sizes and shapes. Even sophisticated designs allow to collect and focus only a small amount of the available photons. In contrast to the electrons, the cross section for x-ray diffraction is much lower and the penetration depth larger. This means that an intense beam is needed in order to form a useful diffraction image but the sample can be very thick (mm). When pumping with optical light however, only the sample surface is pumped while the x-rays probe the unpumped bulk regions as well. Time resolved x-ray diffraction studies are usually done on one particular Bragg peak only [19, 30].

Our time resolved electron diffraction experiments have been performed on the two introduced materials $4H_b$-$TaSe_2$ and $1T$-$TaS_2$. The setup used for these measurements was developed, built and steadily improved during the last five years at the Laser Research Institute of the Stellenbosch University [31–35]. Since a lot of effort was spent to design a reliably operating setup which is able to produce high quality data, the setup and some experimental techniques will be described in the next three chapters. The actual experiments and their results will be discussed in chapter 6.

# 3. The Setup

The concept of the experiment is based on the pump–probe technique. That means, the target will be hit by two different short pulses (pump and probe), which will have a certain adjustable time delay between each other. The pump pulse triggers the process to be observed in the sample, the probe pulse takes a snapshot of it for a certain time delay after triggering. The temporal resolution is given mainly by the pulse durations and therefore can be very high (tens of femtoseconds). The temporal delay can easily be controlled very accurately by varying the path length of one of the beams: a path length change of 3 µm, which can easily be achieved, corresponds to a temporal delay of 10 fs. Since the signal of the probe beam can be very weak, it is common practice to repeat the experiment with a fixed time delay and integrate the signal until it is satisfactory strong. In this case one data point represents an average over many single shot experiments. By repeating this procedure for different time delays, one can gather information about the whole process.

We use an amplified Ti:Sapphire laser (Clark-MXR CPA 2101) which operates at 1 kHz repetition rate and produces 150 fs short pulses with a centre wavelength of 775 nm. The beam is divided with a 90:10 beam splitter. The strong part is used as an optical pump while the weaker part is used to produce short electron pulses serving as a probe signal. A sketch of our femtosecond electron diffraction setup is shown in figure 3.1. Details of the entire system are given in the following sections.

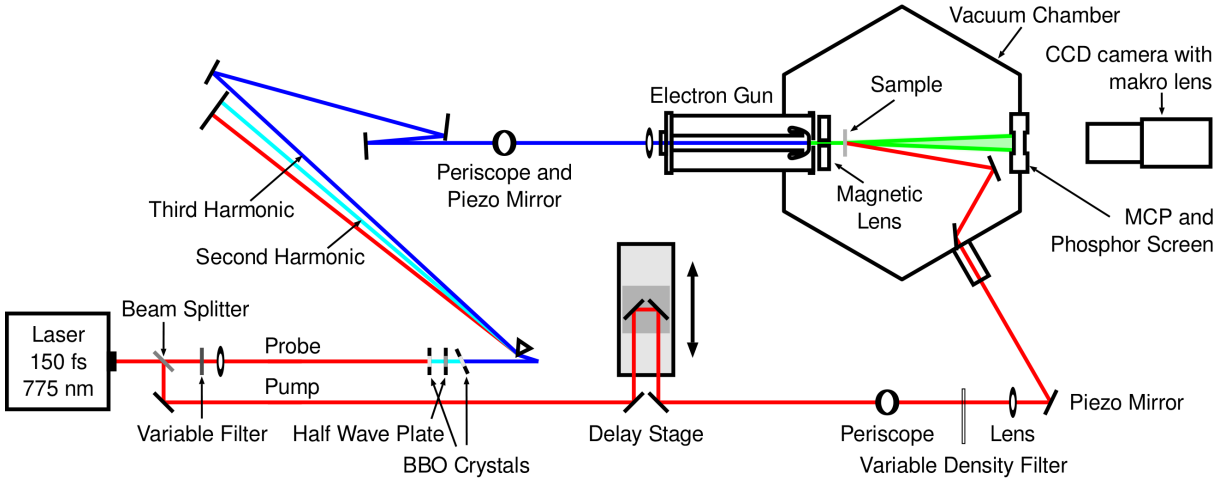


Figure 3.1: Sketch of the FED setup. A laser beam is split into two parts. The probe part is frequency tripled and focused into an electron gun where it produces short electron pulses. These are accelerated, focused by a magnetic lens and diffracted by the crystal structure of the sample. A combination of MCP, phosphor screen and CCD camera is used to detect the diffraction pattern. A delay stage in the pump beam path lets us control the time interval between pump and probe pulses reaching the sample. A detailed explanation of the setup is given in the text.

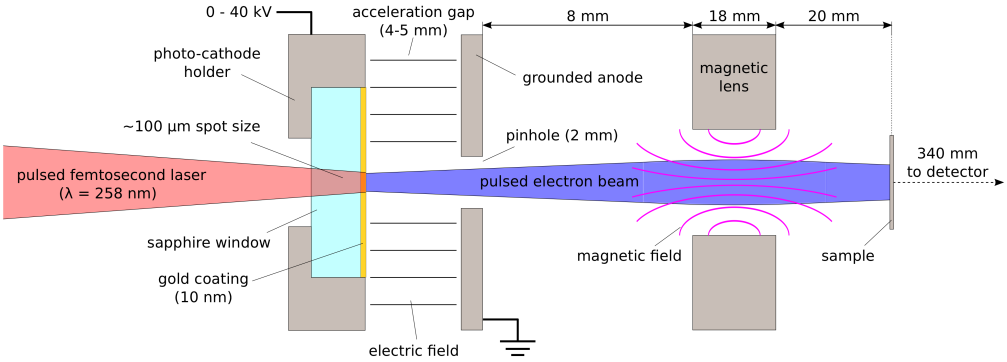


Figure 3.2: A short laser pulse (red) produces photo electrons (blue) which are accelerated by a high electric field and focused by a variable magnetic field.

## 3.1 The Probe

The probe beam has the task to obtain information about the status of the sample during that short moment in which one of the pulses passes through it. The beam therefore consists of weak pulses, which are being manipulated by the sample in some way. Possible changes in the sample initiated by the probe pulse on the other hand can be neglected. With a suitable detector one can observe these probe pulses, now containing information of the sample.

In our case, the probe beam consists of ultra short electron pulses: a weaker part of the laser beam is sent into a specially designed electron gun, where it produces short pulses of free electrons via the photoelectric effect. In transmission geometry, the electrons get diffracted by the lattice of the sample and form a characteristic diffraction pattern on the detector. Changes in the diffraction pattern are equivalent to changes in the crystal structure of the sample.

**Electron Gun** The electron gun is evacuated and attached to a large vacuum chamber where the experiment takes place. The main component of the electron gun is a 10 nm thin layer of gold which has been evaporated onto the front side of a 3 mm thick sapphire (or quartz) window. To extract electrons from the gold film, we frequency triple our laser beam to 258 nm so that its photon energy (4.8 eV) exceeds the work function of the gold layer (4.5 eV) [36]. The laser beam is focused through the window onto the gold layer (see Figure 3.2), photo electrons will leave the layer on the front.

The gold layer forms part of a cathode which is charged to a potential of up to −40 kV and has a distance of 4 to 5 mm from the grounded anode. Anode and cathode form a capacitor with an electric field which accelerates the electrons to an energy of up to 40 keV. The cathode is manufactured in a Rogowski profile to guarantee a smooth decrease of the electric field to the outside of the cathode. This prevents arcing which would not only discharge the capacitor, but could also damage the thin gold layer and reduce its ability to produce free electrons. A variable neutral density filter in the laser beam path enables us to adjust the electron current.

Due to space charge effects, which will be discussed later in this chapter, we want to keep the number of electrons per pulse small ($\approx 1000$). In order to generate pulses containing 1000 electrons each, a UV pulse energy of 100 pJ ($130 \cdot 10^6$ photons) or more is needed, depending on the condition of the gold layer.

The electron current of our probe beam can be measured by simply collecting all

the electrons with a Faraday cup which is connected to an ampere meter. The Faraday cup is constructed such that it collects all the electrons from the beam hitting it as well as possibly emitted secondary electrons. However, it gets difficult when the current is in the order of only a few thousand electrons per pulse, which corresponds to $10^6$ electrons per second or 0.5 pA. A special picoammeter (Keithley 6487, 10 fA resolution) is used for a reliable measurement of such low currents. Our measurements typically have an accuracy of about $\pm 150$ electrons per pulse.

**Magnetic Lens** The electrons will exit the gun through a hole (2 mm diameter) in the anode cap and enter the main vacuum chamber where they first pass through a magnetic lens. The lens has a thickness of 18 mm and a centre hole of 6 mm diameter. The magnetic field is produced by an electric current running through 586 turns of copper wire which are partially surrounded by a yoke made from mild steel. Electrons moving through the magnetic lens will be forced onto a spiral path around the symmetry axis and will experience a deflection towards the axis, independent of their initial direction [37]. The deflection is stronger, the further away a particle is from the axis. The field is optimal for good focusing of the electrons only parallel and close to the symmetry axis and thus, the alignment of the lens with respect to the electron gun is crucial. As a help, a metal tube with an outer diameter of 6 mm can be screwed onto the anode cup. The lens, if adjusted correctly, slides onto it and thus is optimally positioned with respect to the electron gun.

By varying the operating current of the magnetic lens, we can change the focusing of the electron beam. For a 30 keV electron beam with 500 electrons per pulse, the current necessary to focus the beam on the detector is approximately 1 A and the maximum magnetic field on the lens axis is in the order of 100 mT. For higher currents the focal length can be very short so that the beam can be focused before it passes the sample, even if the distance between magnetic lens and sample is as short as only one or two centimetres. As a result the beam produces a highly magnified shadow image of the sample area on the detector which can be very useful for alignment purposes.

Due to the resistance of the long copper wire, the lens produces a significant amount of heat. Since the lens is situated inside the vacuum chamber, the only two ways of cooling are due to thermal radiation and, primarily, due to heat conduction through the mount. Therefore, the lens mount is designed to allow for a good heat conduction and the thick chamber base plate on which the lens is placed serves as a heat sink. When in use with a constant current of 1 A, the outside temperature of the lens stabilises at 50°C. During alignment when higher currents are used temporarily, temperatures above 60°C can be reached. Temperature changes inside the vacuum chamber of only a few Kelvin can affect the position of the sample slightly, and consequently we most likely lose the diffraction signal. For that reason we leave the lens current switched on at all times to ensure thermal equilibrium in the chamber during measurements.

**Detection System** The electrons move through the sample region and continue to drift until they hit the detector which is situated 36 cm behind the magnetic lens. The electron signal is detected with a phosphor screen after being amplified by a chevron pair of micro channel plates (MCP). The MCP has an open-area-ratio of 60%. MCP and phosphor screen have a diameter of 4 cm and are mounted on a vacuum flange, so that the signal can be observed through a window from outside the vacuum chamber.

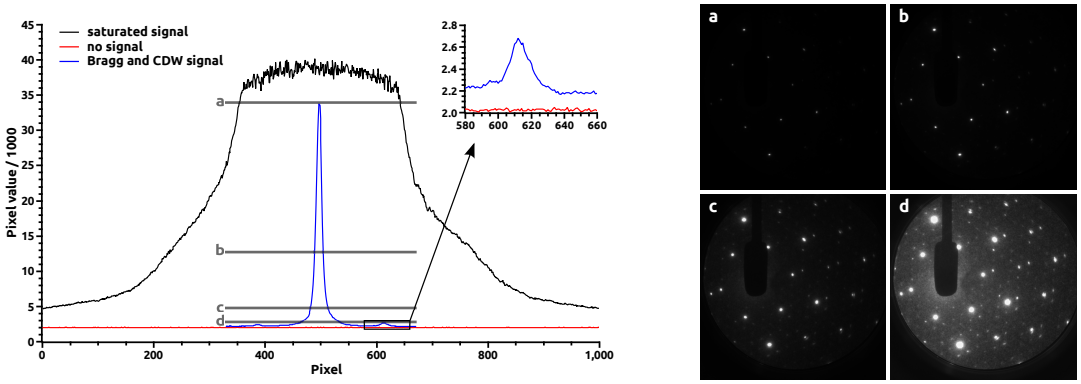


Figure 3.3: The graph shows pixel values of different images taken with the 16bit camera: a saturated signal (black), a dark image (red) and a cut through the image displayed in (a) to (d) showing a typical diffraction pattern of $TaS_2$ with a CDW signal (blue). (a) to (d) show the same picture with different intensity scales which maximum values are indicated by the grey lines in the graph.

A cooled 16 bit camera (EHD SC4022M) takes photos of the diffraction pattern and saves them on a computer. The dynamical range of the camera is shown in figure 3.3. A constant offset of about 2000 counts was measured independent of the integration time (see red curve). The pixels get saturated at a value of around 40000 (black curve) which corresponds to 40000 electron–hole pairs produced by the photons hitting that pixel [38]. This high dynamic range allows us to observe small diffraction peaks (inset in figure 3.3), while at the same time the more intense peaks are not saturated (strong peak in the blue curve). On the right hand side of figure 3.3, four different 8 bit versions of the same 16 bit image are shown. Thereby, only the range between zero and a maximum value indicated by the corresponding grey line in the graph (labelled with the letters a to d) is used to create the 8 bit grey scale. In the first frame, the strong Bragg peaks are not saturated but the weaker spots are not at all visible. The last frame, in contrast, shows clearly the weak spots while the strong ones are now saturated.

The strong signal of the undiffracted electrons should be blocked by a beam block which can be moved sideways from outside the chamber through a rotation feedthrough. The signal would otherwise damage the phosphor screen permanently. The beam block is grounded to prevent it from charging up.

**Sample Mount** The sample is mounted approximately 5 cm behind the cathode. The sample must be free standing and is usually supported by a fine mesh. Sample preparation is one of the major challenges in the field of UED, mainly due to the required thickness of less than 100 nm. More information about UED samples and their preparation is given in chapter 4.

The sample holder is mounted on a $x$-$y$-$z$-translation stage inside the vacuum chamber and has space for either four or nine meshes or apertures of the typical size (3.05 mm diameter) used in transmission electron microscopy (TEM). Several samples and measuring devices (usually a streak camera and a Faraday cup, see figure 3.4) can be mounted on the stage at the same time. The stage is computer controllable from outside the chamber and several positions can be saved in the program. This makes it very easy to switch between different samples and devices.

The sample mount is kept on a potential of 20 V during the measurement. This ensures that possible low energetic photo electrons, produced by the pump beam hitting

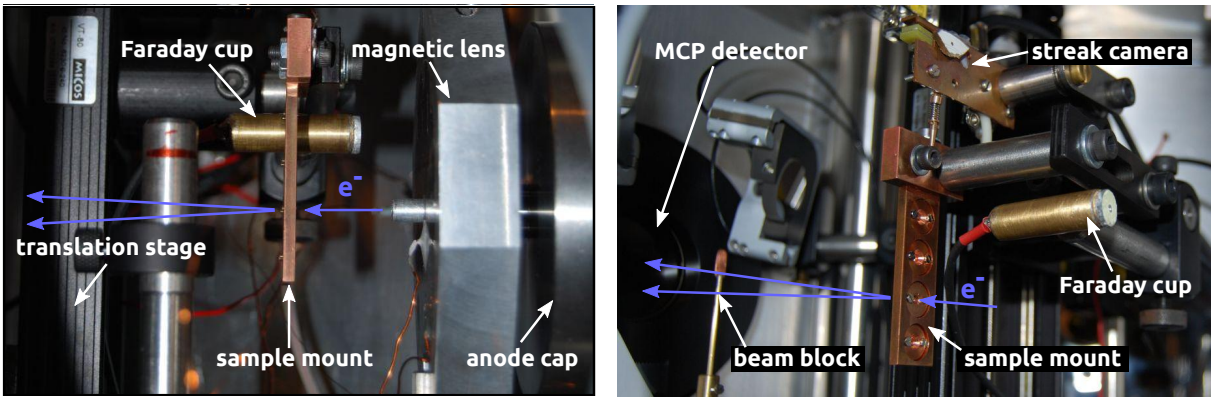


Figure 3.4: Photos of the sample region in the chamber taken from two different angles.

the sample, are collected and do not reach the detector where they would be responsible for a significant background signal.

**Probe Beam Size** During a diffraction experiment, the probe beam is optimised by the magnetic lens to be as small as possible on the detector to get a sharp diffraction image. However, it is also important to look at the beam size at sample position, since it must be ensured, that the probed sample region is pumped homogeneously (i. e. the pump beam must be significantly larger than the probe beam). The electron beam size can easily be measured with an aperture mounted in the same $z$-plane than the sample.

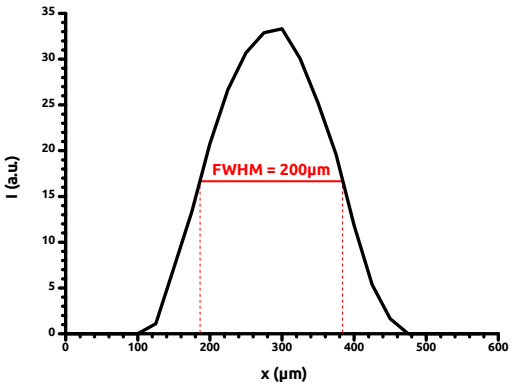


Figure 3.5: Typical electron beam profile measured at sample position with a 50 µm aperture.

The aperture has a diameter of 50 µm which is small compared to the electron beam diameter. If we position the aperture into the electron beam path, we only see a small part of the electrons reaching the detector. To measure the electron beam size we move the aperture step by step sideways over the whole beam diameter and measure the integrated signal strength on the detector for each step. We can then plot the measured intensity over the position of the stage and get the FWHM as a value for the electron beam size at sample position. We can repeat the measurement in vertical direction to get an idea of the ellipticity of the spot.

In figure 3.5 a typical measurement of the probe beam at sample position is shown. Strictly speaking, the curve should still be deconvoluted with a boxcar function of 50 µm width to take account of the finite size of the aperture. However, this has only a negligible effect on the FWHM and thus we can simply read the beam size to be 200 µm.

**Measuring the UV Focus on the Cathode** The size of the probe beam focus on the detector depends on the size of the UV beam on the cathode. The smaller the spot size on the cathode, the sharper the diffraction pattern. Therefore we want the UV focus to be as small as possible. Since there is no space inside the electron gun for an adjustable

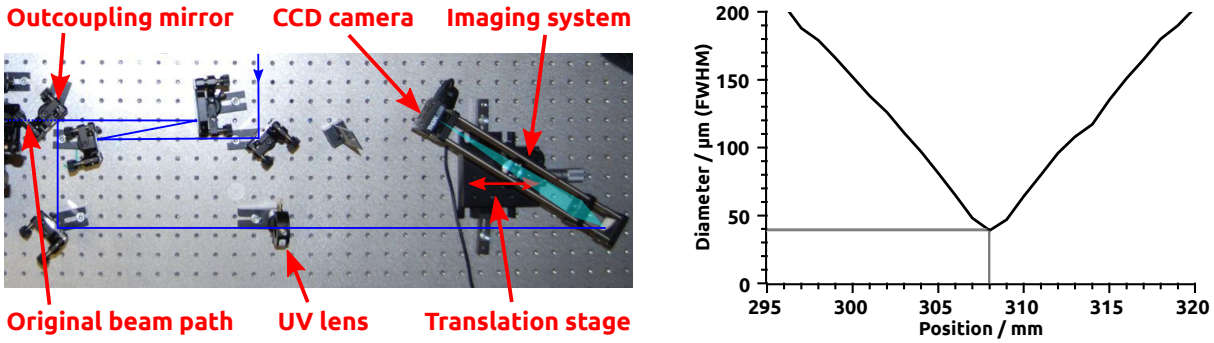


(a) (b)

Figure 3.6: (a) The setup used to measure the UV focus. (b) Diameter of the UV focus as a function of distance from the lens.

lens, the smallest focal length our setup allows is obtained when putting the lens just before the entrance window of the gun. With a little space for alignment purposes, this results in a focal length of 30 cm. Since the UV beam is slightly divergent, the focus is a little more than 30 cm behind the lens.

We cannot observe the focus inside the electron gun and thus, to measure the actual focal distance from the lens and the minimum spot size, we need to do so outside the chamber. Here we use the method of copying the beam. With two mirrors we direct the beam into a convenient direction on the optical table. The lens is mounted in the same distance where it would be placed in the original beam path, an accuracy of $\pm 1$ cm is sufficient. Now the focus is easily accessible for us. Unfortunately we cannot observe the beam directly with a CCD camera placed in the beam path since the protecting glass window in front of the chip blocks the UV light completely. Instead, we constructed a setup which is shown in figure 3.6a: a phosphor screen is placed in the beam path and a camera observes the beam spot on that screen. To get a better resolution, a lens magnifies the region onto the camera. The geometries of the imaging setup are known so that the true beam diameter can be obtained from the pictures taken with the camera. This setup is mounted on a translation stage which can be moved parallel to the UV beam direction. By scanning over the focal range and measuring the beam size at each position we obtain the curve shown in figure 3.6b. The focus has a diameter of 40 µm and is located 30.8 cm behind the lens.

The lens can now be mounted in the original beam path 31 cm before the cathode. The dimensions of the gun are known and so the optimal position of the lens can be determined with an accuracy of 5 mm. For a more accurate alignment the lens is mounted on a translation stage and the electron spot is observed on the detector for different positions of the lens. Thereby it is important to carefully focus the electron beam for every step. A clear minimum of the electron spot size indicates the best position for the UV lens. This part of the alignment might have to be repeated from time to time, for example after replacing the cathode.

**Measuring the Transverse Coherence Length** The transverse coherence length of the electron beam determines the spatial resolution of the diffraction pattern. It must be significantly larger than the period of the periodic structure to be observed in order to get a diffraction pattern from it. In the case of $4H_b$-$TaSe_2$ and $1T$-$TaS_2$, the coherence length must be larger than 3.5 Å to observe the atomic lattice and larger than 13 Å to ob-

serve the CDW superstructure. Thus, the transverse coherence length is an important characterising parameter for our setup.

The transverse coherence length is given by

$$L_\perp = \frac{\lambda}{2\pi\sigma_\vartheta} \tag{3.1}$$

where $\lambda$ is the de Broglie wavelength of the electrons and $\sigma_\vartheta$ the RMS (root mean square) angular spread of the electron beam.

The de Broglie wavelength $\lambda$ is defined as

$$\lambda = \frac{h}{p} \tag{3.2}$$

where $h$ is Planck's constant and $p$ the momentum of the electron. For the relativistic case one gets:

$$\lambda = \frac{hc}{E_\mathrm{k}\sqrt{1 + 2\frac{mc^2}{E_\mathrm{k}}}} \tag{3.3}$$

or

$$\lambda[\mathrm{nm}] = \frac{1.24}{E_\mathrm{k}[\mathrm{keV}]\sqrt{1 + 2\frac{511}{E_\mathrm{k}[\mathrm{keV}]}}} \tag{3.4}$$

with $c$ being the speed of light, $m$ the rest mass of an electron and $E_\mathrm{k}$ its kinetic energy. For electrons with a kinetic energy of 30 keV, this results in a de Broglie wavelength of $\approx 7$ pm.

To measure the angular spread of the electron beam, a small aperture mounted at target position is used. The distance from target position to the detector is known and so the angular spread can be obtained by measuring the spot size on the detector. If the spot is significantly bigger than the aperture, the diameter of the aperture can be approximated to zero. However, since the aperture always has a finite size, we are actually measuring an upper limit of the angular spread. In order to minimise the error due to the finite size of the aperture, the electron beam can be focused on the detector during the measurement.

Since we assume the spot on the detector to follow a Gaussian intensity profile, we can simply measure the full width at half maximum (FWHM) and calculate the RMS using the relation $\mathrm{FWHM} = 2\sqrt{2\ln 2}\,\mathrm{RMS}$.

We used a 50 µm aperture and measured the angular spread at different positions in the beam profile. From the average we calculated a transverse coherence length of 6.6 nm. Since the aperture was fairly big compared to the spot size we measured on the detector (143 µm FWHM), the calculated value is a lower limit, the actual coherence length might be even larger. However, we can conclude that the spatial resolution is good enough in order to obtain a good diffraction image from our samples.

A lower limit of the coherence length can also be estimated by measuring the width of the Bragg peaks in a diffraction pattern. The distance $d$ between two Bragg peaks is related to the inverse of the distance $a$ of the corresponding lattice planes, like the width $\Delta d$ of the peaks is related to the inverse of the coherence length $L_\perp$:

$$L_\perp = \frac{d}{\Delta d} \cdot a. \tag{3.5}$$

In figure 3.7 a section of a (highly averaged) diffraction image is shown as well as a line profile of the three visible Bragg peaks. The values obtained from this graph lead to a lower limit of the coherence length of 11 nm. Compared to the aperture measurement, this method seems to be not only simpler but also more accurate. This is due to the large size of the aperture used in the first method. Smaller apertures should lead to more accurate results. However, we found that apertures smaller than 50 µm are very difficult to adjust into the electron beam since most of the electrons are blocked and therefore the signal on the detector is very weak.

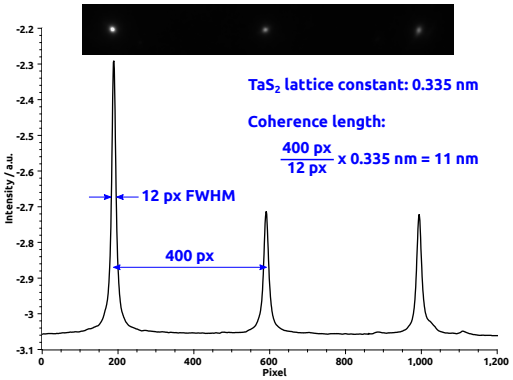


Figure 3.7: An estimation of the coherence length can be obtained directly from a diffraction image.

**Space Charge** Due to space charge effects, the electron pulse length increases quickly with propagation distance. To demonstrate that, simulations using the ASTRA code [39] have been performed, the results are shown in figure 3.8. The parameters were chosen to match the ones used in our experiments. The UV laser beam was assumed to follow a Gaussian profile in all three dimensions. The spot size on the cathode was set to 35 µm FWHM diameter and the pulse length to 150 fs FWHM. The electrons got accelerated to an energy of 30 keV and the field of the magnetic lens was adjusted in each case to result in the smallest electron spot size on the detector. The plot shows the dramatic pulse broadening for different numbers of electrons per pulse.

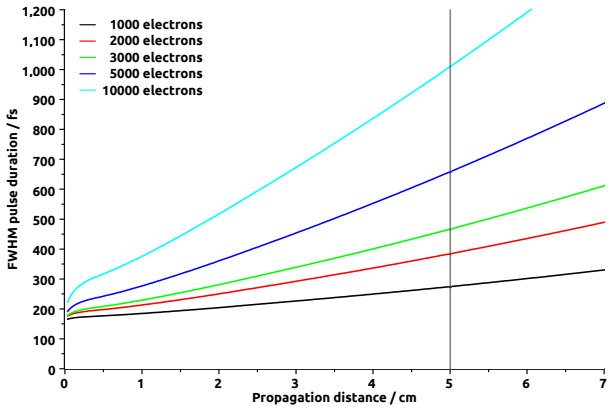


Figure 3.8: Due to space charge effects, the electron pulses expand quickly, like shown in these simulations. To keep a good temporal resolution, the electron number per pulse and the propagation distance to the sample should be kept small.

An initial broadening to about 250 fs occurs already during the acceleration in the first millimetre. This broadening is less severe the faster the acceleration happens and therefore the anode–cathode distance is kept as short as possible. In the following drift region, the pulses continue to broaden. Here the number of electrons per bunch plays a significant role since for 10000 electrons the pulses exceed a duration of 1 ps within 5 cm while a bunch containing 1000 electrons stays below 300 fs after the same travel distance.

Consequently, we prefer short travel distances and a small number of electrons per pulse in order to keep a good temporal resolution.

Thus, the magnetic lens was designed to be as thin as possible and the samples are moved as close as possible to the magnetic lens. A cathode–sample distance of only 5 cm is possible which means that we can achieve a pulse length of about 300 fs under realistic conditions. An electron number of less than about 1000 per pulse usually produces a very weak diffraction signal so that long measuring times would be needed in

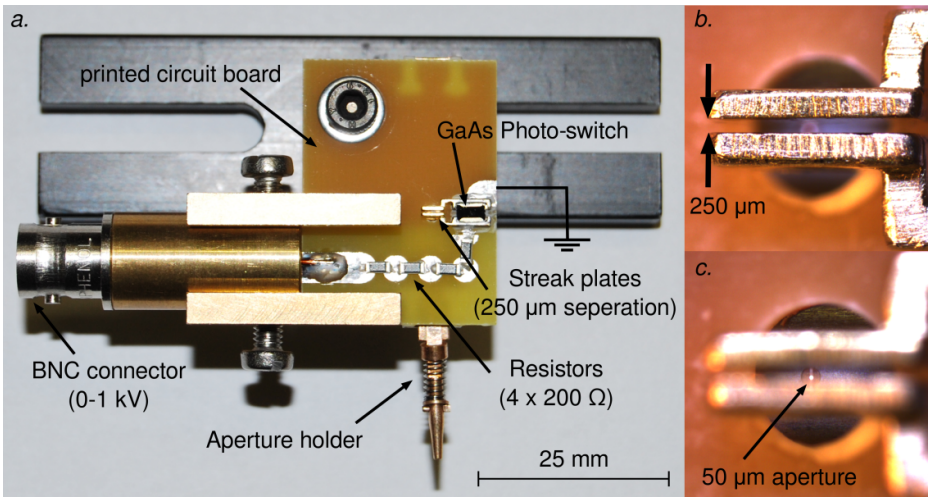


Figure 3.9: (a) Photograph of the streak camera. (b) Enlarged view of the streak plates. (c) Enlarged view of the aperture behind the streak plates.

order to capture a useful image. This is not advisable since it would make the experiment much more difficult and likely to fail.

The ASTRA simulations allow us to get an overview of the behaviour of the electron pulses in the sample region. However, many input parameters contribute to the simulation result. To be independent of changes and uncertainties in these parameters, we preferably want to measure the actual pulse duration under the current experimental conditions. The measurement procedure will now be described.

**Measuring the Electron Pulse Duration** Since the electron pulse length changes with propagation distance, we need to measure the pulse duration at the same position we place our sample. With a sample distance of 5 cm from the cathode we expect the pulse duration to be somewhere between 200 fs and 1 ps, depending on the number of electrons per pulse (see figure 3.8). A streak camera with the ability to measure such short electron pulses was developed in our lab [32].

The streak camera consists of two electrodes with a distance of 0.25 mm and a length of 3 mm (see figure 3.9). One electrode is initially charged up to 500 V. The electrodes are connected to each other via a GaAs photo conductive semiconductor switch (PCSS) which has a high resistance until it is triggered by a laser pulse. The laser pulse generates conduction band electrons, therewith reducing the resistance of the switch significantly. Thus, the two electrodes are shortened and the electric field between the electrodes begins to follow a damped oscillation of very high frequency (4.5 GHz). The first slope of this oscillation is linear for several picoseconds around the point where the field changes its direction. Only this part is used to streak the electron pulse. If the timing is aligned correctly, the first electrons in the pulse experience a field in one di-

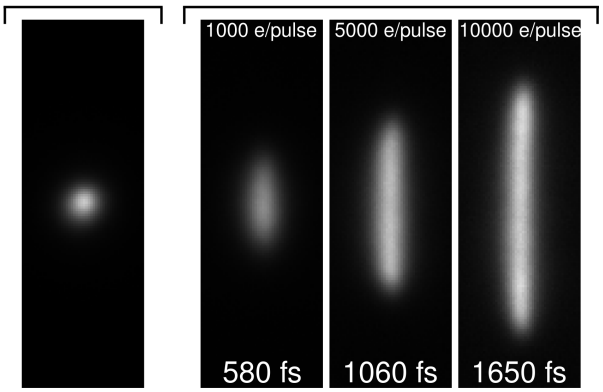


Figure 3.10: Streak measurements for different electron currents. The sample was positioned 7 cm behind the photo cathode. The left panel shows the unstreaked electron spot on the detector.

rection, the ones in the middle experience no electric field and the electrons in the end of the pulse experience a field in the opposite direction. On the detector a 'streaked' image of the electron pulse is visible. When delaying the triggering laser pulse slightly one can measure a shift of the streaked signal on the detector. Since the induced temporal delay is known one can easily find the calibration of streak length to real time and thus determine the duration of the electron pulse. More information about the design and operation of the streak camera can be found in [32, 35].

Figure. 3.10 shows images of the streaked signal on the detector for different numbers of electrons per pulse. The streak camera was placed at a typical sample position 7 cm behind the photo cathode. In the left panel, the streak camera was switched off and therefore the pulse is not streaked. The measured pulse durations are given as well.

**Beam Correction** Since the beam path length from the laser system to our sample position is about seven meters, a very slight change in the direction of the laser beam, originating early in the beam path, can make a significant difference in the beam position of both, pump and probe, on our sample. It is then very likely that we loose the spatial overlap of pump and probe beam. Since the samples in our case consist of small crystal flakes (not bigger than 100µm $\times$ 100µm), a small movement of the probe beam can also lead to the complete loss of the diffraction pattern.

To compensate for that, beam correction systems are included in both, the pump and the probe beam path. The mount of the last mirror in the probe beam path, before the frequency tripled laser beam enters the electron gun, is adjustable in fine steps by two computer controlled piezo motors. We wrote a computer program to track the centre of mass of one of the Bragg spots on the images taken with our detection camera. If the spot, which usually has a diameter of about 12 pixel FWHM, moves more than one pixel away from its original position, the program corrects this by adjusting the piezo mirror accordingly. The position is checked and (if necessary) corrected every two minutes which is sufficient in order to keep the beam stable for as long as the measurement runs. The beam correction system in the pump beam path works similar and is described in the pump beam section 3.2.

## 3.2 The Pump

We use 150 fs short laser pulses with adjustable intensity as our pump beam. The pump beam initiates the dynamics in the sample which result in a change of the atomic structure. The change can be reversible or irreversible. In the reversible case, the structure ideally should relax back on a nano- or microsecond time scale, so that the next pump pulse, (which arrives – in our case – a millisecond later at the same sample spot) will hit it in the original state and starts the same process again. If the process is irreversible, it can only be initiated once on a single sample spot. The sample then has to be moved to a fresh spot before the next pump pulse arrives, in order to start the same process again. This makes the experiment considerably more complex and thus we will concentrate on reversible processes only.

**Fluence** The pump beam has to be strong enough to trigger the dynamics in the sample, but should not permanently damage it. The actual value of the adequate fluence

depends on the sample and on the process to be observed but generally is in the order of 1–3 mJ/cm$^2$ (corresponding to about 5–15 GW/cm$^2$). It can be adjusted using either a variable neutral density filter or a combination of a rotatable half wave plate and a polariser in the beam path. Power losses due to the entrance window and the two metal mirrors inside the chamber were measured to be 10%. The beam size at sample position is measured like explained below and thus the actual fluence can be calculated from the power measured outside the chamber.

A lens situated outside the vacuum chamber, about 50 to 100 cm before sample position, is focusing the beam. The sample does not need to be in the focus, thus the beam size on the sample is adjustable by shifting the lens along the beam path or alternatively using a lens with a different focal length. Since our samples have a typical diameter of 100 µm, we set the beam diameter to more than 500 µm to ensure a homogeneous illumination and excitation of the entire sample.

**Translation Stage** The path lengths of both, the pump and the probe beam must be such, that both pulses arrive at the sample at exactly the same time (alignment for time zero). One has to take into account that the electrons move only with about a third to a fourth of the speed of light, depending on the accelerating voltage ($v = 0.33c$ for 30 keV, $v = 0.37c$ for 40 keV). Thus, the pump beam path effectively has to be a bit longer than the probe beam path. A translation stage is mounted into the pump beam path, like shown in figure 3.1. This allows us to change the arrival time of the pump beam (100 steps correspond to 300 fs delay) while the probe beam path length always stays constant.

**Beam Correction** When moving the delay stage, the position of the pump beam on the sample can change slightly but significantly due to imperfections of the stage. This can be corrected with a beam correction system similar to the one in the probe beam path (see figure 3.11). We take advantage of the fact, that the pump beam enters the chamber under an angle to the normal of the entrance window. The reflected fraction of the beam misses the last mirror above its mount and can be used to 'copy' the beam spot at sample position. A camera is mounted in exactly the same distance in the reflected beam, than the sample is situated in the transmitted beam path. Further attenuating of the reflected beam ensures, that the camera will not be damaged or saturated. Like in the probe beam path, the mount of the last mirror, before the beam enters the chamber, is adjustable by two piezo motors which can be computer controlled. A LabView program tracks the centre of mass of the beam spot on the camera and if necessary moves the piezo mirror such, that the centre of mass stays as close as possible to a given position. Since the mirror moves the pump beam in the chamber the same amount, also the laser spot on the sample stays at its optimal position.

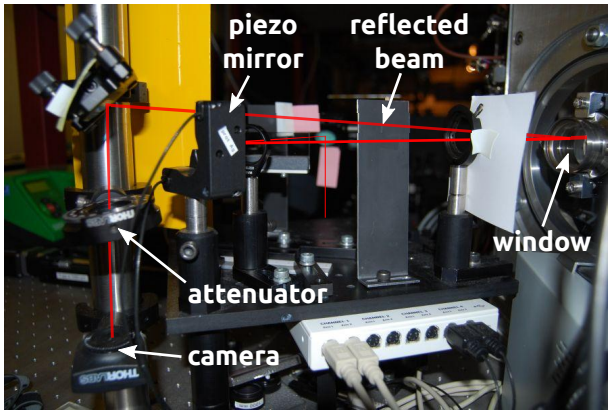


Figure 3.11: A part of the pump beam gets reflected at the entrance window of the chamber and is used to monitor the beam position and size on the sample.

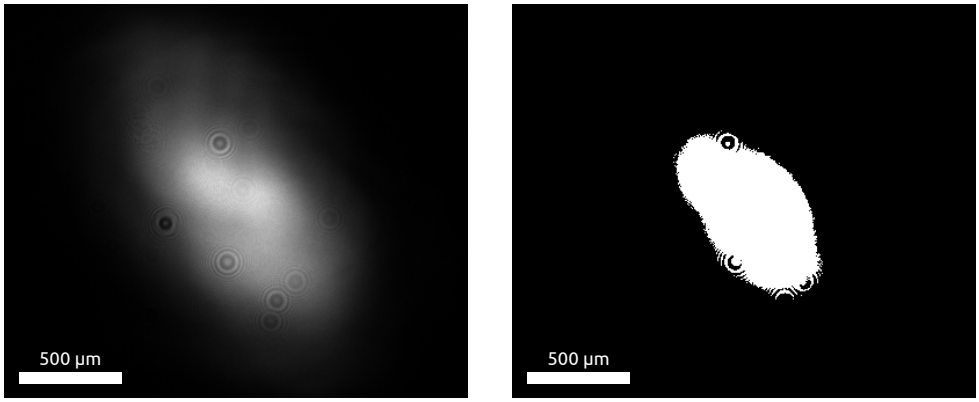


(a) (b)

Figure 3.12: (a) Photograph of the pump beam taken with the beam correction camera. (b) FWHM area of the pump profile shown in (a).

The centre of mass can be kept constant within $\pm 20$ µm for the duration of the entire experiment, which in some instances can exceed 24 hours. Translation stage imperfections as well as beam drifts are effectively compensated.

Depending on the fluence needed for the experiment it might be possible to only focus the pump beam very slightly, so that the spot on the sample is big compared to the size of the probed sample piece. If a relatively large sample area is pumped, the spatial overlap of pump and probe is easy to achieve and small movements of the beam are negligible. However, beam correction of the pump beam is still advisable, especially for long measurements and when using a low quality delay stage.

Without the two active beam correction systems in pump and probe beam path, we would not be able to do measurements exceeding half an hour, probably due to a small but noticeable drift in the laser beam direction.

**Pump Beam Profile** The most direct way to measure the pump beam at sample position is to use a thin carbon foil mounted on a support grid and take pictures of the shadow image while increasing the pump intensity step by step. Carbon foils are very strong and the laser only burns a hole where its intensity exceeds the melting point of carbon. Other thin foils would rather crack and break where the laser hits them and the so created hole is bigger than the actual laser beam and has an arbitrary, polygonal shape. The radius of the hole in the carbon foil, which is growing with increasing pump fluence, can be measured from the picture (the mesh size of the support grid is known and therefore functions as a scale). The relative pump intensity plotted over the hole radius gives the beam profile.

However, this method implies that the pump beam is strong enough to destroy the carbon foil. Since it is generally not necessary to have such a high energetic beam to perform FED experiments, the setup might not allow for this method. An easier way to measure the pump spot size is to simply measure the beam size of the 'copy' we observe with the beam correction camera. This is not as accurate as the carbon foil method which measures the beam directly at the sample position. But it is much simpler, gives an instantaneous result and the measurement can in principle even be performed parallel to an experiment. The exact position of the camera is not very critical as long as the beam is only slightly focused, which usually is the case.

A photo of the pump beam taken with the beam correction camera is shown in figure 3.12a. All pixels with values in the upper half of the intensity scale contribute to the beam size (white area in figure 3.12b). The small ring structures are generated by small dirt particles on the camera chip which are hard to remove. However, they do not affect the measured beam size relevantly, as long as they are not located in the brightest region of the beam. Each pixel of the camera has a size of 5.6 µm×5.6 µm and thus, the beam size can be calculated to be 0.35 mm$^2$ for the example shown in the pictures. For a circular beam this would correspond to a FWHM diameter of 700 µm which is a lot larger than the probe beam diameter of 200 µm (figure 3.5) or our sample size of 100 µm. Therefore, a homogeneous pumping of the sample is guaranteed.

## 3.3 Vacuum System

The vacuum chamber was designed primarily to be very flexible since the whole setup was still under development. It consists of a stainless steel frame of hexagonal shape and six aluminium side walls which are removable and exchangeable (see figure 3.13). Two extra plates allow us to have one plate in the workshop to have necessary changes done while in parallel being able to work with a functioning chamber. The chamber has a big removable lid made from perspex through which we can overview the inside of the chamber. Three more windows on the side plates help with that task.

Most of the many plates and flanges are sealed with rubber O-rings (mostly Viton®) which again provide for a flexible chamber design but are not made to withstand ultra high vacuum. Most of the items situated inside the chamber, like the three translation stages and two piezo mirror mounts, are vacuum compatible (specified for a vacuum of up to $10^{-6}$ mbar) but some are not. This includes mirror mounts, some cables and plugs and other small things. Everything gets cleaned with acetone in an ultrasonic bath and/or wiped with ethanol and is handled with gloves before it is inserted into the chamber. An oil filter is positioned between the rough pump and the two turbo pumps to prevent oil from the rough pump reaching the chamber.

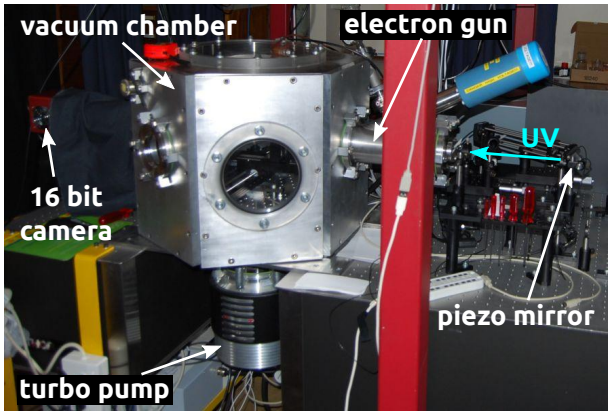

Figure 3.13: Photograph of the vacuum chamber.

The volumes of the main chamber and the electron gun are only connected through the 2 mm opening in the anode cap. Therefore we use two turbo pumps, one attached to each of those two volumes. The minimum pressure we reach is about $1 \times 10^{-6}$ mbar (measured inside the main chamber).

We use nitrogen to ventilate the chamber in order to prevent humidity to condense on the surfaces. This improves the time needed to evacuate the chamber. When opening the chamber for only a few seconds, a pressure of $10^{-6}$ mbar can be reached after about one hour of pumping. Keeping the chamber open for several minutes however, leads to a pumping time of several hours, even if nitrogen was kept flowing as long as the chamber was open. We therefore pump the chamber mainly over night so we can start experimenting the next morning.

## 3.4 Improvements

The main challenges with our current FED system, which was introduced in this chapter, are a decay of the photo cathode (see chapter 5.2) and the pulse broadening due to space charge effects. There are however ideas of how to overcome these limiting factors. A next generation electron gun is therefore currently under development at the Laser Research Institute and further development of the system is (and will be) an important part of the group's work.

The decay of the cathode efficiency can be eliminated by using bulk gold instead of only a 10 nm thin layer of gold. Obviously, the laser cannot penetrate through a thick layer of gold and therefore the photo cathode needs to be illuminated from the front. The design of the laser beam path is challenging, since an incoupling mirror needs to fit in somewhere in the already tightly packed region between the cathode and the sample. Our second generation electron gun will include the option of using a front illuminated cathode.

The most popular idea to overcome the pulse broadening is to recompress the expanding electron pulse. Several methods have been proposed by different groups, including ours [31, 40–43]. They all make use of the fact that the electron pulses have a nearly linear chirp (longitudinal position–momentum correlation) originating from the repelling coulomb forces inside the bunch. Simplified this means that the electrons in the front of the pulse are faster than the ones in the back. By turning this habit around, the bunch will compress until again the space charge forces will prevail and tear it apart. In the position of maximum compression, short (subpicosecond) pulses can be achieved even with very high electron numbers. This leads to much shorter measurement times, in the extreme case even a single shot experiment becomes possible this way, like shown by van Oudheusden *et al.* [44]. And further, since the beam path can be much longer, more electron optics can be included which will enhance the image quality and will also relax the requirements on the sample size.

A compact compressor was designed in our group and showed promising first results [43]: we were able to take a diffraction pattern using pulses containing 26000 electrons, compressed to a duration of $< 750$ fs. The system still needs some development but will eventually improve our FED setup significantly. The compressors simplicity and compactness are the main advantages over alternative compressor systems.

Another idea was shown in [45, 46], where long electron pulses were used in combination with a streak camera in order to measure the dynamics of a photo induced process. Instead of scanning the delay stage step by step, an adjustable time window could be observed within one streaked diffraction image. The results of a conventional measurement could successfully be reproduced within a considerably shorter measurement time.

# 4. Sample Preparation

In order to produce a good diffraction signal with clear spots and little background, the sample needs to fulfil some requirements defined by our setup. First of all, the sample must be free standing and have a thickness in the order of the mean free path length of the electrons in that material. Since this can result in thicknesses of less than 100 nm, sample preparation is one of the major challenges in the field of femtosecond electron diffraction.

Since our electron beam is fairly big at sample position (several hundred micrometres in diameter), the sample should ideally be of similar size. If the sample is much smaller, only very few electrons get diffracted and the signal-to-noise ratio is too low to observe a good diffraction pattern. This too is a demanding request, keeping the extremely small thickness required in mind. The samples used in the experiments presented in chapter 6 had a size of roughly $100\mu m \times 100\mu m$.

In addition, the sample might need to be prepared in respect to a certain crystal axis or layer, depending on the structural changes to be observed.

The samples are usually mounted on a support grid like they are commonly used in transmission electron microscopy (TEM). The meshes we used have a diameter of 3.05 mm and hole sizes in the order of 100 µm. Carbon coated meshes are available for better support of very sensitive samples. The thickness of the carbon film is typically in the order of 10 nm.

It is important to ensure that the sample is grounded while performing an electron diffraction experiment. Otherwise the sample charges up and the electrons get deviated from their original direction. Therefore the mount should be made of metal and if a mesh is glued onto it, the glue should not insulate the mesh from the mount. We

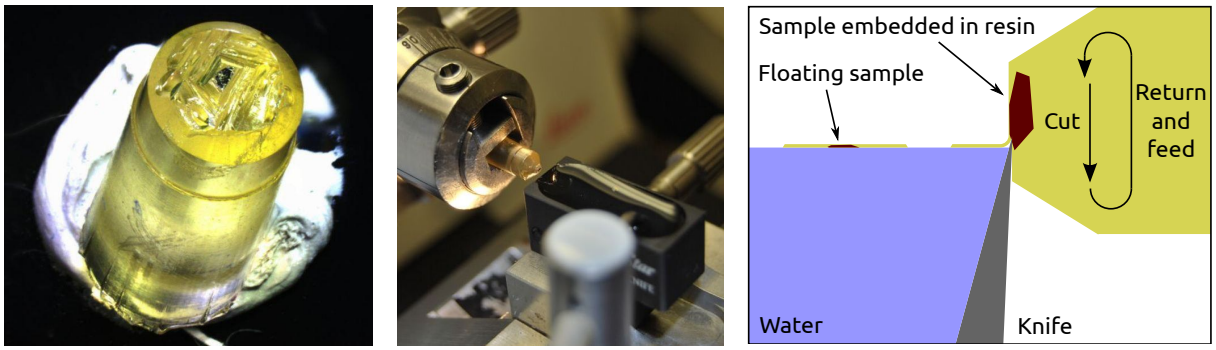


(a) (b) (c)

Figure 4.1: Sample preparation: (a) A small piece of $TaS_2$ glued onto a resin cone. The cone has a diameter of 5 mm. (b) The resin cone is mounted into the moving arm of an ultramicrotome. (c) Principle of the cutting process of an ultramicrotome.

found that a small drop of silver paint holds the mesh while providing conductivity.

There are different methods to achieve thin freestanding samples, two of which will be introduced in the following paragraphs.

**Scotch Tape Method** For quasi-two-dimensional crystals with only a weak interaction between the layers in one direction, it is possible to cleave them with scotch tape. When stuck between two pieces of tape, the crystal will split between two crystal layers when pulling the two tape pieces apart. Repeating this process several times can lead to a very thin crystal film – in the case of graphite even single crystal layers (graphene) were achieved with this method [47]. The challenge is to take the film off the tape without leaving any glue stuck on it. This is managed by dissolving the tape with acetone or another suitable solvent. If the film is floating on the solvent it can be picked up with a support grid.

Since our sample $TaS_2$ has a quasi-two-dimensional structure, it should theoretically be possible to prepare it with this method. However, we did not find a working combination of scotch tape and solvent to get the sample off the tape. We decided to rather use an ultramicrotome to cut the sample, where we also have much better control of the sample thickness. Here, we sometimes found it helpful to remove the top layers of the bulk crystal by using scotch tape. Doing this just before cutting the sample with the ultramicrotome can simplify the alignment of the knife parallel to the crystal layers.

**Cutting Samples with an Ultramicrotome** Some samples are grown as bulk crystals which can reach dimensions in the order of millimetres and are best prepared by cutting them with an ultramicrotome. In figure 4.1 the principle of the cutting process is shown.

Usually, a small piece of the sample material is embedded in a piece of resin which becomes hard when baking it. For our crystals it turned out to be a better alternative to simply glue it onto the flat surface of an empty resin cone instead (figure 4.1a). Like this we have better control of the orientation of the sample. This is important since we

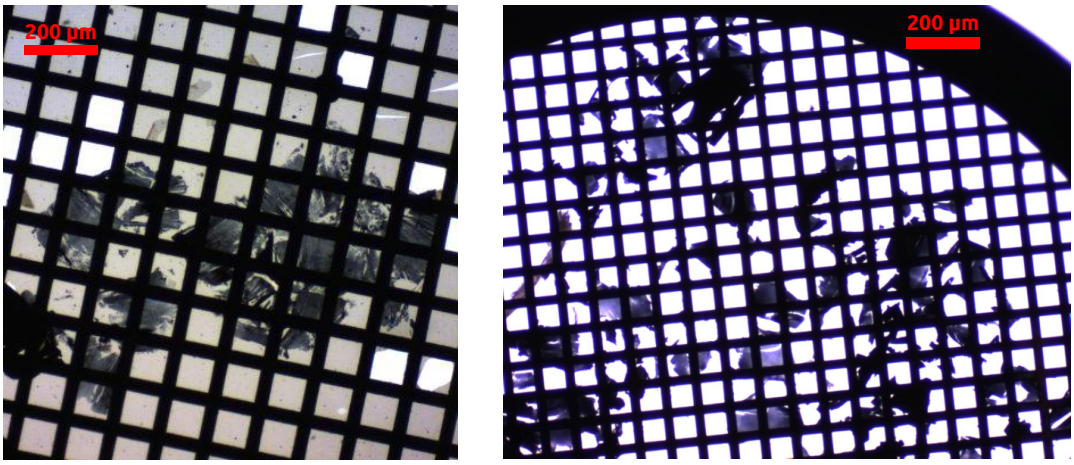


(a) (b)

Figure 4.2: (a) 30 nm thin $TaS_2$ samples on a carbon coated mesh. The carbon layer broke at some places. (b) 30 nm thin $TaS_2$ samples on a mesh without a carbon layer.

need to cut the transition metal dichalcogenides parallel to the two-dimensional layers in order to see the hexagonal crystal structure within the layers as well as the CDW superstructure in the diffraction pattern.

The resin cone with the sample is then mounted into the moving arm of the ultramicrotome (figure 4.1b). After careful alignment in respect to the knife, the microtome moves the sample with a constant speed over the knife, shifting the sample forward in small steps between each cut (figure 4.1c). The knife is attached to a boat filled with water and the water level is carefully adjusted to not form a meniscus on the knife's edge. If everything is optimally aligned, the thin slices will nicely float onto the water surface where they can be collected with a support grid.

For preparation purposes or for softer samples a simple glass knife can be used, while harder materials like $TaS_2$ or $TaSe_2$ have to be cut with a diamond knife. Sample thicknesses down to a few nanometres can be achieved with an ultramicrotome.

Transferring the floating films onto the mesh can be challenging as well. Larger samples easily break into small pieces which are not suitable for our experiments. Since the film has to be taken out of the water, the mesh naturally will be wet afterwards. For those small structures the surface tension of the water plays a significant role. A drop hanging on the mesh can be removed with filter paper but the water films which form in the mesh holes pop like bubbles when they dry. If the sample is thin and weak, it pops together with the water and there is nothing left on the mesh. In that case one can use meshes covered with a thin carbon film to collect the samples on. Since carbon is very strong, it acts as a support for the sample without having a large influence on the diffraction signal. However, it still increases the background signal and consequently we want to avoid using carbon meshes, if possible.

As a help to guide the floating samples onto the mesh, an eyelash mounted on a toothpick is a very useful tool.

When the meshes with the thin samples on it have dried, we inspect them with an optical microscope. Two examples of meshes containing 30 nm thick $TaS_2$ slices are

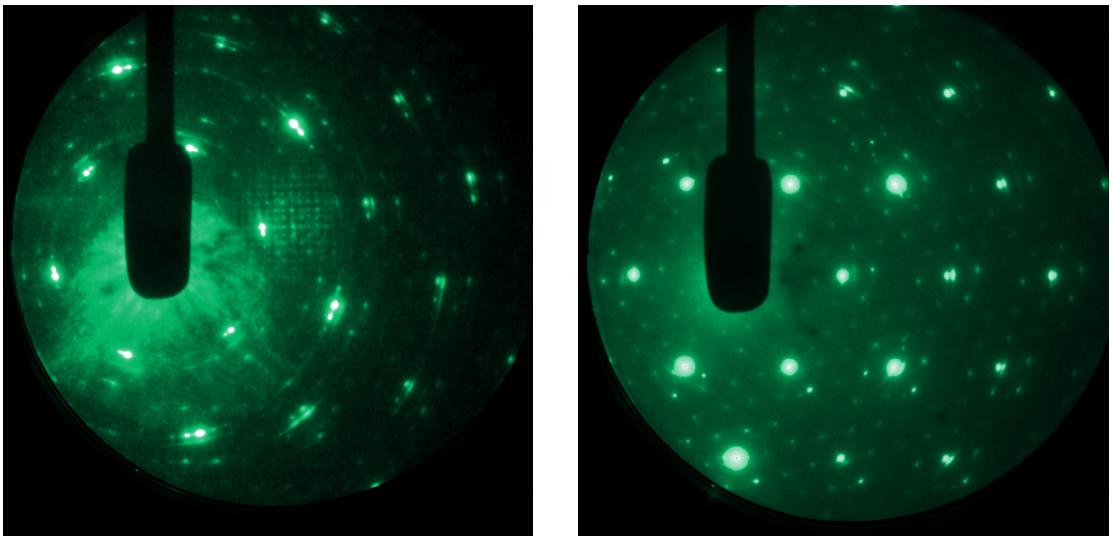

(a) (b)

Figure 4.3: (a) Diffraction pattern of a sample on a mesh, optimised on one crystal flake. No aperture was used. (b) Diffraction pattern of a sample mounted on an aperture. Background signals are blocked by the aperture.

shown in figure 4.2, one on a carbon foil and the other one on a plain mesh. Only now we see whether the cutting was successful and suitable sample pieces were achieved. Promising samples should at least fill one mesh hole completely or be of similar size and look homogeneous. The thickness should be right, which will only be confirmed when probing the sample piece with our electron beam but might be estimated by eye after gaining some experience with that sample (for example the dark looking piece on the left edge of figure 4.2a will probably block all electrons).

If the samples are considerably smaller than the electron beam, a diffraction pattern might still be seen when focusing the electrons rather somewhere between the sample and the detector. The pattern will be out of focus but brighter since the electron beam size on the sample is reduced and consequently more electrons are moving through the crystal flake. Even if such a diffraction pattern is not suitable for a time resolved experiment, it can be used to check if the thickness of the sample is acceptable.

**Mounting Samples on Apertures** The size of our electron beam at sample position (200 µm diameter, see section 3.1) is considerably larger than the biggest sample pieces we managed to cut and float onto a mesh. Therefore, by simply mounting the sample as it is into the beam path, the diffraction pattern is likely to show features of neighbouring crystal flakes or a high background due to the surrounding carbon foil (which in principle is redundant where it does not support any sample). The crystal flakes are in general oriented in arbitrary directions so that two neighbouring flakes would indeed show the same pattern, but rotated in respect to each other. This results in double Bragg peaks or in extreme cases in the formation of concentric rings consisting of many Bragg peaks of different intensity (see figure 4.3a). Furthermore, a shadow image of the mesh is often visible additionally to the diffraction image. The UV beam which is focused onto the cathode surface to produce the electron pulses, passes through the

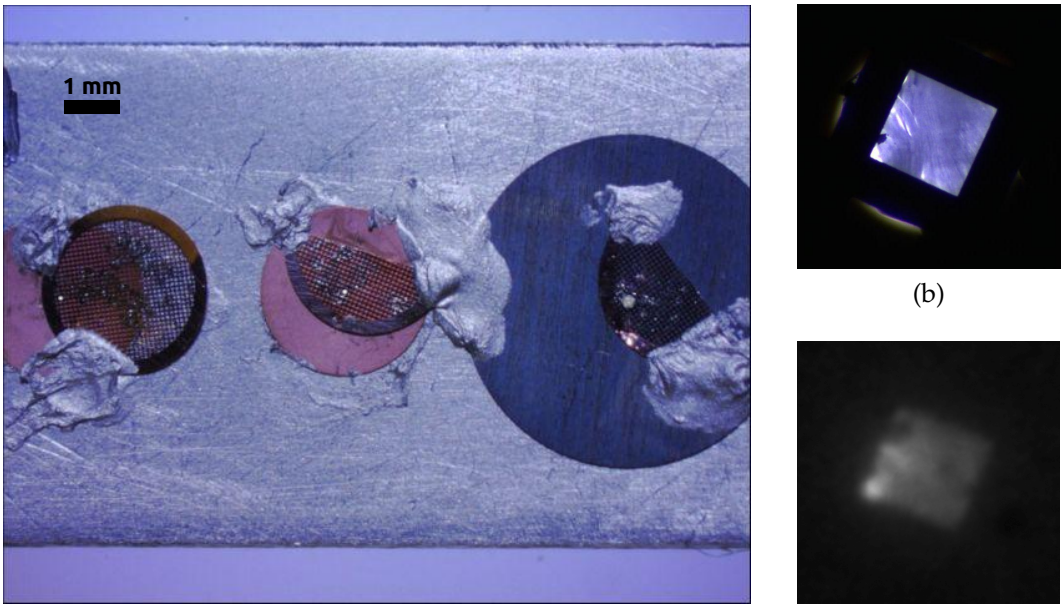


(a) (b) (c)

Figure 4.4: (a) Photo of a sample mount holding three apertures (two 100 µm and one 250 µm) with samples glued onto them. One mesh has been cut into two halves. (b) Microscope image of a good sample on an aperture. (c) Electron shadow image of the same sample.

thin gold layer and expands until it reaches the detector where it creates the shadow image. This is also visible in figure 4.3a.

To single out the good sample piece and block everything else, it was found very helpful to use an aperture of a diameter comparable to the sample size. The aperture is glued onto a sample mount using silver paint. The mesh is then placed on that aperture such that the good sample piece is centred on the aperture. It is fixed carefully with a small amount of silver paint and its position can be optimised while the silver paint is still pliable. If more than one good sample spot is found on the same mesh, it might be possible to cut the mesh into several pieces, each containing one of the good spots, and mount them onto several apertures. A sample mount prepared in this way is shown in figure 4.4.

Preparing samples this way requires a stereo microscope with good illumination as well as a steady hand and plenty of patience. It is, however, worth the effort since not only the quality of the diffraction image improves significantly (see figure 4.3), but also the alignment in the chamber becomes much simpler (see chapter 5).

Good looking samples are mounted into our electron diffraction setup to check the quality of the diffraction signal. The best sample piece is used for the experiments.

# 5. Measurement and Analysis

The first step towards a successful FED experiment is to prepare a suitable sample which produces a good diffraction pattern in our setup. This was described in chapter 4. Once this is achieved, a few more preparations are necessary before finally starting the actual experiment. During a measurement, many pictures are collected which have to be analysed in order to obtain interpretable data. The steps we take to align the setup, run the experiment, verify and analyse the obtained data are presented in this chapter.

## 5.1 Measurement Strategies

Like demonstrated in both, simulations and measurements (section 3.1), the electron current should be kept low in order to ensure a short pulse length at sample position. However, we still need enough electrons to produce a clear signal on the detector. By experience we learnt that about $1 \times 10^8$ electrons are necessary to create a reasonable diffraction pattern. This can be achieved for example by allowing 500 electrons per pulse and integrating over $2 \times 10^5$ pulses. The pulse duration then stays below 500 fs (for a sample position 6 cm behind the photo cathode) and for a 1 kHz repetition rate a camera exposure time of 3.5 minutes is necessary. Taking ten data points for different time delays, this already leads to a measurement duration of more than half an hour.

Changes in the signal caused for example by slow fluctuations in the laser intensity or by temperature changes of the sample mount can be misinterpreted as structure changes induced by pumping the sample. To avoid that, it has been found advantageous to take images with only one minute exposure time for every time step and then repeating the whole scan several times. In the end we can integrate over all the images taken for the same time delay to get one effective scan with bright clear pictures.

We can now get rid of long term changes in the signal since we can correct for movement of both beams, pump and probe, after every minute. Signal changes induced by the pump beam should occur in every single scan and always at the same position of the delay stage. Events happening only once during the whole measurement are due to other reasons and should not be included in the analysis.

Another advantage is, that we might already get an idea after one or two scans if the scan is worth continuing or not and we can repeat the scans until we collected enough data to be able to perform a detailed analysis – the more scans we can average over, the better the signal-to-noise ratio becomes. Bad scans can be excluded from analysis. For example if the signal is too weak, the scan should not be used for analysing since it would add more to the noise then to the actual signal. By only taking the 'good' scans for analysis we ensure that we get the best possible results. We then average over all the good images taken at one position of the delay stage so that we get one diffraction

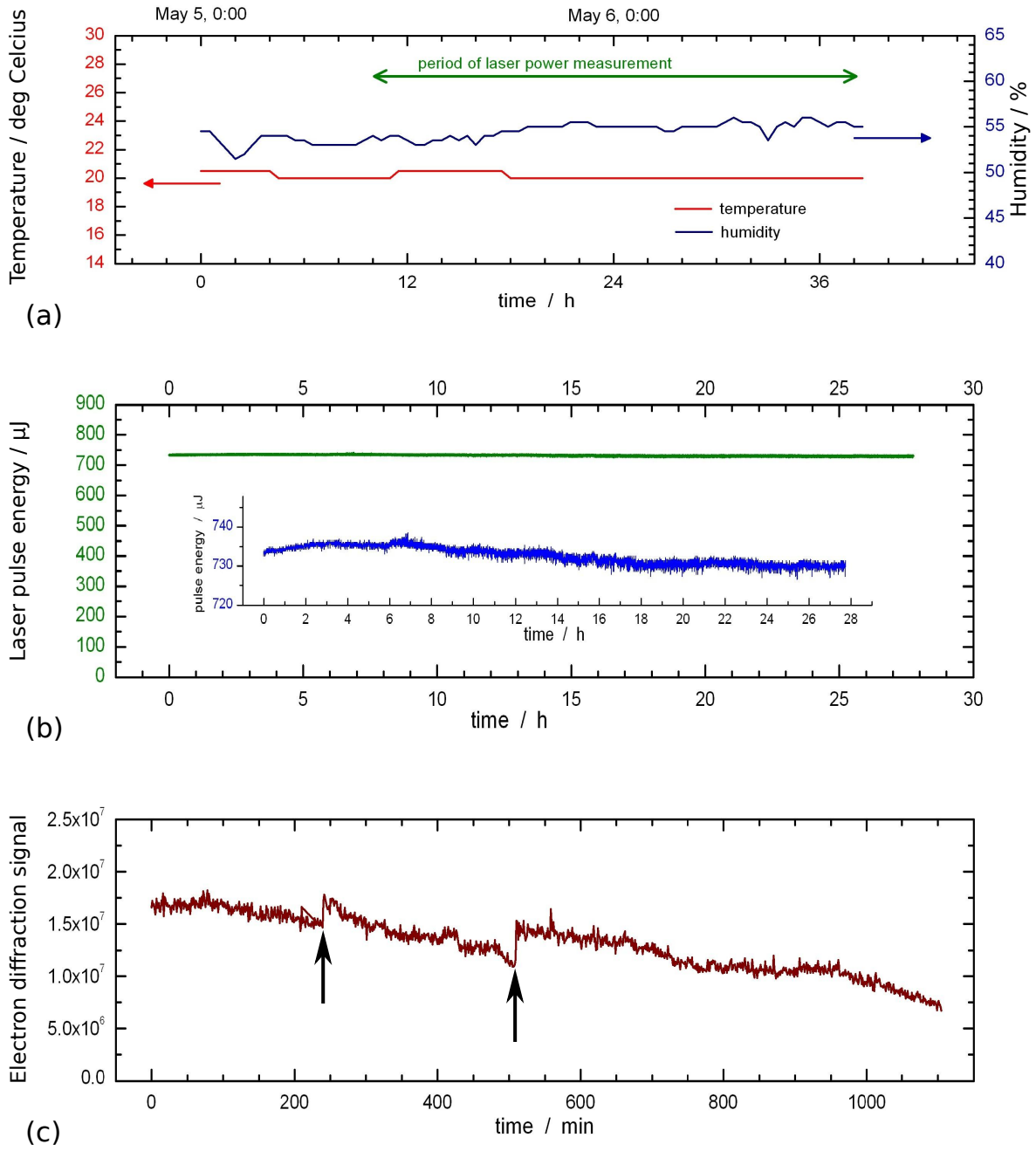


Figure 5.1: (a) The conditions (temperature and humidity) in the lab can be kept constant over long periods of time, like shown by this measurement over a period of 38 hours. (b) This helps to keep the laser intensity very stable, here a measurement over 28 hours is shown. (c) The decrease in the electron diffraction signal is due to an irreversible decay of the photo cathode performance (see text). The signal can be corrected a few times by slightly moving the UV beam on the cathode.

image for each time step.

Another important method to get rid of unwanted changes in the signal is to take two images per time step: one with the sample being pumped and one with the pump beam blocked. Changes in the signal of the 'unpumped' image indicate unwanted long term changes and can be taken into account when analysing the data. Simply subtracting the 'unpumped' images from the 'pumped' ones cancels these unwanted changes out. The resulting images show changes in the diffraction pattern for each time step in respect to the unpumped state and this is exactly what we want to measure.

These methods lead to even longer measurement durations of several hours and thus to strict requirements of the experimental conditions in the lab.

## 5.2 Stability

We learnt, that the temperature and humidity in the lab directly influence the laser output intensity and thus have to be kept very stable over a long time period. Therefore, all the windows in the lab have been insulated with aluminium foil and an air conditioner is running permanently to keep the temperature constant. As one can see in figure 5.1a and b, the conditions can be very stable over long times. The weather only rarely has a significant effect on the laser performance, usually during drastic weather changes. By constantly logging the conditions in the lab, we can check afterwards if they could possibly explain changes we observed in our signal.

Since every second picture is taken without the sample being pumped, for an ideal measurement they should all look exactly the same during the whole scan. To compare the signal in those images, in every picture we cut out one particular Bragg spot and integrate over its intensity. These numbers are plotted in figure 5.1c for a measurement over 18 hours. The graph shows a slow but steady decrease in intensity with the exception of several steps, indicated by arrows. At these points we interrupted the measurement and adjusted for a better signal. Without doing so, the graph would show a constant decrease in intensity of our signal.

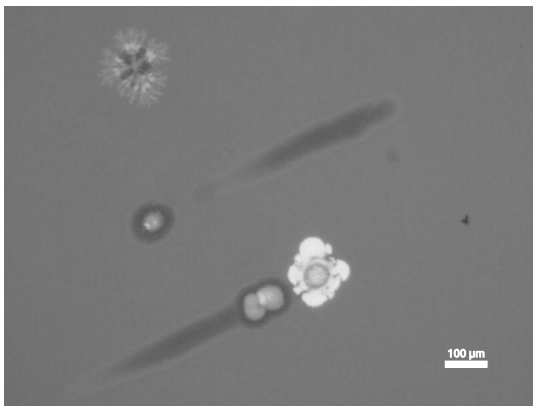


Figure 5.2: Photograph of the surface of a used cathode. Damages in the gold layer are due to UV beam exposure and discharges which are probably induced by small dirt particles on the surface.

This decrease results from a decay in the efficiency of our photo cathode. The UV laser intensity stays constant, but produces less and less free electrons from the gold film. The reason for that is a slow ablation of the thin gold layer due to the constant exposure to UV light. Figure 5.2 shows a photograph of a spot on the cathode which has been used for several weeks until it hardly produced any photo electrons. We found that the gold layer was removed at this position as can be seen in the picture. To recover the signal strength, we slightly move the UV beam on the photo cathode until we hit a spot, where the electron production rate is still high. When using a fresh spot, we often observed a fast initial drop of the electron signal strength followed by a slower decay.

Since the decay is nonreversible, from time to time we have to open the vacuum chamber and turn the cathode in its mount by about 45°. After doing so a few times, we have to replace the photo cathode with a new one. The decay of the photo cathode is slow enough in order to be able to take long measurements, as long as the UV laser intensity stays below ≈1 mW. Higher intensities result in a faster decay. But since we need to operate the gun with a low electron current to keep a good temporal resolution, we work in the low intensity regime anyway.

## 5.3 Preparing and Running the Measurement

Before starting the measurement, a few things have to be checked and aligned. The measurement is then run automatically by a computer program. These points are described in detail in appendix A, an overview is given here.

**Preparing for the Measurement** The electron beam should be aligned such that it moves along the symmetry axis of the magnetic lens. If this is the case, the electron signal on the detector changes its size but not its position when the lens current is varied. The sample is then moved into the electron beam and the shadow image is observed on the detector. If the sample is mounted on an aperture, alignment is simply done by optimising the aperture into the focused electron beam. If the sample is not mounted on an aperture, the shadow image will show the mesh with sample pieces on it. One piece can be chosen and moved into the centre of the electron spot. After focusing the beam, a diffraction pattern should be visible which can now be optimised.

The spatial overlap of pump and probe has to be ensured, which is done with an aperture (either with a sample on it or without). First, the aperture is aligned into the electron beam, then the pump beam is adjusted onto the aperture. During the measurement, the beam correction systems in both beam paths keep the beam positions stable and thus prevent a loss of the overlap.

The beam paths of pump and probe are designed such, that both beams arrive at sample position at approximately the same time. Fine adjustment of the timing can be done by moving the translation stage placed in the pump beam path. First, we need to find the stage position for which the two pulses are temporally overlapped at the sample (time zero position). This can be achieved with the help of the streak camera (rough alignment), an aperture or a suitable sample. A sample showing a drastic, long lived change in the diffraction pattern when being pumped can be very effective in finding the time zero position accurately. Later, we want to scan around this position in small steps to resolve the structural changes triggered by the pump pulse.

The electron beam current is adjusted such that the diffraction peaks are strong but not saturated on a one minute exposure image. The pulses should not contain too many electrons in order to keep a good temporal resolution (see figure 3.8). When everything is aligned and the diffraction pattern looks good, the measurement finally can be started.

**The Measurement Program** A computer program written in National Instruments LabView [48] controls all the different steps during a measurement, so that data can be collected without somebody being present all the time. The program was written mainly by myself and is explained in detail in Appendix A.2.

The starting position on the stage as well as the ranges and step sizes for the wished scan can be defined in the program. Several ranges with different step sizes can be selected. This enables us to do fine steps close to time zero and then increase the step size in order to observe the longer time scales as well.

A region of the diffraction image containing one Bragg spot can be selected. This spot will be tracked during the measurement and its position will be optimised whenever necessary. The pump beam will be observed with the beam correction camera and also optimised when necessary.

For each step, the program will take two diffraction images, one of the pumped and one of the unpumped sample. When the scan is finished, the program automatically starts a new one. This goes on until either the diffraction signal gets too low, a specified number of scans is completed or the program is aborted by the user. All images are saved in one folder per scan with relevant information stored in a separate log file.

Since measurements usually take several hours, we often let them run overnight. Via a remote desktop connection we are able to connect to the lab computer from any place connected to the Internet. This enables us to check the measurement from home and stop it, if required. The laser can be switched off remotely as well.

## 5.4 Analysis

Like described previously (section 5.1), from the several scans taken the acceptable ones are selected and averaged so that we consequently get one effective scan which we use for further analysis. Depending on the sample and the process to be observed, different analysis methods are used. Some possibilities are described in this chapter. All software used for analysis was written in LabView [48]. Most of the programs were written either partly or completely by myself.

**General** The pictures of the diffraction pattern can be calibrated with the help of the known diameter of the phosphor screen (40 mm). Consequentially, the distance $r$ from the centre of the main beam to each diffraction spot can be measured in millimetres. The distance between sample and detector (camera length $L$) is also known and thus

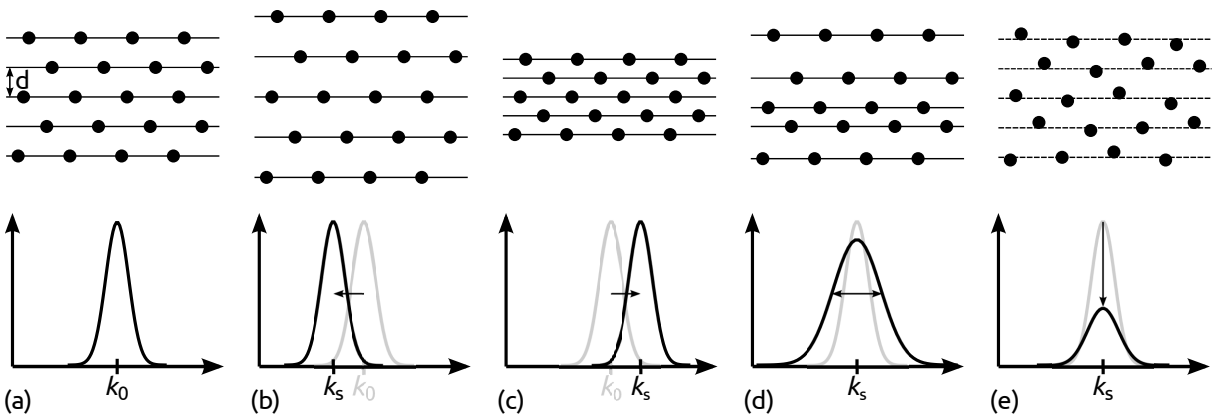


Figure 5.3: Changes in the crystal structure are visible as changes in the diffraction pattern: (a) Original crystal structure and corresponding diffraction peak. (b) Expansion and (c) contraction of the crystal result in a shift of the peak. (d) Fluctuations in the lattice spacing broaden the peak. (e) Heating decreases the signal strength.

the measured radius can be converted to the scattering angle $\vartheta$ (the angle between the original beam direction and the path of the diffracted electrons is $2\vartheta$). Since this angle not only depends on the distance $d$ between the lattice planes which lead to the corresponding diffraction order but also on the energy of the electrons, it is advisable to convert it to a more general parameter which is completely independent of any experimental conditions. Commonly the scattering vector $k_s$ is used for this purpose:

$$k_s = 4\pi \frac{\sin \vartheta}{\lambda} = \frac{2\pi}{d}, \tag{5.1}$$

where $\lambda$ is the de Broglie wavelength of the electrons (see equations (3.2) and (3.4)).

This equation allows us to interpret the changes we observe from one diffraction pattern to the next (see figure 5.3): A shift of the diffraction peak, visible in the diffraction pattern as a change in the radius $r$, means a change in the distance $d$ of the lattice planes. An increasing radius corresponds to a decreasing lattice spacing and vice versa (b and c). A broadening of a certain diffraction peak, which in principle is a partial shift in both directions, means that the distance of the corresponding planes varies inside the crystal (d). The integral over the diffraction peak stays the same in this case. When losing the periodicity of the lattice, for example due to a heating process, the diffraction signal (peak value and integral) weakens (e) [49].

Since the changes in the diffraction pattern we are looking for can be very small, a careful analysis is necessary.

**Analysis of $TaSe_2$** A typical diffraction image from a 100 nm thin film of $TaSe_2$ taken at room temperature shows the bright hexagonal Bragg pattern produced by the crystal lattice as well as the characteristic $\sqrt{13}$ structure of the commensurate CDW (see figure 5.4a). The intensity of the CDW peaks is only 1–2 % of the lattice Bragg peak intensity and typically one to ten times higher than the background noise (see figure 3.3). When pumping the sample, we expect the intensity of the diffraction spots, especially the CDW spots, to change. Thus, we need a method to obtain a suitable value describing the intensity of the spots in each image. Since the lattice Bragg peaks will show different dynamics compared to the CDW peaks, we need to analyse both types separately. In the end we can plot the values over the temporal delay between pump and probe pulses and interpret these curves to learn about the structural changes in the crystal lattice.

Our home written analysis software automatically detects the positions of the Bragg peaks and allows to select the Bragg spots suitable for being analysed (see figure 5.4a). Bragg spots on the edge of the detector or overlapping an interfering background signal should not be used. Each Bragg spot is surrounded by six CDW spots. To describe the positions of the CDW peaks relative to their central Bragg spot, a mask can be adjusted like shown in figure 5.4b. The same mask is then used to locate all the CDW spots around the selected Bragg spots in the image. Since not all CDW spots are clearly visible, some might be off the screen or behind the beam block and some are overlapping an additional not CDW related spot, every single CDW spot can be deselected if necessary.

The signal of the CDW spot is in general quite weak (in the order of 1 % of the lattice Bragg peaks) and thus it is important to take the background into account. The general CDW mask, rotated by 30° and placed at every selected Bragg spot, is used as a background mask (red in figure 5.4). For every deselected CDW spot, a background

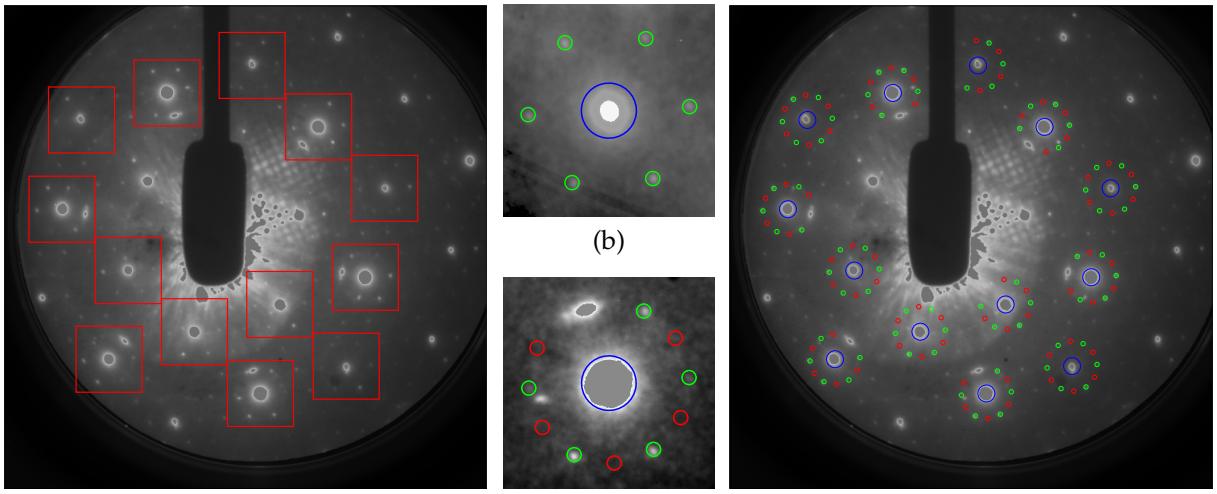

(a) (b) (c) (d)

Figure 5.4: Choosing the masks for analysis: (a) 13 Bragg spot environments are selected for further analysis. (b) The CDW mask relative to the central Bragg peak can be adjusted to fit the peak positions and size. (c) The background mask (red) is generated automatically by rotating the CDW mask (green) by 30°. For each Bragg environment, unsuitable CDW and background spots can be deselected. (d) In the end, three final masks are generated for the entire diffraction image: for Bragg signals (blue), CDW signals (green) and background (red).

spot has to be deselected as well (see figure 5.4). In the end this results in three masks for the whole diffraction image, like shown in figure 5.4d. These masks are saved in a file and used for all images of the measurement.

Integrating over the background pixels (red mask) and dividing by the number of pixels inside the mask, gives us an average background value which we subtract from all the other pixels. We then integrate over the pixels defined by the two other masks (blue and green) which results in two values per image describing the intensities of the Bragg signal and the CDW signal respectively.

The analysis so far will be done for all the images of the scan, the pumped as well as the unpumped. At this point the result from each unpumped image will be subtracted from the corresponding result of the previous pumped image. By dividing this number again by the unpumped value, we obtain the relative intensity change of the Bragg and CDW signals. Therefore, these values are around zero when the sample is not pumped (before time zero) and at minus one when the signal is lost completely.

The resulting values for the intensity of the Bragg and CDW spots are plotted over the time delay. Measurement results are shown and discussed in chapter 6.

**Analysis of $TaS_2$** The analysis of the $1T$-$TaS_2$ measurements is similar to the one just described. However, we now have to analyse not only one but two different CDW signatures. Therefore, two CDW masks can be chosen separately and the background mask is now adjustable as well. The analysis of the Bragg spots and the nearly commensurate CDW spots did not change. The background should be chosen as far away from any CDW spot as possible, but still in the same distance from the central Bragg peak (see figure 5.5b). Again, the resulting curves show the relative changes of the intensities where the signal strengths in the unpumped images serve as reference.

The unpumped reference images do not show a signal of the incommensurate CDW and therefore it is not possible to calculate changes of the incommensurate signal rel-

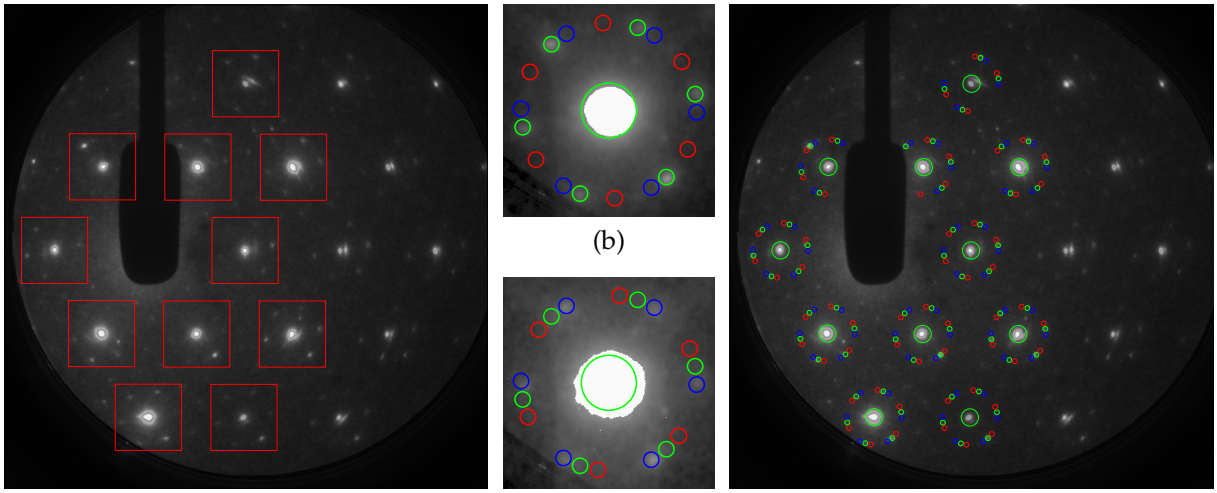

(a) (b) (c) (d)

Figure 5.5: Analysis of $TaS_2$ measurements: (a) Bragg spot environments can be selected for further analysis. (b) For analysing the nearly commensurate CDW signal (green), the background (red) should be away from the CDW spots. (c) When analysing the incommensurate CDW signal (blue), the background should be at the same distance from the nearly commensurate spots in order to compensate for the influence of the stronger signal. (d) Four final masks are generated for the entire diffraction image: for Bragg signals (big green circles), two CDW signals (green and blue) and background (red).

ative to its room temperature state. However, we can use the unpumped signal of the nearly commensurate CDW as a reference and calculate the relative change compared to the nearly commensurate CDW at room temperature. For the incommensurate CDW we therefore calculate: The pumped incommensurate CDW signal minus the unpumped incommensurate CDW signal, divided by the unpumped nearly commensurate CDW signal.

Thus, if the incommensurate CDW signal grows up to 50 %, it does not mean, that the signal has reached half its maximal strength. It only states that it is half as strong as the nearly commensurate signal is at room temperature. In order to compare the CDW amplitudes, we need to take into account that the signal strength is proportional to the square of the CDW amplitude. Therefore, a signal drop to 50 % would correspond to the atomic displacement (which defines the CDW amplitude) being reduced to 70 %.

The fact that the two CDW signals are still relatively close together has to be taken into account as well. The incommensurate CDW spots are slightly overlapping the slope of the stronger nearly commensurate CDW peaks. This can distort the results of the incommensurate CDW behaviour. To compensate for that, the background mask needs to be adjusted to an equivalent position relative to the nearly commensurate CDW spots like shown in figure 5.5c. Therefore it makes sense to do the analysis twice with different background masks: once for the nearly commensurate CDW and the Bragg peaks and once for the incommensurate CDW. The effect of the incommensurate CDW peaks on the nearly commensurate CDW signal is neglected due to the intensity difference of the two.

The whole diffraction pattern with the four different masks is shown in figure 5.5d.

# 6. Results

In this chapter, the results of our measurements on the commensurate CDW in $4H_b$-$TaSe_2$ as well as the transition from the nearly commensurate to the incommensurate CDW in $1T$-$TaS_2$ are introduced and discussed. All measurements were performed in a team effort. However, each student focused on one particular sample and ensured a proper analysis of the data and a suitable interpretation of the results. The results obtained from measurements done on $4H_b$-$TaSe_2$ are therefore discussed in detail in the PhD thesis of Nicolas Erasmus [45] and [50]. Here only a short summary will be given on which basis the new results on $TaS_2$ will be discussed extensively later in this chapter.

Note, that with electron diffraction we only observe the structural part (PLD) and not the actual (purely electronic) CDW itself. Therefore, when speaking of a 'CDW', we usually refer to the combined CDW/PLD phenomenon. For equilibrium systems this terminology is mostly irrelevant since both parts – structural and electronic – always come together. In time resolved experiments far from equilibrium however, one has to be careful not to confuse the two.

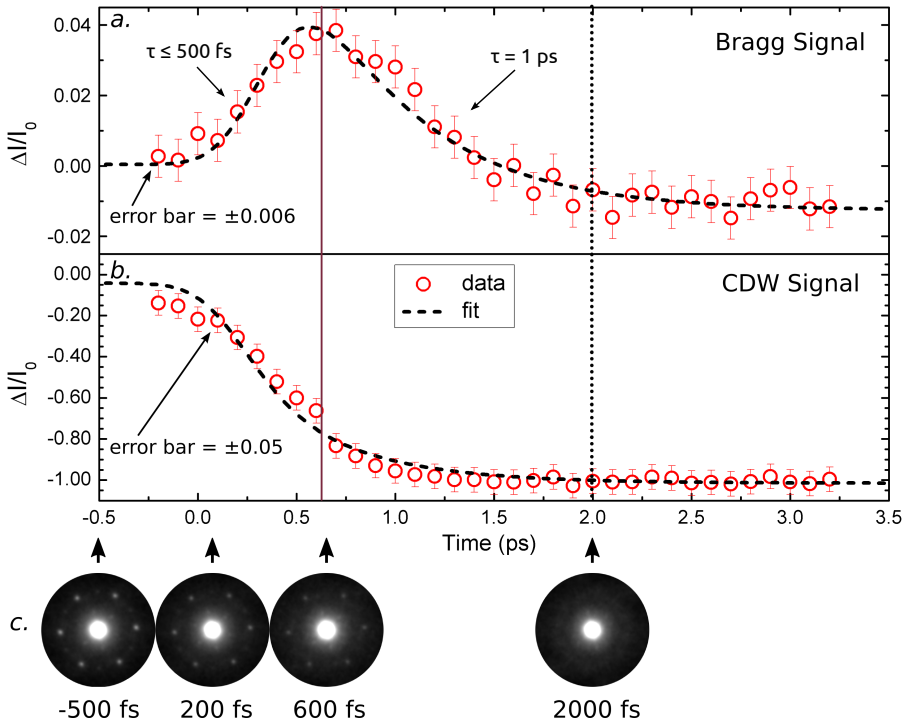


Figure 6.1: Following photo excitation, the atoms move towards their unperturbed lattice position, which results in a higher Bragg peak intensity and a decrease in CDW peak intensity. When the lattice heats up, its vibrations lead to a further reduction of both, the Bragg as well as the CDW signal.

## 6.1 $4H_b$-$TaSe_2$

A typical diffraction pattern obtained at room temperature clearly shows the $\sqrt{13} \times \sqrt{13}$ superstructure of the CDW (see figure 5.4a). When pumping the sample with a short laser pulse, energy from the pump photons is transferred instantaneously to the electrons in the sample. Since the electrons are now 'hot', the CDW is destroyed immediately. The lattice ions however are much heavier and slower compared to the electrons and react on a timescale of hundreds of femtoseconds. The star clusters, consisting of 13 atoms each, start to dissipate and the atoms relax back towards their unperturbed lattice positions. This PLD weakening is seen in the measurement as a drop in the CDW peak intensity as well as a rise in the Bragg intensity (see figure 6.1). This happens within our temporal resolution of 500 fs.

The electrons continue to transfer energy to the lattice via the Debye-Waller effect. The ions start to jiggle around their average position which again reduces the symmetry of the lattice and thus the intensity of the Bragg peaks. The PLD continues to weaken as can be seen in the further decrease of the CDW signal intensity. Due to the strong electron–phonon coupling, a time constant of only $\approx$ 1 ps was found for this process.

These developments were already described by Eichberger *et al.* [18] for a very similar system. Here the photo excited perturbation of the nearly commensurate CDW in $1T$-$TaS_2$ resulted in the same qualitative behaviour within the first few picoseconds.

For pump fluences above 2.5 mJ/cm$^2$, our sample is believed to completely change into the higher energetic phase which forms an incommensurate CDW. This can be seen by the complete suppression of the CDW peaks. However, the incommensurate CDW does not produce a visible diffraction pattern in our setup since its amplitude is too small. The fluence needed to reach the phase transition heats the sample up to the equilibrium phase transition temperature of 410 K. This means that in the end also in the photo excited transient case, thermal heating is necessary to initiate the phase transition. The system then recovers back to its original room temperature state on a nanosecond timescale (see figure 6.2). On the other hand, when the PLD was only perturbed with a fluence of less than 2.5 mJ/cm$^2$, the recovery is faster with a time constant of 150 ps.

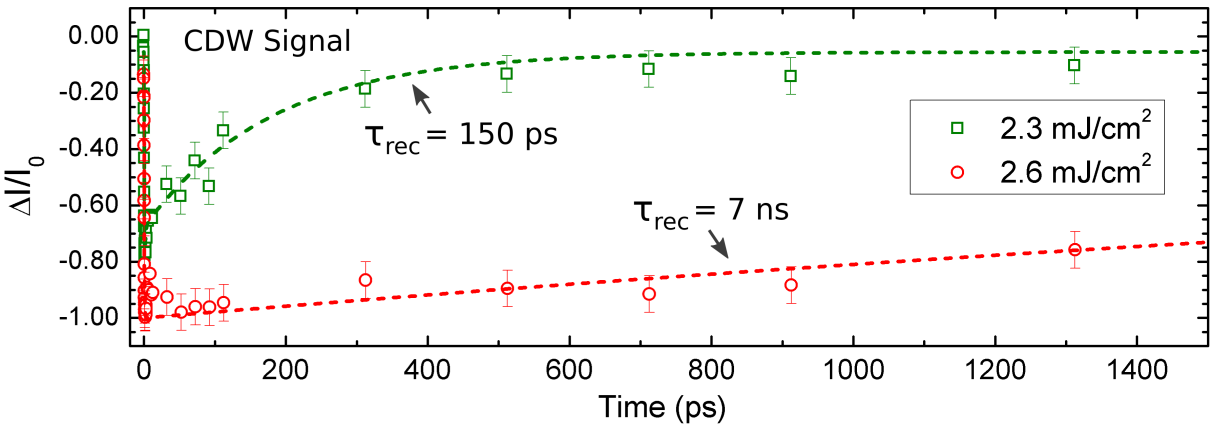


Figure 6.2: The recovery time depends on whether the CDW was completely suppressed or only perturbed.

Similar observations have been made on $TiSe_2$ using time resolved x-ray diffraction [19]. Here also, the recovery time was found to be significantly longer when the CDW was completely suppressed and long range structural correlations had to be reestablished through domain regrowth. In contrast, when only disturbing the CDW, the order itself remains and only the CDW amplitude has to be recovered which leads to a much shorter time constant.

## 6.2 1*T*-$TaS_2$

In order to study an optically induced CDW phase transition, 1*T*-$TaS_2$ is a more suitable sample. Here, the energetically higher (incommensurate) CDW phase produces a visible diffraction pattern in our setup, which in addition is spatially separated from the pattern of the energetically lower (nearly commensurate) phase. This allows us to simultaneously study the temporal behaviour of both, the suppressed as well as the excited CDW.

Like shown in section 2.2, 1*T*-$TaS_2$ shows a nearly commensurate CDW at room temperature, which we can see in the diffraction pattern as weaker spots in between the bright Bragg spots (left in figure 6.3). By drawing a line through two neighbouring CDW peaks and extending it towards the next Bragg peak, it becomes quite clear that this is not a perfectly commensurate phase: The line does not go exactly through the centre of the Bragg peak like one would expect for the commensurate structure.

When pumping the sample and looking at the diffraction pattern well after time zero, it changes to the one shown in the right hand part of figure 6.3. Three major differences can be noticed between the two: the CDW pattern weakens, the higher orders disappear completely and the CDW pattern rotates by an angle of 12° and is now aligned with the much brighter pattern of the lattice. Furthermore, the distance between a Bragg spot and the corresponding CDW spots is slightly (about 1 %) smaller for the incommensurate CDW. This small change cannot be seen by eye, but becomes apparent when analysing the pictures with the software described in section 5.4.

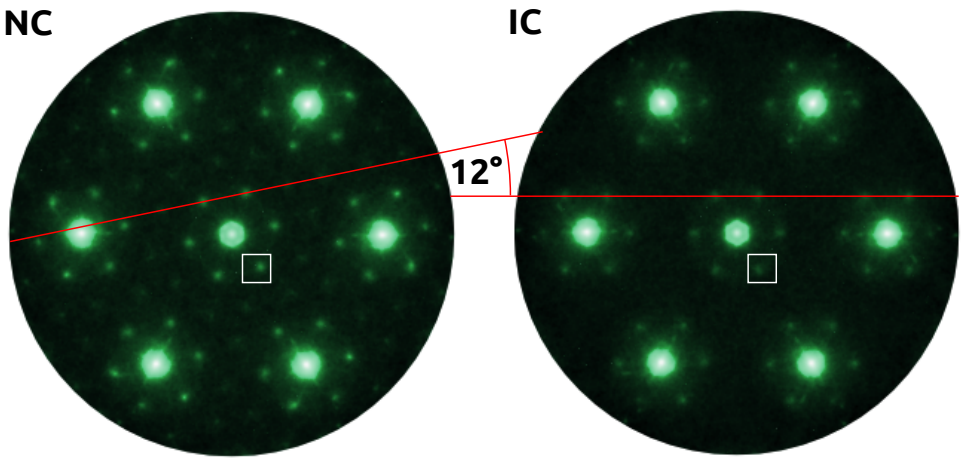


Figure 6.3: Diffraction pattern of 1*T*-$TaS_2$ before (left) and 10 ps after (right) photo excitation. A rotation of 12° can be determined between the two CDW derived diffraction patterns. Each picture was obtained by rotating a diffraction image five times by 60° and averaging over the six resulting images. This enhances the image quality and the differences between the two patterns become more evident.

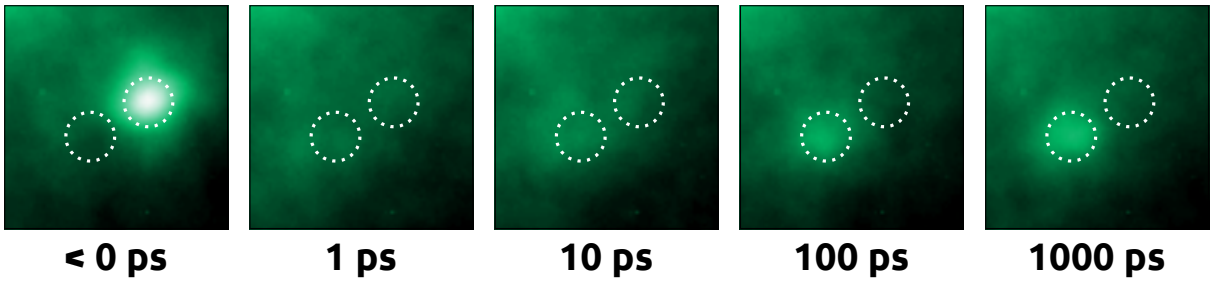


Figure 6.4: Development of the CDW peaks in the diffraction pattern from the nearly commensurate to the incommensurate phase. The positions of both CDW signatures are indicated in each panel; the same scaling factor was used for all panels. The fluence was 2.1 mJ/cm$^2$.

These observations coincide with the specifications known about the incommensurate CDW pattern (see section 2.2, since the diffraction pattern is an image of the reciprocal lattice, we can directly compare it with the sketches in figure 2.5). As a check, we heated our sample to an equilibrium temperature above the phase transition temperature of 353 K. The diffraction pattern we found looks exactly like the one we get when pumping the sample at room temperature with a laser pulse. This confirms our interpretation of initiating the phase transition to the incommensurate phase through photo excitation.

We will now look at the development of the sample structure from the one to the other state. Figure 6.4 shows a small region of the diffraction pattern (indicated in figure 6.3 as white squares) for different pump–probe delay times. A high pump fluence of 2.1 mJ/cm$^2$ was used for this measurement. The positions of the nearly commensurate (right hand circle) and the incommensurate (left hand circle) CDW spots are marked in each panel. Note, that the CDW spots are not moving but rather disappearing at the one and appearing at the other position. It is clearly visible, that at least two processes with different time constants are involved: the nearly commensurate CDW disappears within the first picosecond, while the incommensurate CDW needs a considerably longer time to develop. The results of measurements on both timescales will now be discussed.

**The First Picoseconds** The faster dynamics in the immediate vicinity of time zero were measured for a relatively high pump fluence of 1.9 mJ/cm$^2$, the results are shown in figure 6.5. Plotted are the relative intensity changes of both CDW signals as well as the lattice Bragg peaks, like it was explained in section 5.4.

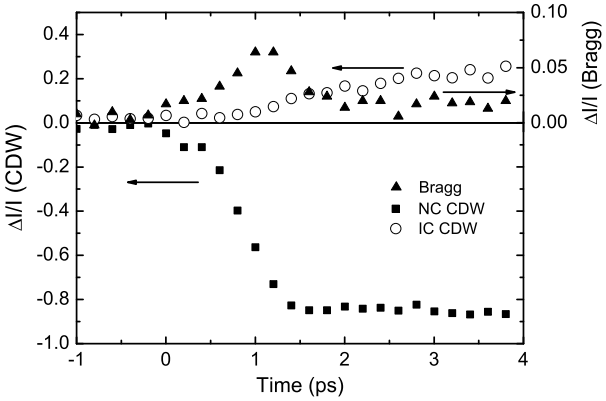


Figure 6.5: Behaviour of the CDW and Bragg signals up to 4 ps after photo excitation. A pump fluence of 1.9 mJ/cm$^2$ was used for this measurement.

The nearly commensurate CDW signal which we observe at room temperature, decreases within our temporal resolution of 700 fs. This indicates a strong electron–phonon coupling in the sample. We saw the same behaviour already in the $TaSe_2$ measurements described above and it has also been observed previously on 1$T$-$TaS_2$ samples which were cooled to an equilibrium temperature of 200 K [18].

The intensity of the Bragg signal increases when the nearly commensurate PLD gets attenuated since the atoms are now released from their CDW positions and move towards their unperturbed lattice positions. This again happens within our temporal resolution. However, the Debye-Waller effect then leads to a reduction of the Bragg intensity. This behaviour too was already explained in previous experiments and in the following we will concentrate on the development of the two CDW phases only.

The incommensurate phase appears, maybe with a slight retardation, slowly increases and continues to grow after the four picoseconds shown in this graph. Measurements on longer timescales are therefore necessary in order to analyse the behaviour of this CDW.

**Nanosecond Behaviour** The development of both CDWs was measured for different pump fluences on a time scale up to a nanosecond after excitation (see figure 6.6). All the measured curves stabilise after a few hundred picoseconds and we conclude that a quasi equilibrium state is reached at this point. Several features can be observed in the graphs:

- *Time constants:* There are at least two processes involved in the development of both, the nearly commensurate as well as the incommensurate CDW. The first changes happen on a picosecond time scale, while the time it takes the sample to stabilise into the new state is in the order of 100 ps. Furthermore, the long time constants clearly depend on the pump fluence.

- *Signal strength:* The intensity of the CDW diffraction peaks in the new state shows a threshold behaviour: When pumping with 1 mJ/cm$^2$ or more, the incommensurate CDW always stabilises at a value of 50 %, while the nearly commensurate CDW disintegrates completely. When pumping with less (0.8 mJ/cm$^2$), the incommensurate CDW signal stabilises at a lower intensity and in this case, the nearly commensurate CDW is still present in the sample as well.

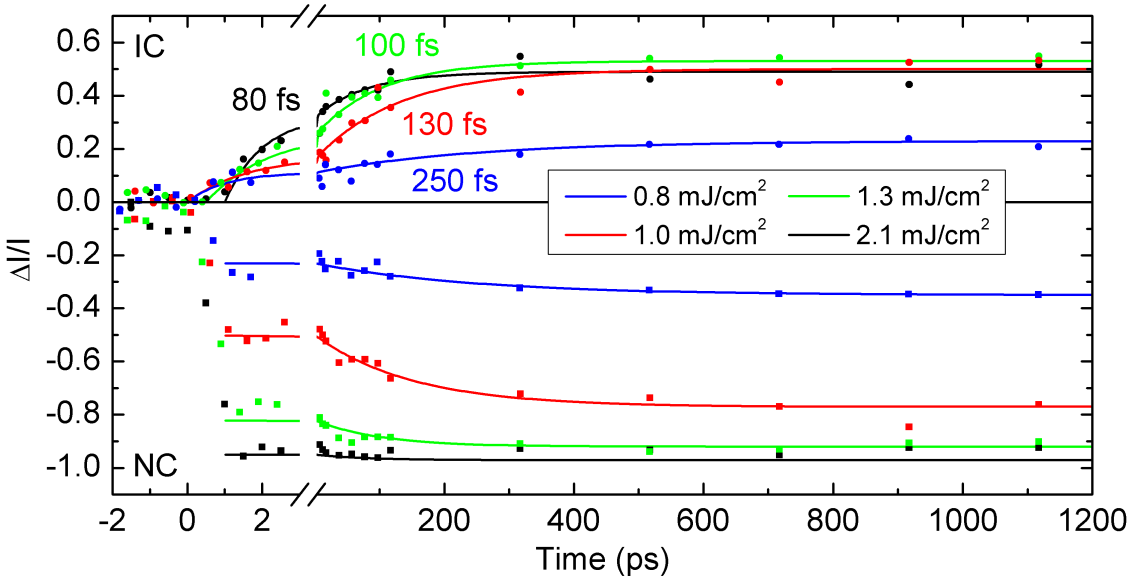


Figure 6.6: Long-term behaviour of the CDW signals for different pump fluences. Time constants for the recovery process are given for each measurement for the incommensurate phase. The fits are explained in the text.

- *Delay:* We also noticed a delay of up to 1 ps for the onset of the growth of the incommensurate CDW when using high pump fluences (see figure 6.10 below).

Since the CDW state in equilibrium is given by the sample temperature, it seems likely that this might also be the case in our nonequilibrium experiments. Therefore we first consider the expected temperature behaviour in the sample initiated by the pump beam, before discussing the above mentioned points in detail.

**Temperature Behaviour** In equilibrium, one can describe the sample as consisting of a lattice and an electron gas, both having the same defined temperature $T_0$ throughout the entire sample. When hitting the sample with a laser pulse, energy is deposited into this system which eventually leads to a state similar to the initial one but with a higher temperature $T_1$. After an even longer time, the sample will be cooled to $T_0$ again. However, in the following we will only look at the processes leading to the quasi equilibrium state at $T_1$. We will not take the cooling processes into account since we assume them to happen on a significantly longer time scale which we do not observe in our measurements.

From the total energy a single laser pulse contains, only a part is absorbed in the sample and thus contributes to the temperature rise in it. The rest is either reflected or transmitted. The transmittance of our pump light (775 nm, 1.6 eV) through the sample was measured to be 16 %. The reflectance could not be measured, since the very thin sample was not flat enough to allow for a good reflection. However, with the help of wavelength dependent optical parameters for 1$T$-$TaS_2$ given in literature [51], we can calculate the sample to be 34 nm thick and absorb 48 % of the incoming pump light [52].

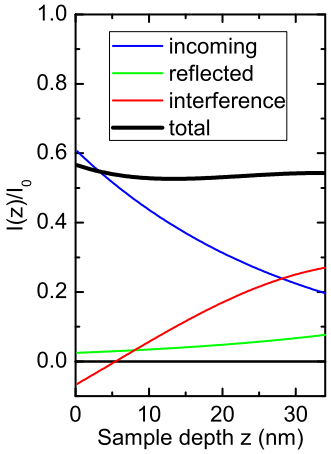


Figure 6.7: A forward moving wave, a reflected wave and the interference between the two result in a nearly homogeneous excitation profile. $I_0$ is the intensity of the incoming beam.

Since our sample thickness is almost equal to the penetration depth of the pump light (30 nm), one might suspect an inhomogeneous excitation density: The front part of the sample could be stronger pumped than the back part. However, this is not trivial and has to be calculated. In order to do so, the electric fields of both, the forward moving wave ($E_1$) as well as the wave reflected from the back surface of the sample ($E_2$) have to be added. The total intensity ($I$) of the light can then be calculated by taking the absolute square of this sum:

$$\begin{aligned} I(z) &= |E_1(z,t) + E_2(z,t)|^2 \\ &= |E_1(z,t)|^2 + |E_2(z,t)|^2 + 2\,\mathrm{Re}\{E_1(z,t)E_2^*(z,t)\}, \end{aligned} \tag{6.1}$$

where $t$ is the time and $z$ the distance from the front surface of the sample. The asterisk indicates the complex conjugate. The absorption can be included as the imaginary part of a complex wave number:

$$\tilde{k} = k + i\frac{\alpha}{2} \tag{6.2}$$

with $\alpha = 1/30\,\text{nm}$ being the absorption coefficient of $1T$-$TaS_2$. The first two terms in equation 6.1 represent the intensities of the forward moving and the reflected beams respectively, while the last term is the result of the interference between the two. In figure 6.7 these three parts and the resulting sum are plotted. One can see that the interference term has a large influence and actually leads to a nearly homogeneous excitation profile.

Two questions may now be asked, the answers of which will be important for the interpretation of our experimental results: What will the temperature $T_1$ be in the quasi equilibrium state and how long does it take to reach this state? These questions will now be discussed.

The temperature increase in the pumped sample area can be calculated by:

$$\Delta T = A\frac{F}{c_{\text{vol}} \cdot d} \tag{6.3}$$

where $A$ is the absorption, $F$ is the pump fluence, $c_{\text{vol}}$ is the volumetric heat capacity given in units of $\frac{\text{J}}{\text{cm}^3\,\text{K}}$ and $d$ is the sample thickness. The heat capacity of $1T$-$TaS_2$ is almost constant above room temperature and given in [53] as molar heat capacity $c_{\text{mol}} = 19\,\frac{\text{cal}}{\text{mol K}}$ ($1\,\text{cal} = 4.2\,\text{J}$). This can be converted to the volumetric heat capacity by dividing by the molar volume. In the end we get a value of $c_{\text{vol}} = 2.25\,\frac{\text{J}}{\text{cm}^3\,\text{K}}$ which leads to the relation

$$\Delta T[\text{K}] = 63 \cdot F[\text{mJ/cm}^2]. \tag{6.4}$$

When the sample is heated above the first phase transition temperature of 353 K, a certain amount of energy is used to actually overcome the transition and does not contribute to a temperature rise (this is a first order phase transition). In [53] this transition enthalpy is given as 122 cal/mol which would correspond to a fluence of $0.1\,\text{mJ/cm}^2$ or the energy needed for a temperature rise of 6.4 K. Therefore, when pumping strong enough to overcome the phase transition we should rather use the more accurate relation:

$$\Delta T[\text{K}] = 63 \cdot (F[\text{mJ/cm}^2] - 0.1). \tag{6.5}$$

Equation 6.4 (or 6.5) enables us to calculate the sample temperature $T_1 = T_0 + \Delta T$ in the quasi equilibrium state when the added energy is evenly distributed within the sample.

An equilibrium temperature of $T_0 = 33°\text{C}$ (306 K) was measured with a Pt100 element on the sample mount during the experiments. The phase transition would therefore require a temperature increase of 47 K. This can be reached by pumping with a fluence of $0.75\,\text{mJ/cm}^2$ while a minimum fluence of $0.85\,\text{mJ/cm}^2$ would be necessary in order to overcome the phase transition completely. The equilibrium temperatures we can reach with the pump fluences used in the measurements are shown in table 6.1.

| $F$ (mJ/cm$^2$) | $T_1$ (K) | $\tau$ (ps) |
|---|---|---|
| 0.8 | 353 | 250 |
| 1.0 | 363 | 130 |
| 1.3 | 383 | 100 |
| 2.1 | 430 | 80 |

Table 6.1: For each fluence the final sample temperatures $T_1$ and the fitted time constants $\tau$ for the long term behaviour of the incommensurate CDW are given.

At very early times just after photo excitation, the absorbed energy has not yet been converted into heat and therefore a sample temperature is not yet defined. We now look at the energy conversion processes in the sample which lead from the highly nonequilibrium to the thermalised quasi equilibrium state.

The energy of a laser beam hitting the sample is transferred to the electrons, exciting some of them into high energetic states. This gives rise to a nonthermal part of the electron distribution, additional to the thermal (still cold) part. Now, several processes can occur simultaneously [54]:

- Electron–electron scattering results in thermalisation of the electron gas. This means that the temperature of the thermal electrons will rise while the nonthermal electrons will relax into thermal states as well. The temperature of the electron gas is then much higher than the lattice temperature. This happens within $\approx 10\,\mathrm{fs}$ [20].

- Through electron–phonon scattering, energy will be transferred from the electrons (thermal and nonthermal) to the lattice. This results in an increase of the lattice temperature and a simultaneous decrease of the electron temperature until both temperatures are equal. A (local) thermal equilibrium is then reached. For 1$T$-$TaS_2$ a time constant of 300 fs was given by Eichberger *et al.* [18] for this process.

- Energy can also be transported by the (ballistic and diffusive) movement of both electrons and phonons through the sample. This however only plays a role if the initial excitation profile is inhomogeneous and can therefore be neglected in our case of homogeneous pumping.

Since both equilibration processes – electron thermalisation and electron–lattice equilibration – happen on a subpicosecond time scale and no transport mechanisms need to be taken into account, we conclude that a thermal equilibrium throughout the entire sample is reached within the first picosecond following photo excitation.

**Time Constants** The measurements of the incommensurate CDW could be fitted well with a sum of two exponential functions. The first rise has a time constant of about 1 ps for all fluences measured. The second process is much slower with time constants between 80 ps for the highest fluence and 250 ps for the lowest fluence (see figure 6.6 and table 6.1).

For the nearly commensurate state, the intensity rapidly decays within several hundred femtoseconds. If the CDW is not destroyed completely within this first decay, a small increase in CDW peak intensity follows. This is in accordance with the observations made by Eichberger *et al.* [18]. Since the complete curve shows at least three different processes (steep decay, small increase, long term decrease), a function describing the overall behaviour has many variables and an accurate fit would require a much higher density of measuring points. We will therefore concentrate on the long term behaviour only and refer to [18] for details on the fast picosecond behaviour. The long time constants were found to be in the same order than the ones obtained for the incommensurate CDW and also show the same fluence dependence. Within our measurement accuracy the time constants of the long term behaviour could very well be the same for both CDWs. In figure 6.6, only a single exponential function (shifted along

the $\Delta I/I$ axis) was fitted to each measurement of the nearly commensurate phase using the time constants $\tau$ we obtained for the corresponding incommensurate fits.

Like explained earlier, the energy transfer from the electrons to the lattice happens within one picosecond. Therefore, the initial fast development of the CDW intensities is not a big surprise. However, the long (fluence dependent) time constants must have a different origin.

During the first picosecond, the nearly commensurate CDW is obviously destroyed over a large part of the sample. However, unless we pump very hard, some regions initially stay in the nearly commensurate phase, even though the sample temperature is already above the phase transition temperature. In these regions, presumably some kind of potential barrier has to be overcome in order to change the phase.

Such a barrier might be produced by defects in the crystal structure which pin the CDW and thus make it more difficult to change its phase. Since defects are located randomly throughout the sample, some regions might be pinned stronger than others and therefore the potential barrier varies over the sample. For some regions the provided thermal energy might not be sufficient to immediately overcome the pinning forces. These regions remain in the nearly commensurate state for a while.

Another possible explanation of the energy barrier lies within the domain structure of the nearly commensurate phase: The structural modulation from the perfectly hexagonal lattice is less in the domain wall regions compared to the commensurately modulated domains. Therefore it seems plausible that the transition to the incommensurate phase involves a higher energy barrier within the domains and a lower one (or none at all) in the domain walls.

The signal of the incommensurate CDW reaches only part of its final intensity within the first picosecond. This is also the case if the nearly commensurate CDW has been destroyed completely right after pumping ($2.1\,\mathrm{mJ/cm^2}$). This indicates, that a certain part of the sample is neither in the nearly commensurate nor in the incommensurate phase and only with time the entire sample is converted to the incommensurate phase.

A possible scenario taking place in our sample is the following: The incommensurate CDW will start forming locally – preferably in the domain wall regions – with its phase adapted to defects. This nucleation results in many small domains being established within a few picoseconds, which are not yet in phase with each other. Domain boundaries without any particular superstructure will form between those domains. These parts will not contribute to any CDW peak intensity in the diffraction pattern. By overcoming the energy barrier, domains can align their phases to each other while domain boundaries and nearly commensurate domains can be converted to the incommensurate phase as well. This phase of domain growth happens on a longer time scale [19]. This idea is supported by the fact, that the developments of both, the nearly commensurate as well as the incommensurate phase, happen on a very similar – maybe even identical – time scale, which is to expect since the same process lies behind the development of both CDWs.

Su *et al.* [55] showed that in equilibrium, weak collective pinning effects play indeed a significant role in the incommensurate phase of $1T$-$TaS_2$: Domains, much larger than the average separation distance between defects, are pinned as a whole by many defects. After introducing a temperature jump, more barriers can be overcome and the system relaxes slowly by adapting domain boundaries and sizes to the new potential.

This relaxation process was found to follow an Arrhenius behaviour:

$$\tau(T) = t_a \cdot \exp \frac{E_B}{kT}. \tag{6.6}$$

Here, $k$ is the Boltzmann constant, $E_B$ the energy barrier which has to be overcome and $t_a$ the average time between attempts to overcome this energy barrier.

In figure 6.8 our measured time constants and their corresponding temperatures $T_1$ are shown in an Arrhenius plot. For the lowest pump fluence, the sample was pumped up to the phase transition temperature but the energy was not sufficient to overcome the phase transition in the entire sample. Therefore, other dynamics might play a role in this case and consequently this data point was not included in an Arrhenius fit. The best fit through the other three points is shown in the graph. We find an energy barrier of about 100 meV which is in the same order of magnitude than the 400 meV found by Su *et al.* [55].

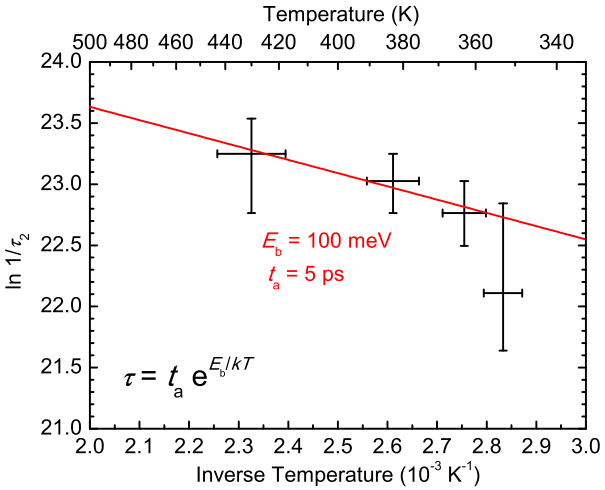


Figure 6.8: The measured time constants and the corresponding temperatures in an Arrhenius plot. The best fit through the three strong pumped measurements is shown as well. The weakly pumped measurement was not included in the fit (see text).

Small CDW domains – which implies a small correlation length of the superstructure – result in broad diffraction peaks and therefore domain growth is usually observed as a decrease in peak width [19, 56]. Unfortunately, we are restricted by the transverse coherence length of our electron beam which was measured to be 7–10 nm. Only domain sizes much smaller than this would lead to a measurable peak broadening in our setup. Since a domain consisting of only $5 \times 5$ CDW periods already has a diameter of 6 nm, it is not surprising that we do not resolve any changes in CDW peak width in our measurements.

**Signal Strength** Provided that the pump fluence is high enough (1 mJ/cm$^2$ or more), the incommensurate CDW always stabilises at a value of 50 % while the nearly commensurate CDW disintegrates completely. In the literature, the amplitude of the incommensurate CDW (in equilibrium) is given to be 70 % of the nearly commensurate one [15, 16]. Since the scattering intensity is proportional to the square of the CDW amplitude, this corresponds to an intensity change of 50 %, which is in agreement with our observations. We therefore conclude, that the entire sample is in the incommensurate phase after one nanosecond. The intensity difference between the two CDW phases is explained by the different amplitudes alone.

Only when pumping with a low fluence of 0.8 mJ/cm$^2$, the incommensurate CDW signal stabilises at a lower intensity. In this case, the nearly commensurate CDW is still present in the sample as well, after one nanosecond. Since both CDWs cannot exist at the same time in the same region of the sample, they have to be spatially separated. A fluence of 0.8 mJ/cm$^2$ is sufficient to reach the phase transition temperature but not enough to actually overcome the phase transition completely. Consequently, after one nanosecond some parts of the sample are still in the nearly commensurate phase, while other parts were converted to the incommensurate CDW.

In order to determine the fluence dependence more accurately, we have measured the CDW signal intensities at a fixed time of 2.5 ps after photo excitation (figure 6.9). This is after the initial fast (ps) changes occurred, but before the long term (100 ps) stabilisation. Therefore we can safely assume the sample to be in a thermal equilibrium at this stage while no significant domain growth has taken place yet. For comparison, the fluence dependent intensities after one nanosecond are included in the graph as well (blue dots). These are taken from figure 6.6. The top axis shows the final sample temperature calculated with equations 6.4 and 6.5, the phase transition region is marked by a grey box.

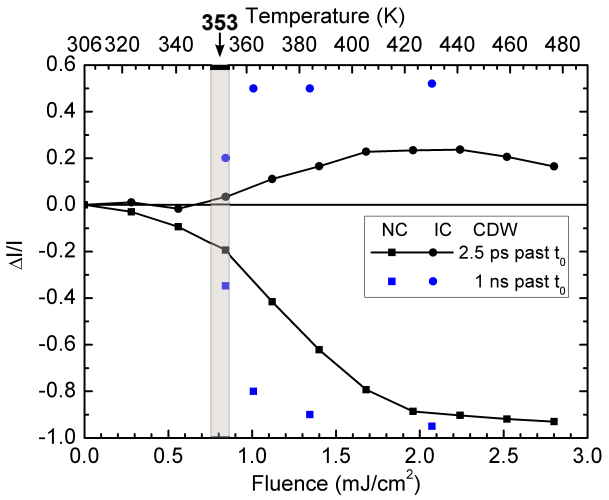


Figure 6.9: Fluence dependence 2.5 ps and 1 ns past time zero. The top axis shows the sample temperature we reach with the respective fluence shown in the bottom axis. The phase transition at 353 K is marked with a grey box.

Only weak pumping is necessary in order to perturb the nearly commensurate CDW and the perturbation gets larger with increasing fluences. When pumping with more than 2 mJ/cm$^2$, the CDW is completely destroyed already in the first 2.5 ps. The incommensurate CDW increases over a certain fluence range (0.8–1.5 mJ/cm$^2$) and then reaches a plateau. This phase always takes more than a few picoseconds to fully develop as can be seen when comparing with the one nanosecond measurements (blue dots).

Like calculated earlier (page 48), the phase transition temperature is reached for fluences of more than 0.75 mJ/cm$^2$ and the entire sample is pumped into the incommensurate temperature range with fluences higher than 0.85 mJ/cm$^2$. However, we again see that some regions initially remain in the nearly commensurate phase (except when pumping with more than about 2 mJ/cm$^2$), even though the temperature is clearly high enough to initiate the phase transition in the entire sample. These regions are only converted to the new state during the phase of domain growth.

The more of the sample remains nearly commensurate in the beginning, the less gets immediately transformed into the incommensurate phase. Therefore, the plateau in the incommensurate curve (at 2.5 ps) is only reached for fluences which immediately suppress the nearly commensurate CDW in the entire sample.

The decrease in the incommensurate curve for very high fluences cannot be explained by the phase transition into a state without any CDW. In equilibrium, such a phase exists above a temperature of 543 K and a fluence of 3.9 mJ/cm$^2$ (see equation 6.5) would be needed in order to reach this. Still, for high fluences almost the entire sample has no CDW order after 2.5 ps. This might be connected with the delay which will shortly be discussed in the following paragraph.

**Delay** We also noticed a delay in the order of 1 ps for the onset of the growth of the incommensurate CDW when using high pump fluences (see figure 6.10). Since the nearly commensurate CDW already decreases significantly within this time, the sample seems to be completely disordered first and the new phase then develops out of

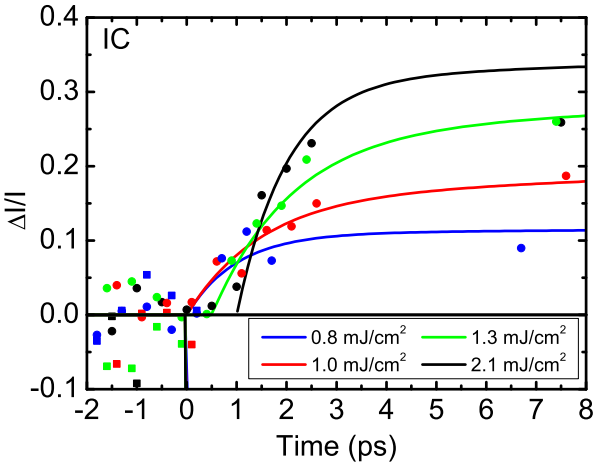


Figure 6.10: Enlargement of the development of the incommensurate CDW. Same data as in figure 6.6.

this disordered state. The time of complete disordering grows with increasing fluence which might be the explanation for the observed decrease of the early incommensurate CDW intensity for high fluences (see figure 6.9). However, our measurement accuracy does not allow for a detailed analysis of this finding. More accurate measurements need to be done to confirm and investigate this behaviour.

# 7. Summary

I have investigated the structural dynamics of CDW phases in strongly correlated electron systems, namely $4H_b$-$TaSe_2$ and $1T$-$TaS_2$, using femtosecond electron diffraction.

**The FED Setup** The FED setup which is currently in use at the Stellenbosch University can produce electron pulses shorter than 500 fs (at sample position), containing about 1000 electrons with an energy of 30 keV. The system was introduced in this work and its elements described in detail: Short electron pulses are generated by laser pulses producing photo electrons on a gold film. These are accelerated by a static electric field and then focused by a static magnetic field. The detection system consists of MCP, phosphor screen and a 16 bit CCD camera. The sample is situated only about 6 cm behind the photo cathode in order to limit pulse broadening due to space charge effects. The electron current can be measured by a picoammeter connected to a Faraday cup and a home built streak camera is used to measure the electron pulse length at sample position. Alignment techniques to achieve spatial and temporal overlap of pump and probe beams on the sample piece were described as well. Beam correction systems are situated in each beam path and are essential to keep the beam positions on the sample stable over many hours. The system has a total time resolution of about 500 fs, a transverse coherence length of 10 nm and is able to detect intensity changes in a diffraction pattern of about 1 %.

The crystalline $TaSe_2$ and $TaS_2$ samples were prepared with an ultramicrotome. Slices thinner than 100 nm were cut and floated onto TEM meshes. Mounting good sample pieces onto small (100 μm) apertures provides for an excellent quality diffraction pattern.

Measurements can take many hours during which many image pairs are collected, each consisting of a diffraction image of the pumped and one of the unpumped sample. We perform and average over many identical scans in order to increase the signal-to-noise ratio of the resulting data. The collected images are analysed to get information about the changes in the diffraction pattern relative to its unpumped state. In the experiments on the two transition metal dichalcogenides, we observe the intensity changes of the different Bragg and CDW signals depending on the delay time between pump and probe.

**Transition Metal Dichalcogenides** Measurements on the two transition metal dichalcogenides $4H_b$-$TaSe_2$ and $1T$-$TaS_2$ showed that the optically induced phase transition requires thermal heating above the transition temperature. Initial dynamics happen on a subpicosecond time scale: the PLD weakens and the lattice heats up. The recovery of $4H_b$-$TaSe_2$ to the original state was found to be 150 fs when the CDW was disturbed with a fluence below 2.5 $mJ/cm^2$. With higher fluences, the sample was trans-

formed completely into the higher energetic (incommensurate) phase. This means that the long range order of the superstructure has been lost and needs to be reestablished which leads to a significantly longer recovery time of about 7 ns.

In contrast to $4H_b$-$TaSe_2$, the higher energetic (incommensurate) state in $1T$-$TaS_2$ produced a clear diffraction pattern and therefore we were able to observe the dynamics of both, the suppressed and the excited CDW. Here, the most noticeable result was the observation of the relatively long time constants (100 ps) for the formation of the incommensurate CDW phase which seem to equal the destruction times for the nearly commensurate CDW. These times were also found to depend on the pump fluence used. A recovery to the original state was not observed within the first nanosecond following excitation.

From our data obtained on $1T$-$TaS_2$ we learnt that at early times (1 ps after pumping), some sample areas are neither in the nearly commensurate nor in the incommensurate phase and some areas might still be in the nearly commensurate phase even if the sample temperature is clearly above the transition temperature. Only after some time all regions are converted to the incommensurate phase. Due to a homogeneous excitation profile within the sample, thermal equilibration by heat diffusion could be excluded as an explanation for the long time constants.

A possible scenario was proposed: The CDW is pinned by defects in the crystal structure. This results in an energy barrier which has to be overcome in order to change the CDW. Due to photo excitation, the electronic part of the superstructure (CDW) gets destroyed and the structural part follows on a subpicosecond time scale (PLD weakening). The lattice heats up until a thermal equilibrium between electrons and lattice is established within a picosecond. The incommensurate phase starts evolving locally by forming small domains adapted to defects. Some stronger pinned regions might initially stay in the nearly commensurate phase while the domain walls (regions in between the domains) do not show any CDW. The domains then grow and 'melt' together in order to establish a long range order in the crystal. This process follows an Arrhenius behaviour and the energy barrier was estimated to be in the order of 100 meV. In the case of low pump fluence, the transition could not be completely overcome and thus, both phases are still present in the sample after the phase of domain growth.

**Outlook** Femtosecond electron diffraction is a powerful tool to study crystalline materials under nonequilibrium conditions. Structural changes following a sudden excitation can be temporally resolved and directly measured. This was shown on the example of two transition metal dichalcogenides whose CDWs were studied in the nonequilibrium. The information we gained with these experiments helped to better understand the CDW phenomena. However, many other materials – not only transition metal dichalcogenides – show features which would be interesting to study in a femtosecond electron diffraction experiment. Therefore it is to expect that in the future many FED experiments will contribute to the better understanding of various effects in condensed matter.

Since there are many possibilities to improve current FED setups, it is also to expect that better and better FED systems will emerge in the future. The time resolution will get better, the signals will be clearer and the results less noisy. Samples, which do not fulfil the current limitations will become accessible as well. Electron pulse compressors will allow for single shot experiments and with that, irreversible processes will be much easier to observe.

# A. Preparing and Running the Measurement

## A.1 Preparing for the Measurement

After a standard check of the laser beam alignment, the electron beam has to be aligned as well. Therefore everything inside the chamber should be moved out of the electron beam path. This includes the beam block just in front of the detector. The electron signal is now visible on the detector and can be focused by adjusting the current of the magnetic lens.

Note that either the UV intensity or the MCP voltage should always be decreased if the focused main electron beam is hitting the detector. The strong signal would otherwise damage the phosphor screen permanently.

If the electron beam is not perfectly aligned along the axis of the magnetic lens, it changes position on the detector when changing the lens current. This means that the electron beam is not moving on the symmetry axis of the magnetic lens. To correct this, the UV lens in front of the electron gun can be adjusted in both directions perpendicular to its optical axis ($x$ and $y$). This changes the spot on the cathode where the electron pulses are produced and thus also their path through the magnetic lens. When properly adjusted, the electron spot only changes its size when turning the lens current but does not move.

Misalignment of the electron beam usually does not matter so much for the quality of the diffraction signal but it makes it more difficult to find it in the first place.

To find and optimise the sample position for the best diffraction pattern, the magnetic lens is defocused such that the electron signal on the detector is fairly big. Now the sample can be moved into the beam and a shadow image becomes visible on the detector.

If the sample is already mounted on an aperture as described in chapter 4, it is easy to find and optimise the diffraction pattern. The aperture is very small and difficult to find with a small electron beam. But by turning up the UV intensity, the beam becomes very big at sample position and a shadow image of the aperture is easily found. The beam is then slowly focused and the sample position corrected to keep the signal visible on the detector. The centre position can be worked out by moving the aperture to the edges of the beam in both $x$ and $y$ directions where the signal just disappears and then taking the average of these positions. The diffraction pattern is now optimised.

If the sample is not mounted on an aperture, the whole mesh is visible in the shadow image. The sample pieces appear as darker areas and the shapes can be compared to a microscope image taken earlier from the sample. Thereby one should be aware that pieces of resin are clear under the microscope, but appear dark in the elec-

tron beam as well. The 'good' spot is moved into the middle of the electron beam and kept there while the magnetic lens is slowly focused. When the focus is reached, the diffraction pattern is visible and can be optimised by slightly moving the sample.

Once the optimal position of the sample is found, it can be saved in the control program of the stages.

If the electron beam (and the Bragg spots) appear to be too big even when focused with the magnetic lens, the $z$-position of the UV lens should be checked (see section 3.1). Other reasons could be a very high electron current or, when the pattern was observed with the camera, misalignment of the macro lens of the camera.

**Temporal Overlap** The beam paths of pump and probe are designed such, that both beams arrive at sample position at approximately the same time. Fine adjustment of the timing can be done by moving the translation stage placed in the pump beam path. First, we need to find the stage position for which the two pulses are temporally overlapped at the sample (time zero position). Later, we want to scan around this position in small steps to observe the structural changes triggered by the pump pulse.

Since the streak camera functions like a pump probe experiment (see section 3.1) it can be used to roughly find the time zero position. The streak plates are placed at sample position and the pump beam is used to trigger the optical switch. A voltage of 10 V applied on the streak plates is sufficient to considerably deflect the electron beam. When the switch is triggered, this deflection reduces quickly following a damped oscillation. This is clearly visible on the detector when moving the delay stage through the corresponding region. We are interested in the position, where the deflection of the electrons just starts to change.

The vague positioning of the 3 mm long streak camera at sample position, as well as a small time delay between activating the optical switch and actually discharging the capacitor, limit the accuracy of this method to a window of millimetre size. We can now use a different, more accurate method to find the time zero position more exactly.

An aperture is placed at sample position and the pump beam focused onto its inner edge. The pump beam should be as strong as possible without generating a plasma at the aperture. A plasma would quickly damage the aperture and additionally produces a strong background signal on the detector making it impossible to observe the electron signal. The pump beam now produces an electron cloud at the aperture. If the electron probe pulse passes the aperture after the pump pulse created the electron cloud, it will be disturbed by it. This is visible on the detector as a slight change of the position and possibly also by a deformation of the electron signal (see figure A.1). This is just a very small movement, but is clearly distinguishably from the statistical fluctuations of the signal. Time zero can be found by looking for the position where the signal just starts to change.

If a sample is available which shows a drastic change in the diffraction pattern when being pumped and has a long recovery time constant, it might be easier to use this signal instead to find time zero. The complete disappearance of some diffraction spots is a good example.

The delay stage position for temporal overlap stays the same as long as sample position and electron energy are not changed. Small shifts can be seen when changing filters or lenses in one of the beam paths.

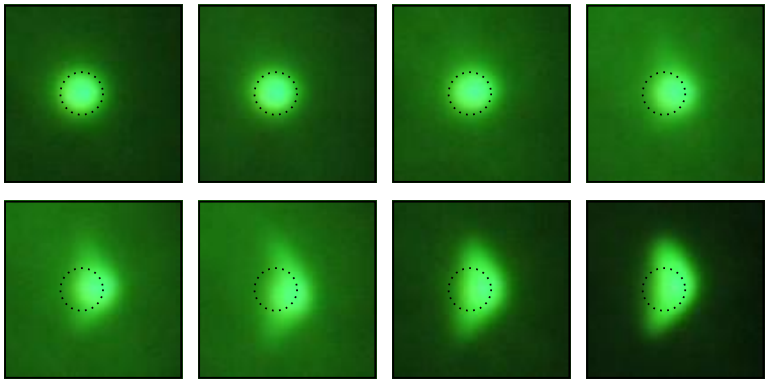

Figure A.1: Electron signal for different time delays between pump and probe. The step size between the images was 1.2 ps. In the third panel, the electrons start to get deviated by the charges produced by the pump beam. The time zero position therefore is between the second and the third panel.

**Spatial Overlap** To ensure that the pump and probe beams are spatially overlapped on the sample, a 100 µm aperture is mounted in the sample mount and thus in the same $z$-plane than the sample. By observing the shadow image on the detector the aperture is moved and optimised into the electron beam. The pump beam hits the aperture from the opposite side. A small piece of paper is placed on the magnetic lens so that the part of the pump beam going through the aperture can be seen there. By adjusting the beam path with a mirror outside the chamber the intensity of the observed spot can be optimised. Spacial overlap is now achieved.

Ideally, the sample is already situated on an aperture and the spatial overlap can be achieved directly on the sample. Otherwise, the sample can now be adjusted into the electron beam by observing the shadow image.

In the beginning of a measurement, the positions of pump and probe beams are saved and during the measurement their movements are observed and corrected for with the two beam correction systems in both beam paths like described in chapter 3. Therefore, spatial overlap is guaranteed during the whole measurement.

To ensure that the diffraction signal stays strong for several hours, we need to make sure that the UV beam hits a relatively fresh spot on the cathode. On a fresh spot we need to use less laser power to produce a certain amount of electrons and therefore the ageing of the cathode spot is (after an initial drop) still comparably slow. The UV intensity is then adjusted to optimise the signal strength.

Just before starting the experiment, an image of the diffraction pattern is taken as a last check whether everything is correct. The pattern should be as strong as possible without saturating the camera. The beam block must be positioned to block the strong electron signal in the centre of the pattern. The Bragg spots should be small and in focus.

## A.2 The Measurement Program

The front panel of the program which controls the measurement is shown in figure A.2.

A starting position on the delay stage as well as the ranges and step sizes for the wished scan can be defined after starting the program. Several ranges with different


Figure A.2: The front panel of the UED-scan program.

step sizes can be selected. The units can be alternated between millimetres (stage position / position change) and picoseconds (time delay between pump and probe), the current values will be converted accordingly. An exposure time and a number of scans can be chosen, but usually these values do not need to be changed. A one minute exposure time was the standard value for all our measurements so far. It makes sense to choose a high number of scans and abort the program when the signal gets too low or enough data has been collected.

When clicking on 'New ROI', a diffraction image will be taken with the exposure time defined as a probe beam correction parameter. Here, an exposure time of 5 s is typically enough but can be increased if necessary. One of the Bragg peaks, preferably the brightest one, can be selected by drawing a box around it. The position of the box is stored in a file and whenever the program checks the probe beam position, it takes an image with the given exposure time and calculates the centre of mass of the signal inside the chosen box.

Since a finite background signal could falsify the apparent beam position, all pixel values below a threshold value will be set to zero. This threshold should be set to a value just above the background level of the image. Note, that the images taken with the 16 bit camera can have negative values and therefore the threshold is usually somewhere around $-30000$. The centre of mass is then determined of the background corrected image.

This value is determined over and over again during the course of the measurement. It is compared to the stored values of the initial beam position and if the beam has moved more pixels than defined by the 'tolerance', the program corrects, checks the new position and if necessary corrects again. This goes on until the beam is back within the given limits.

The pump beam correction works accordingly. Threshold and tolerance can be adjusted on the front panel. No box need to be chosen since the whole camera image will be used in order to work out the beam position. The initial position and intensity of the beam on the camera can be checked and optimised with a different program (test

firewire cam.vi) before starting the measurement. The shutter in the pump beam path can be operated by clicking on the big green button which indicates its current status.

When pressing the 'scan' button, the program moves the stage to its starting position and makes sure the shutter in the pump beam path is open. The current positions of both beams are saved and used as reference throughout the measurement. Then both beam correction setups are calibrated: the piezo mirrors are moved a certain number of steps and the movement of the centre of mass of the signal on the camera is observed. A calibration value is saved for each direction ($+x$, $-x$, $+y$ and $-y$) in a file. The beams are then corrected to their original position. This is necessary since the step sizes of the piezo mirror mounts are not well defined and can be different in each direction.

The first two pictures of the diffraction pattern are taken and saved on the computer, one with the shutter open and one with the shutter closed. Then the stage moves one step to the next position, the pump and probe beams are checked and if necessary corrected and the next two pictures are being taken. This will be repeated until the end of the first scan. Then the stage again moves to the starting position, the pump and probe beam correction systems are calibrated, the beam positions corrected and the next scan is started while the pictures are being saved in a new folder for each new scan.

The current position of the delay stage as well as the number of the current scan are shown at all times in the program. The blue status bar on the right hand side of the front panel shows the progress of the current scan. Important data is saved in a log file (Log.txt) for each scan. For every picture this includes the exposure time (usually 60 seconds), the shutter status (open or closed), the stage position in millimetres and the current time. Also the centre of mass of the probe beam position is saved in a log file (CoMLog.txt), as well as the number of steps the piezo mirrors take to correct the two beams (Z:\UED-programs\Beam Walk Compensator\PiezoLog). This enables us to check the movement of the beams over time.

The program can be aborted by the user at any time by clicking on the red button in the menu bar (not included in figure A.2). The program also stops automatically, when the signal becomes too low: Whenever an image is taken to check the probe beam position, the maximum intensity of the beam is compared to the threshold value. If the intensity is less than 500 counts above the threshold value, the program stops. Therefore it is safe to run a measurement without being in the lab for a long time period (for example over night).

# Bibliography


[1] Kittel, C.: *Introduction to Solid State Physics*. Wiley, 2008.

[2] Rossnagel, K.: On the origin of charge-density waves in select layered transition-metal dichalcogenides. *Journal of Physics: Condensed Matter*, vol. 23, p. 213001, 2011.

[3] Singleton, J.: *Band Theory and Electronic Properties of Solids*. New York : Oxford University Press, 2001.

[4] Wilson, J.A., Di Salvo, F.J. and Mahajan, S.: Charge-density waves and superlattices in the metallic layered transitient metal dichalcogenides. *Advances in Physics*, vol. 24, pp. 117–201, 1975.

[5] Schuster, R.: *Electron Energy-Loss Spectroscopy on Underdoped Cuprates and Transition-Metal Dichalcogenides*. Ph.D. thesis, Technische Universität Dresden, 2010.

[6] Lüdecke, J., van Smaalen, S., Spijkerman, A., de Boer, J.L. and Wiegers, G.A.: Commensurately modulated structure of 4Hb–$TaSe_2$ determined by x-ray crystal-structure refinement. *Physical Review B*, vol. 59, no. 9, pp. 6063–6071, March 1999.

[7] Di Salvo, F.J., Moncton, D.E., Wilson, J.A. and Mahajan, S.: Coexistence of two charge-density waves of different symmetry in 4Hb $TaSe_2$. *Physical Review B*, vol. 14, p. 1543, 1976.

[8] Moret, R. and Tronc, E.: CDW induced atomic shifts in 4Hb–$TaSe_2$. *Physica*, vol. 99B, pp. 56–58, 1980.

[9] Spijkerman, A., de Boer, J.L., Meetsma, A., Wiegers, G.A. and van Smaalen, S.: X-ray crystal-structure refinement of the nearly commensurate phase of 1T–$TaS_2$ in (3+2)-dimensional superspace. *Physical Review B*, vol. 56, p. 13757, 1997.

[10] Thomson, R.E., Burk, B., Zettl, A. and Clarke, J.: Scanning tunneling microscopy of the charge-density-wave structure in 1T–$TaS_2$. *Physical Review B*, vol. 49, p. 16899, 1994.

[11] Hellmann, S., Rohwer, T., Kalläne, M., Hanff, K., Sohrt, C., Stange, A., Carr, A., Murnane, M.M., Kapteyn, H.C., Kipp, L., Bauer, M. and Rossnagel, K.: Time-domain classification of charge-density-wave insulators. *Nature Communications*, vol. 3, p. 1069, 2012.

[12] Sipos, B., Kusmartseva, A.F., Akrap, A., Berger, H., Forró, L. and Tutiš, E.: From mott state to superconductivity in 1T-$TaS_2$. *Nature Materials*, vol. 7, p. 960, 2008.

[13] Fazekas, P. and Tosatti, E.: Charge carrier localization in pure and doped 1T-$TaS_2$. *Physica B*, vol. 99, pp. 183–187, 1980.

[14] Dardel, B., Grioni, M., Malterre, D., Weibel, P., Baer, Y. and Lévy, F.: Temperature-dependent pseudogap and electron localization in 1*t*-$TaS_2$. *Physical Review B*, vol. 45, no. 3, p. 1462, 1992.

[15] Brouwer, R. and Jellinek, F.: The low-temperature superstructures of 1T–$TaSe_2$ and 2H–$TaSe_2$. *Physica B*, vol. 99, p. 51, 1980.

[16] Chapman, L.D. and Colella, R.: Experimental evidence from x-ray diffraction for phase excitations in solids. *Physical Review Letters*, vol. 52, no. 8, p. 652, February 1984.

[17] Thompson, A., Gamble, F. and Revelli, J.: Transitions between semiconducting and metallic phases in 1-T $TaS_2$. *Solid State Communications*, vol. 9, pp. 981–985, 1971.

[18] Eichberger, M., Schäfer, H., Krumova, M., Beyer, M., Demsar, J., Berger, H., Moriena, G., Sciaini, G. and Miller, R.J.D.: Snapshots of cooperative atomic motions in the optical sup-

pression of charge density waves. *Nature*, vol. 468, p. 799, 2010.

[19] Möhr-Vorobeva, E., Johnson, S.L., Beaud, P., Staub, U., Souza, R.D., Milne, C., Ingold, G., Demsar, J., Schaefer, H. and Titov, A.: Nonthermal melting of a charge density wave in $TiSe_2$. *Physical Review Letters*, vol. 107, p. 036403, July 2011.

[20] Demsar, J., Forro, L., Berger, H. and Mihailovic, D.: Femtosecond snapshots of gap-forming charge-density-wave correlations in quasi-two-dimensional dichalcogenides 1T–$TaS_2$ and 2H–$TaSe_2$. *Physical Review B*, vol. 66, p. 041101, 2002.

[21] Kusar, P., Mertelj, T., Kabanov, V.V., Chu, J.-H., Fisher, I.R., Berger, H., Forró, L. and Mihailovic, D.: Anharmonic order-parameter oscillations and lattice coupling in strongly driven 1T–$TaS_2$ and $TbTe_3$ charge-density-wave compounds: A multiple-pulse femtosecond laser spectroscopy study. *Physical Review B*, vol. 83, p. 035104, 2011.

[22] Cercellier, H., Monney, C., Clerc, F., Battaglia, C., Despont, L., Garnier, M.G., Beck, H., Aebi, P., andH. Berger, L.P. and Forro, L.: Evidence for an excitonic insulator phase in 1T–$TiSe_2$. *Physical Review Letters*, vol. 99, p. 146403, 2007.

[23] Hellmann, S., Sohrt, C., Beye, M., Rohwer, T., Sorgenfrei, F., Marczynski-Buhlow, M., Kallane, M., Redlin, H., Hennies, F., Bauer, M., Fohlisch, A., Kipp, L., Wurth, W. and Rossnagel, K.: Time-resolved x-ray photoelectron spectroscopy at FLASH. *New Journal of Physics*, vol. 14, p. 013062, 2012.

[24] Hellmann, S., Beye, M., Sohrt, C., Rohwer, T., Sorgenfrei, F., Redlin, H., Kallane, M., Marczynski-Buhlow, M., Hennies, F., Bauer, M., Fohlisch, A., Kipp, L., Wurth, W. and Rossnagel, K.: Ultrafast melting of a charge-density wave in the mott insulator 1T–$TaS_2$. *Physical Review Letters*, vol. 105, p. 187401, 2010.

[25] Ishizaka, K., Kiss, T., Yamamoto, T., Ishida, Y., Saitoh, T., Matsunami, M., Eguchi, R., Ohtsuki, T., Kosuge, A., Kanai, T., Nohara, M., Takagi, H., Watanabe, S. and Shin, S.: Femtosecond core-level photoemision spectroscopy on 1T–$TaS_2$ using a 60-eV laser source. *Physical Review B*, vol. 83, p. 081104, 2011.

[26] Petersen, J.C., Kaiser, S., Dean, N., Simoncig, A., Liu, H.Y., Cavalieri, A.L., Cacho, C., Turcu, I.C.E., Springate, E., Frassetto, F., Poletto, L., Dhesi, S.S., Berger, H. and Cavalleri, A.: Clocking the melting transition of charge and lattice order in 1T–$TaS_2$ with ultrafast extreme-ultraviolet angle-resolved photoemission spectroscopy. *Physical Review Letters*, vol. 107, p. 177402, 2011.

[27] Harb, M., Ernstorfer, R., Hebeisen, C.T., Sciaini, G., Peng, W., Dartigalongue, T., Eriksson, M.A., Lagally, M.G., Kruglik, S.G. and Miller, R.J.D.: Electronically driven structure changes of Si captured by femtosecond electron diffraction. *Physical Review Letters*, vol. 100, p. 155504, 2008.

[28] Ernstorfer, R., Harb, M., Hebeisen, C.T., Sciaini, G., Dartigalongue, T. and Miller, R.J.D.: The formation of warm dense matter: Experimental evidence for electronic bond hardening in gold. *Science*, vol. 323, p. 1033, 2009.

[29] Zamponi, F., Ansari, Z., Korff Schmising, C.v., Rothhardt, P., Zhavoronkov, N., Woerner, M., Elsaesser, T., Bargheer, M., Trobitzsch-Ryll, T. and Haschke, M.: Femtosecond hard x-ray plasma sources with a kilohertz repetition rate. *Applied Physics A*, vol. 96, p. 51, 2009.

[30] Tomov, I.V., Oulianov, D.A., Chen, P. and Rentzepis, P.M.: Ultrafast time-resolved transient structures of solids and liquids studied by means of x-ray diffraction and EXAFS. *The Journal of Physical Chemistry B*, vol. 103, p. 7081, 1999.

[31] Kassier, G.H., Haupt, K., Erasmus, N., Rohwer, E.G. and Schwoerer, H.: Achromatic reflectron compressor design for bright pulses in femtosecond electron diffraction. *Journal of Applied Physics*, vol. 105, p. 113111, 2009.

[32] Kassier, G.H., Haupt, K., Erasmus, N., Rohwer, E.G., von Bergmann, H.M., Schwoerer, H., Coelho, S.M.M. and Auret, F.D.: A compact streak camera for 150 fs time resolved measurement of bright pulses in ultrafast electron diffraction. *Review of Scientific Instruments*, vol. 81, p. 105103, 2010.

[33] Erasmus, N.: *The Development of an Electron Gun for Performing Ultrafast Electron Diffraction Experiments*. Master's thesis, Stellenbosch University, 2009.
[34] Boshoff, I.: *Ultrafast Electron Diffraction on the Charge Density Wave Compound 4Hb–$TaSe_2$*. Master's thesis, Stellenbosch University, 2012.
[35] Kassier, G.H.: *Ultrafast Electron Diffraction: Source Development, Diffractometer Design and Pulse Characterisation*. Ph.D. thesis, Stellenbosch University, 2010.
[36] Rangarajan, L.M. and Bhide, G.K.: Photoemission energy distribution studies of gold thin films under uv excitation by a photoelectron spectroscopic method. *Vacuum*, vol. 30, no. 11/12, p. 515, 2527 March 1980.
[37] Humphries, Jr., S.: *Principles of Charged Particle Acceleration*, chap. 6.7 Solenoidal Magnetic Lens, pp. 125–127. John Wiley and Sons, 1999.
[38] *SciCam SC4022 data sheet*. EHD Imaging GmbH, Zum Rennplatz 15, D-49401 Damme.
[39] Flöttmann, K.: ASTRA (A Space Charge Tracking Algorithm).
[40] Fill, E., Veisz, L., Apolonski, A. and Krausz, F.: Sub-fs electron pulses for ultrafast electron diffraction. *New Journal of Physics*, vol. 8, p. 272, November 2006.
[41] van Oudheusden, T., de Jong, E.F., Siwick, B.J., van der Geer, S.B., Op 't Root, W.P.E.M. and Luiten, O.J.: Electron source concept for single-shot sub-100 fs electron diffraction in the 100 keV range. *Journal of Applied Physics*, vol. 102, p. 093501, 2007.
[42] Wang, Y. and Gedik, N.: Electron pulse compression with a practical reflectron design for ultrafast electron diffraction. *IEEE Journal of Selected Topics in Quantum Electronics*, vol. 18, p. 140, 2012.
[43] Kassier, G.H., Erasmus, N., Haupt, K., Boshoff, I., Siegmund, R., Coelho, S.M.M. and Schwoerer, H.: Photo-triggered pulsed cavity compressor for bright electron bunches in ultrafast electron diffraction. *Applied Physics B*, vol. 109, p. 249, 2012.
[44] van Oudheusden, T., Pasmans, P.L.E.M., van der Geer, S.B., de Loos, M.J., van der Wiel, M.J. and Luiten, O.J.: Compression of subrelativistic space-charge-dominated electron bunches for single-shot femtosecond electron diffraction. *Physical Review Letters*, vol. 105, p. 264801, June 2010.
[45] Erasmus, N.: *Ultrafast Structural Dynamics in 4Hb-$TaSe_2$ observed by Femtosecond Electron Diffraction*. Ph.D. thesis, Stellenbosch University, 2012.
[46] Eichberger, M., Erasmus, N., Haupt, K., Kassier, G., von Flotow, A., Demsar, J. and Schwoerer, H.: Femtosecond streaking of electron diffraction patterns to study structural dynamics in crystalline matter. *Applied Physics Letters*, vol. 102, p. 121106, 2013.
[47] Novoselov, K.S., Jiang, D., Schedin, F., Booth, T.J., Khotkevich, V.V., Morozov, S.V. and Geim, A.K.: Two-dimensional atomic crystals. *Proceedings of the National Academy of Sciences of the United States of America*, vol. 102, no. 30, p. 10451, July 2005.
[48] National Instruments Corporation: Labview 2011.
[49] Rousse, A., Rischel, C. and Gauthier, J.-C.: Colloquium: Femtosecond x-ray crystallography. *Reviews of Modern Physics*, vol. 73, p. 17, January 2001.
[50] Erasmus, N., Eichberger, M., Haupt, K., Boshoff, I., Kassier, G., Birmurske, R., Berger, H., Demsar, J. and Schwoerer, H.: Ultrafast dynamics of charge density waves in 4Hb-$TaSe_2$ probed by femtosecond electron diffraction. *Physical Review Letters*, vol. 109, no. 16, p. 167402, 2012.
[51] Beal, A.R., Hughes, H.P. and Liang, W.Y.: The reflectivity spectra of some group VA transition metal dichalcogenides. *Journal of Physics C: Solid State Physics*, vol. 8, p. 4236, 1975.
[52] This calculation was performed by Maximilian Eichberger, Department of Physics, University of Konstanz, Germany.
[53] Suzuki, A., Koizumi, M. and Doyama, M.: Thermal evidences for successive CDW phase transitions in 1T–$TaS_2$. *Solid State Communications*, vol. 53, no. 2, p. 201, 1985.
[54] Lisowski, M., Loukakos, P.A., Bovensiepen, U., Stähler, J., Gahl, C. and Wolf, M.: Ultrafast dynamics of electron thermalization, cooling and transport effects in Ru(001). *Applied*

*Physics A*, vol. 78, pp. 165–176, 2004.

[55] Su, J.-D., Sandy, A.R., Mohanty, J., Shpyrko, O.G. and Sutton, M.: Collective pinning dynamics of charge density waves in 1T–$TaS_2$. *Physical Review B*, vol. 86, p. 205105, 2012.

[56] Lee, W., Chuang, Y., Moore, R., Zhu, Y., Patthey, L., Trigo, M., Lu, D., Kirchmann, P., Krupin, O., Yi, M., Langner, M., Huse, N., Robinson, J., Chen, Y., Zhou, S., Coslovich, G., Huber, B., Reis, D., Kaindl, R., Schoenlein, R., Doering, D., Denes, P., Schlotter, W., Turner, J., Johnson, S., Frst, M., Sasagawa, T., Kung, Y., Sorini, A., Kemper, A., Moritz, B., Devereaux, T., Lee, D.-H., Shen, Z. and Hussain, Z.: Phase fluctuations and the absence of topological defects in a photo-excited charge-ordered nickelate. *Nature Communications*, vol. 3, p. 838, 2012.